August 2018

Crystal Growth and Manipulation of Intercalated Chalcogenides as Superconductors and Topological Insulators

Nathaniel Smith
University of Wisconsin-Milwaukee

CRYSTAL GROWTH AND MANIPULATION OF INTERCALATED CHALCOGENIDES AS SUPERCONDUCTORS AND TOPOLOGICAL INSULATORS

by

Nathaniel Smith

A Dissertation Submitted in

Partial Fulfillment of the

Requirements for the Degree of

Doctor of Philosophy

in Physics

at

University of Wisconsin-Milwaukee

August 2018

ABSTRACT

CRYSTAL GROWTH AND MANIPULATION OF INTERCALATED CHALCOGENIDES AS SUPERCONDUCTORS AND TOPOLOGICAL INSULATORS
by

Nathaniel Smith

The University of Wisconsin-Milwaukee, 2018
Under the Supervision of Professor Prasenjit Guptasarma

Superconductors are unusual quantum materials which offer no resistance to electric current. The fascinating physics of this phenomenon is complemented by wide-ranging technical applications from power transmission to magnetic levitation. Commercially successful superconductors are found in powerful magnets in medical imaging, particle accelerators, and next-generation quantum computing. In my effort to uncover the mysteries and fundamental mechanisms of superconductivity, I use an array of techniques to synthesize and study single crystals of unconventional superconductors including the iron telluride and bismuth selenide family of superconductors. My study of atomic valence and crystal structure in iron telluride has uncovered previously unknown chemical and structural dependencies of the superconducting state. Taken together, there exists a much stronger dependence than previously known on how elemental concentration, structural defects, and atomic valence determine material properties. In addition, the development of methods to produce high-quality single crystals has enabled my study and modeling of the electronic structure of bismuth selenide at high magnetic fields, previously impossible with lower quality materials. In bismuth selenide, my results show superconductivity is achieved only in samples quenched above 560 °C, with samples quenched at 620 °C showing superconductivity correlated with an expanded Fermi surface cross-section, increase in Fermi

energy, and appearance of nematic charge density waves. Oxygen treatments known to induce superconductivity in thin film iron telluride were applied to bulk iron telluride and found to cause the valence states of tellurium and iron to shift from Te^{0} and Fe^{2+} to Te^{4+} and Fe^{3+}, consistent with oxygen bonding to tellurium and the formation of Fe_2O_3. Additionally, oxygen causes the formation of an oriented $FeTe_2$ intergrowth in single crystals, and the formation of a spin glass magnetic state stable up to room temperature.

DEDICATION

This dissertation is dedicated to my grandfather, for supporting all his grandchildren's education through his hard work, and my wife, for the endless support she has given me in accomplishing my goals.

TABLE OF CONTENTS

LIST OF FIGURES

LIST OF TABLES

LIST OF ABBREVIATIONS

TEM	Transmission electron microscopy
SAED	Selected area electron diffraction
XRD	x-ray diffraction
TEY	total electron yield
LK	Lifshits-Kosevich
SdH	Shubnikov de Haas
dHvA	de Haas-van Alphen
MR	Magnetoresistance
WL	Weak localization
WAL	Weak anti-localization
PTFE	polytetrafluoroethylene
E_F	Fermi energy
v_F	Fermi velocity
k_F	Fermi momentum
$S(\theta)$	Fermi surface cross-section

ACKNOWLEDGEMENTS

Many people have supported my research and personal growth throughout my graduate studies, including my advisors, committee members, lab mates, graduate classmates, collaborators and family.

Firstly, I want to thank my advisor, Prasenjit Guptasarma. Since first sitting in on group meetings before I joined the lab, Prasenjit has harbored a thorough understanding of fine points by everyone in the room and provided atmosphere for exploration of new projects. Prasenjit has given all in his lab an understanding for the rigors of good data collection, scientific principles, and importance of literature. Most importantly, he has encouraged the development of an independent work ethic, technical problem solving, and both academic and personal growth.

Besides my advisor, I would like to thank the rest of my dissertation committee members (Daniel Agterberg, Marija Gajdardziska-Josifovska, Paul Lyman, and Bimal Sarma) for their great support and invaluable advice. Daniel and Paul never ceased to make time for me on both research and academic questions, from minor clarifications, to those where I lacked a complete knowledge of a subject. I am thankful to Marija for her technical knowledge and training in TEM techniques, and her incredible work ethic in making time with all her research investment considering all she does for the UWM Graduate School. Beyond academic and research support, I am especially grateful to her for the advocacy she does for all graduate students on campus. I am also very appreciative to Bimal, for his knowledge of solid state physics and the incredible infrastructure in solid state physics he has harbored at UWM.

Much of my research would not be possible if it were not for the support of collaborators, especially those at national labs, particularly Ke An and Alexey Suslov. I am deeply grateful to

Ke for his support of my battery and neutron research in my fellowship at Oak Ridge National Lab. His guidance and personal contacts to provide resources was invaluable to producing results at ORNL. The supervision and guidance provided by Alexey during experiments at the National High Magnetic Field Laboratory were equally invaluable in interpreting results from experiments. Additionally, his research philosophy and attention to detail are examples to everyone working in research labs.

Last but not least, I would like to express my deepest gratitude to my family and friends. I would not have made it through graduate school without the friends I have made, and the academic, research, and personal support they have given me. This dissertation would not have been possible without their patience, and support. My family has given me the deepest encouragement to be the best I can be for as long as I remember, and I will never forget the work ethic they have instilled in me, and the philosophy that if something can be done better, it hasn't been done well enough. Finally, I would like to thank my wife, for the love and support she has given me in my graduate research during our many years in Milwaukee.

1.0 INTRODUCTION

As our society becomes more dependent on computing and data processing, so are computer systems driven to be smaller, more powerful, and energy-efficient. In the past, this has been driven by the size of the transistors, which has advanced from large vacuum tubes, to solid state devices. These transistors are limited by atomic scales, namely, a transistor cannot be smaller than a single atom. Single-atom transistors would represent several orders of magnitude decrease in size, and limit computing power only in the total size, power, and heat transfer possible on a computer chip. However, even more powerful and energy efficient systems are possible, with one of the most ambitious developments of computing advancement in quantum computing technologies.

In conventional computing, information is stored in the form of 1s and 0s through a binary signal, such as the presence or absence of a voltage, or the polarization of a magnetic domain. Quantum information is stored in a fundamentally different way. Rather than storing each bit of information as a 1 or 0, each qubit is stored as a 1 and 0 simultaneously. While this appears to present a mere doubling of information density, the implications are much more dramatic. When large amounts of information are stored, each bit stores both states (1 and 0) both simultaneously and independently, meaning all possible configurations of qubits are stored. For example, a byte of information representing 8 bits can store one combination of 1s and 0s, while 8 qubits store $2^8 = 256$ possible combinations. When calculations are performed with qubits, a computer can

test all solutions simultaneously, rather than sequentially, leading to a vast improvement in computing power.

The first quantum systems used supercooled atoms at near absolute zero which required large devices to isolate and were difficult to manipulate. Newer systems have used a variety of techniques to generate quantum states, and one technique with the most potential for devices is using superconducting topological insulators. The potential for superconducting topological insulators depends on the development of these materials, including the ability to produce high-quality samples, and a means of tuning the properties which are used for quantum computation.

1.1 MATERIAL MOTIVATIONS

This dissertation will focus on the development of bismuth selenide (Bi_2Se_3) and iron telluride (FeTe) for applications in a variety of areas including quantum computing through topological insulator properties interacting with a superconducting state. These materials have potential uses in many other applications such that control over material properties are of interest even if they cannot be used in quantum computing.

Bi_2Se_3 is well-known as a thermoelectric material, which generates an electrical potential when a temperature gradient is placed across the sample. Additionally, the topological state in Bi_2Se_3 is usable for spintronic computations, which use the electron spin, rather than the electron charge, as a bit. FeTe is part of a class of iron-based superconductors which are unique among other superconductors. Iron-based superconductors have much more metallic properties than other high-temperature superconductors, meaning they are much easier to form into wires for current

transport. In addition, these superconductors have unique low-temperature magnetic states, and enhanced properties in thin films, making them novel among other superconductors, and important to the broader understanding of superconductivity. The study of FeCh (Ch=Chalcogen) type iron-based superconductors, sometimes named 11 type in reference to the element stoichiometry, is largely motivated by their apparent simplicity among iron-based superconductors. While the more complicated 1111 structures have much higher superconducting temperatures (56K in $NdFeAsO_{0.83}$) versus 11 type (8K in FeSe), the simplicity of 11 structures makes the study of fundamental physical properties easier and translatable to other iron-based superconductors. Recently the discovery of anomalously high superconducting temperatures in FeSe thin films, engineering of FeTe/Bi_2Te_3 interfaces, and potential for topological surface states have brought increased interest to the FeCh system of superconductors. A greater understanding of the characteristics of these materials will greatly increase our understanding of both topological and superconducting materials physics.

1.2 TOPOLOGICAL SYSTEMS

Topological systems have gained much interest in recent years due to their interesting physical properties and potential for new technologies, such as spintronics and quantum computing aforementioned.[1–3] 3D (or 2D) topological systems are generally manifest as materials which have insulating bulk (surface) states, but conducting surface (edge) states. These are divided into categories based on the origin of the topology, such as Dirac semimetals, Weyl semimetals, and topological insulators. This dissertation is primarily focused on the class known as topological insulators. Topological insulators in 3D materials were first discovered in $Bi_{1-x}Sb_x$,[4] and have

since been found in Bi_2Se_3, Sb_2Te_3, as well as other materials with strong spin-orbit coupling, usually containing pnictides and chalcogenides, although compounds featuring lead and tin have recently been discovered.[5] Strong spin-orbit coupling creates electronic states with broken time reversal symmetry without an external magnetic field.[6–8] The exact effects of this and other symmetries on topological states will be discussed later. The prediction and subsequent discovery of topological insulators has generated intense research into this new state of matter motivated both by their physical novelty and potential applications stemming from their unique properties. Applications in areas such as spintronics are driven by the so-called "topological protection" from scattering of the surface states, making electronic states robust from scattering even when defects are present. These materials' use in quantum computing is driven by unique Majorana fermion properties when topological and superconducting states coexist. While the study of topological insulators has generated much research in recent years, topological states themselves are not new. Perhaps the simplest example of a non-trivial topological state is the quantum Hall state.[9] The quantum Hall state occurs when 2D electrons with sufficient mobility are placed in a high magnetic field. In this scenario, electrons are split into quantized Landau levels with energy

$$\epsilon_n = \hbar\omega_c\left(n + \frac{1}{2}\right); n \geq 0, \tag{1.1}$$

where ω_c is the cyclotron frequency. These Landau levels have a finite energy broadening due to electron scattering and thermal effects. This quantization of energy levels leads to the sample becoming insulating at magnetic fields when there is no overlap of a Landau level with the Fermi energy, and thus the density of conducting states becomes zero. At the same time, the Hall conductance becomes quantized according to the following equation for well separated Landau levels, where the Hall conductance is written as

$$\sigma_{xy} = \frac{j_y}{E_x} = n\frac{e^2}{h} \tag{1.2}$$

where j_y is the current density, E_x is the electric field in a perpendicular direction, e is the electron charge, and h is the plank constant.

This "topologically" insulating quantum Hall state is distinct from a "trivial" insulator and has unique properties which are determined by the calculation of a topological number. Firstly, while both trivial and quantum Hall insulators are formed due to an exclusion of electrons from the Fermi energy leading to a lack of longitudinal conductance, the quantum Hall state has a finite Hall conductance. In a trivial insulator, the electrons are excluded from conduction bands due to electrons binding to atomic cores, while in the quantum Hall insulator, the electrons are bound into cyclotron orbits. Unlike the trivial insulator, the scattering of electrons at the edges of the sample in a quantum Hall insulator creates anomalous surface currents. This difference in scattering can be visualized in Fig. 1-1.

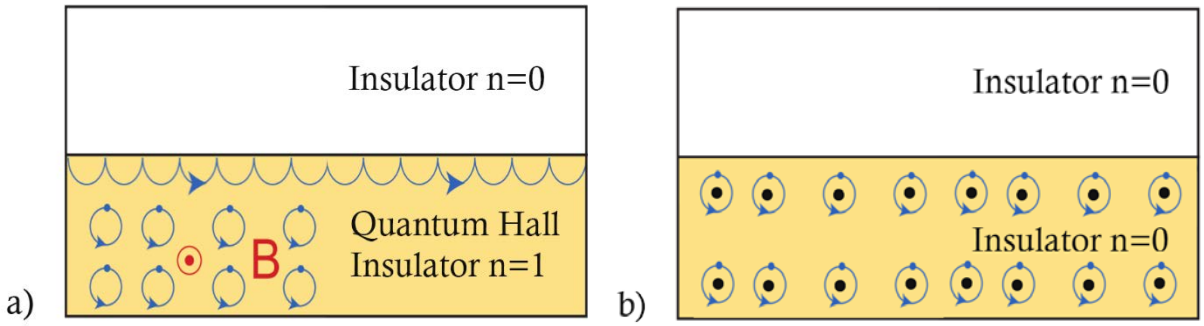

Figure 1-1. In a), bulk electrons are bound in cyclotron orbits, while a conducting edge state appears. In a normal insulator b), all electrons are bound to atomic cores.

The existence of edge states in topological systems is driven by the bulk boundary correspondence, which forces the existence of a conducting state whenever topology

changes.[6,7,10,11] This surface state occurs between a topological insulator and vacuum (a trivial insulator), although in general topology can change at any surface where the topological number changes, such as in a vortex core of a superconductor, or material interface.

While novel, the quantum Hall state is only possible in thin samples with high electron mobility, at very low temperatures, and high magnetic fields. These restrictions makes the use of the quantum Hall states for applications such as computing unfeasible. Topologically insulating materials have electrons in topological states without the need for high magnetic fields, and may be robust even at room temperature depending on the size of the material's bulk band gap.

To discuss how topological insulators are manifest, and how topological materials are possible without the application of a magnetic field, this dissertation will first briefly overview how topological distinctness is determined by the calculation of topological invariant numbers, specifically, the Chern number.

1.2.1 Topological numbers

A material's topological distinctness is determined by calculating a topologically invariant quantity such as the Chern number. The Chern number is constructed in the following manner. We start by considering a band insulator with the following generalized Hamiltonian and wavefunction

$$H(\boldsymbol{k})|u_n(\boldsymbol{k})\rangle = E_n(\boldsymbol{k})|u_n(\boldsymbol{k})\rangle. \tag{1.3}$$

We define $A^{(n)}(\mathbf{k})$ as the Berry connection, a measure of the rate of change of the wavefunction,

$$A^{(n)}(\boldsymbol{k}) = i\langle u_n(\boldsymbol{k})|\,\partial_k u_n(\boldsymbol{k})\rangle \tag{1.4}$$

and a "field strength,"

$$F_{ij}^{(n)}(\boldsymbol{k}) = \partial_{k_i} \mathrm{A}_{k_j}^{(n)}(\boldsymbol{k}) - \partial_{k_j} \mathrm{A}_{k_i}^{(n)}(\boldsymbol{k}). \tag{1.5}$$

From this we construct a gauge-invariant quantity which can be shown to take integer values when integrated around the 2D Brillouin zone:[7]

$$Ch_1^{(n)} = \frac{1}{2\pi} \int_{2DBZ} dk_x dk_y F_{xy}^{(n)}(\boldsymbol{k}) \,. \tag{1.6}$$

The evaluation, and quantization, of this integral is related to the singularities of $A^{(n)}(\boldsymbol{k})$ in the Brillouin zone and is non-zero for non-trivial topologies. The Berry phase is also constructed in a similar way, which is the line integral of $A^{(n)}(\boldsymbol{k})$ around a closed path,

$$\oint_C d\boldsymbol{k} \cdot \boldsymbol{A}^{(n)}(\boldsymbol{k}) \tag{1.7}$$

and is also gauge invariant. However, the Berry phase is not restricted to integer values except in special cases, and is thus not generally a good topological number.

Symmetries play an important role in the determination of topological states and often simplify this calculation. For example, under time reversal symmetry, one can show $F_{xy}^{(n)}(\boldsymbol{k}) = -F_{xy}^{(n)}(-\boldsymbol{k})$, and therefore $Ch = -Ch = 0$. In this case time-reversal breaking is necessary to realize a non-zero Chern number and a topologically non-trivial quantum number. In the case of a material exhibiting the quantum Hall effect, time-reversal symmetry-breaking is supplied via the application of an external magnetic field. In general, there are other means of breaking time-reversal symmetry such as spin-orbit coupling, and materials that have a non-trivial topological number (e.g. Chern number) without external conditions (such as the application of an external magnetic field) are of interest due to a greater ease in use for devices. Furthermore, a topologically insulating state is only present in band insulators, i.e. materials with a sufficiently large band gap

which separates valence and conduction electrons under thermal fluctuations are of particular interest.[7]

Bi_2Se_3 is one such material which has a non-zero topological number known as the "spin Chern number," which defines Chern numbers for up and down spins separately, and the topological class is based on the parity of these numbers even though the net Chern number for all electrons is 0. Further, the large bulk band gap in Bi_2Se_3 allows surface states to dominate conduction if the Fermi energy is tuned to reside in the gap even at room temperature. In Bi_2Se_3, conducting, spin-polarized, surface states manifest through Kramers degeneracy, which dictates that electron spin states must be degenerate at momenta where time-reversal invariance is held. In particular, time-reversal symmetry only exists at momentum $\mathbf{k}$ =0 (Γ point) in Bi_2Se_3. The degeneracy in these spin states are broken at all other momenta due to time-reversal symmetry breaking from spin-orbit coupling.[12] Kramers degeneracy and the non-zero spin Chern number provide helical wrapping of the surface spin states unique to a topological insulator as shown in Fig. 1-2 a).

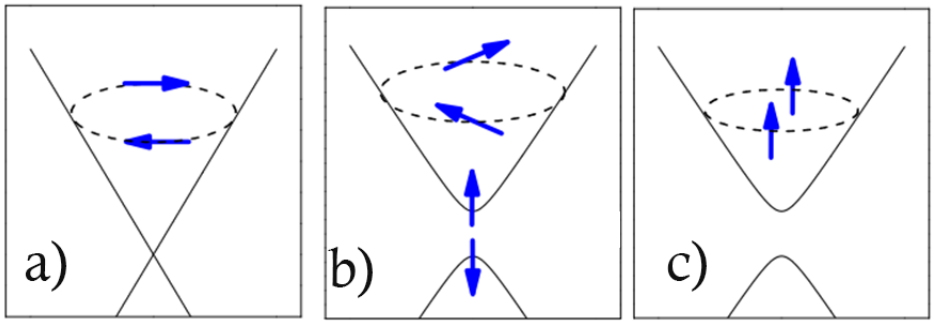

Figure 1-2. Under no magnetic field in a), spin surfaces are wrapped around the time reversal invariant momentum. As magnetic field in increased in b) and c) spin polarized surface states decouple and become polarized.

If time-reversal symmetry at **k** =0 is broken, for example by the addition of an external field, a band gap opens in the surface states, as shown in Fig. 1-2 b) and c). While small fields allow some coupling between surface states, eventually the topology of the surface states becomes trivial. Thus, external magnetic fields can break the degeneracy of surface states in an intrinsic topological insulator, although a new topologically distinct state (quantum Hall state) is induced in 2D materials for sufficiently large fields. The distinct surface states of topological insulators from bulk states or "trivial" surface states (e.g. monolayer films) are the main physical phenomena associated with the topological phase, and manifest as an anomalous surface current in 3D materials, or edge currents in 2D materials. In the case of Bi_2Se_3, and other 3D topological insulators, these surface states are spin-polarized, unlike the edge currents produced in a quantum Hall insulator.[13] This difference is shown in Fig. 1-3. Many additional physical phenomena appear

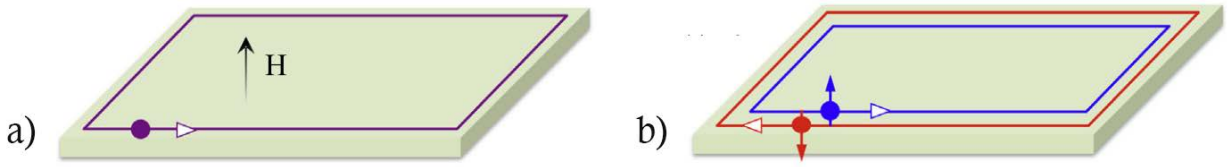

Figure 1-3. In a) the application of a magnetic field produces an edge current. In a topological insulator b), spin-polarized edge currents are produced without the application of fields. [adapted from ref. 13]

when a superconducting and topological state coexist including those applicable to quantum computing. In order to explore the potential for this interaction, we will first discuss the properties of superconductivity and how it is detected.

1.2.2 Superconductivity

The main effect of superconductivity on the electromagnetic properties of a material is due to the pairing of electrons to form a perfectly conducting state and the complete expulsion of magnetic fields from the material. These effects begin to appear at critical temperature T_c and generally have a small range of temperature for the sample to completely transition to the superconducting state. This gradual transition is often caused by inhomogeneities and defects in the sample but generally has a finite width even in very homogenous samples. There are many other signatures of the superconducting state including changes in heat capacity, flux quantization, microwave absorption, etc., but perfect conduction and magnetic expulsion are the main properties of interest in the detection of superconductivity and interaction with a topological state.

The exact origin of superconductivity in many systems, including those of interest in this dissertation, is not always clear, however, many signatures of superconductivity are universal across all systems, particularly resistive and diamagnetic transitions. For superconductivity to appear, conducting electrons (or holes) must have a means of propagating through the material without loss of energy. This is the minimum requirement for a state with zero resistance. Superconducting theory allows for this by adding a pairing potential between electrons with opposite momentum. The attractive pairing, usually mediated through phonons, allows fermionic electrons (holes) to form a Bose-Einstein condensate. Condensation of electrons (holes) allows for electrons (holes) to change momentum with zero energy loss through an interaction with the lattice. The pairing of electrons at the Fermi energy also lowers the energy of conducting electrons (holes) and forms a gap in the density of states at the Fermi energy. This gap technically makes the superconducting state topologically identical to a trivial insulator, even though conduction is still possible. The opening of a band gap in a superconductor (shown in Fig. 1-4) allows for the

calculation of topological numbers, for which the material must exist in a fully gapped bulk state. Additionally, the particle-hole pairing symmetry induced in a superconductor will influence the determination of topological class due to the dependence of topological numbers on the symmetry states in a material.

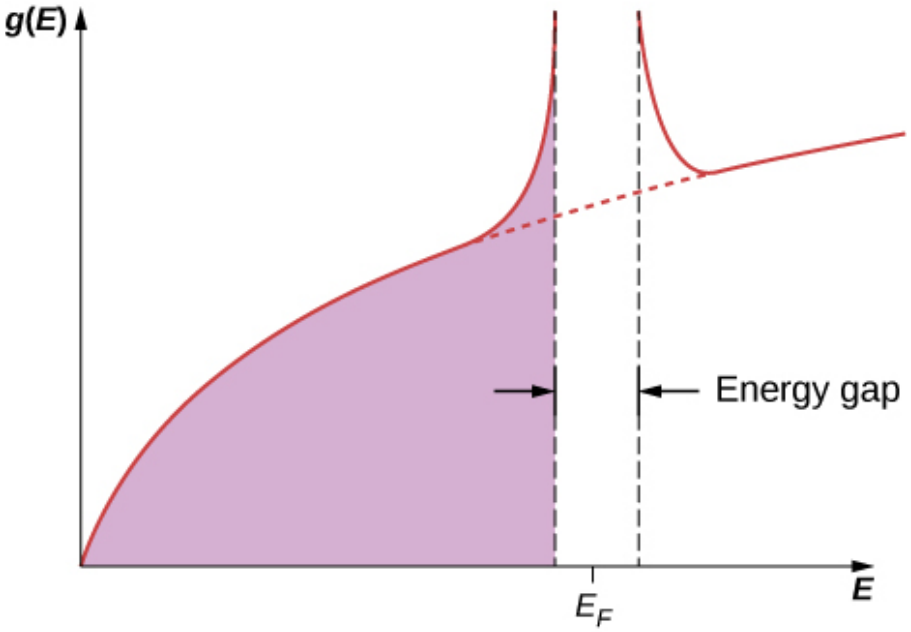

Figure 1-4. Formation of the superconducting energy gap at the Fermi energy

In addition to obtaining zero resistance, superconductors also become completely diamagnetic below a critical magnetic field (H_c). This expulsion of fields is achieved by a spontaneous screening current manifest in the superconductor, the physics of which will not be discussed in this dissertation.[14] Diamagnetism is used as a tool to detect superconductivity through measurements of magnetization, and is also particularly relevant to the interaction of the superconducting and topological states. In superconductors designated "Type II," magnetic flux quanta penetrate the superconducting state above a critical field (H_{c1}) by creating non-superconducting regions known as an Abrikosov vortices, inside the otherwise superconducting material that is screened by a superconducting current. The density of vortices increases with

magnetic field until the entire material becomes normal above a second critical field (H_{c2}). When a topological material and a superconductor coexist, these vortex cores provide a boundary between a trivial and topological state, which harbors topological edge states and Majorana fermions. While a vortex is not necessary to generate topological edge states, which are generally produced at any boundary where a topological number changes, vortices are manipulable via magnetic fields, unlike other boundaries such as crystal defects or the sample surface.

1.2.3 Topological Superconductivity

As electrons pair to form the superconducting state, the opening of an energy gap at the Fermi energy allows for the construction of topological numbers. In addition, a particle-hole symmetry is introduced, which is essential in construction of topological numbers in superconductors. In 1D (e.g. a superconducting edge state) this quantizes the Berry phase as $M\pi$, where M is an integer.[7] This Berry phase is essential for the creation of Majorana fermions, pairs of which can form qubits for quantum computing.[1,7,11,15]

When a type-II superconductor is in a sufficiently strong magnetic field, the magnetic flux penetrating the material breaks the superconducting state. Edge states of supercurrent circulate around the flux cores which transition into the normal state.[16,17] If the normal metal has different topology than the superconductor, this will create an edge state due to the bulk boundary correspondence which is manipulable via magnetic fields to make practical devices.[7]

1.2.4 Majorana Fermions

The creation of Majorana fermions is the primary goal of producing topological superconductors for quantum computing. The Majorana fermion was first proposed in 1937 as an elementary particle satisfying the Dirac equation that is identical to its own antiparticle.[18] Soon after the discovery of topological insulators, it was realized the coexistence of a superconducting and topological state would harbor Majorana fermion quasiparticles.[15] In the superconducting state, electron and hole excitations are superimposed, allowing a superconducting excitation to act as its own antiparticle.

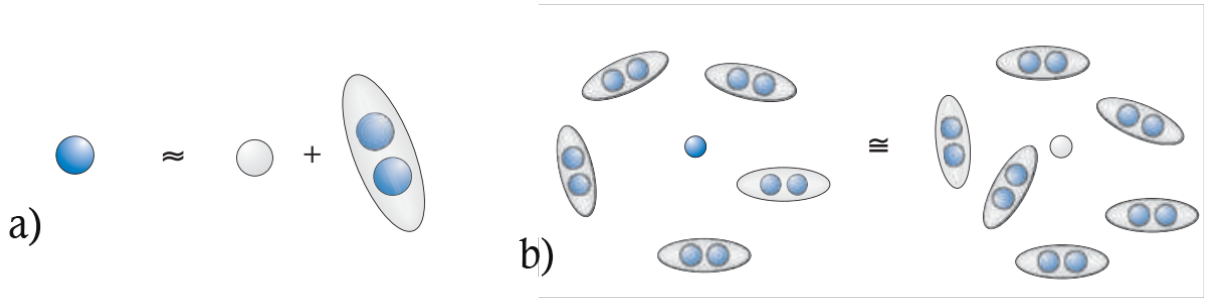

Figure 1-5. a) In a superconductor, a hole (white) can bind to a Cooper pair of electrons, acquiring a negative charge. b) Cooper pairs cluster around holes such that no distinction between electrons and holes remain.[15]

The gapless excitations (surface states) formed at the boundaries of topological insulators are naturally described by the Dirac equation.[11,19] This combination of properties allows edge states in topological superconductors to act as Majorana quasiparticles. While the conducting surface state of a topological insulator is generally at odds with the fully gapped state of superconducting Cooper pairs, the boundary of a superconductor and topological insulator at locations such as Abrikosov vortices support Majorana quasiparticles through the superconducting proximity effect.[7] The Berry phase ($\varphi=\pi$) for superconducting topological insulator) induced by

"braiding" vortices allows pairs of Abrikosov vortices to become their own antiparticles through a $\varphi=\pi$ phase change around a Abrikosov vortex allow Majorana states to have identical creation and annihilation operators, allowing their use as quantum memory.[1,7,20]

1.3 MANIPULATION OF THE FERMI SURFACE

To create devices which exploit properties of the topological state, one must first synthesize high-quality samples of relevant materials and learn how to manipulate factors which alter or tune the topological and superconducting state. These alterations are made through the manipulation of the material's symmetry, chemical potential, and spin-orbit coupling parameters. Coupling parameters and material symmetry are crucial to generate a topological state, which must manifest from a fully gapped band structure, while tuning the chemical potential is important to realize the isolation of topological surface states, rather than the coexistence of topological and bulk conducting states. This dissertation mainly focuses on controlling these effects through modification of interstitial elements and quenching parameters used in the synthesis of candidate topological superconductors, namely FeTe and Bi_2Se_3 compounds.

The most direct way altering the Fermi surface is through the addition of charge carriers. Charge carrier doping is often achieved by element substitution, for example in semiconductors, but this technique often has effects on material symmetry and atomic coupling parameters, which alter the band structure. Intercalation, on the other hand, modifies the Fermi energy in a more direct and isolated manner than doping. In interstitial regions, the only bonding present is due to van der Waals forces, and therefore elements added to the interstitial do not bond strongly to elements in the lattice, limiting their effects on the rest of the material. Interstitial charge doping may be

achieved as a 2D, 1D, or 0D effect, but in materials such as FeTe and Bi_2Se_3, the interstitial region is a plane, and separates 2D layers of parent material. In this way, these systems are much like graphite with loosely bound layers of material. When metal ions are added to the interstitial, the increased density of electrons increases the Fermi energy due to the Fermionic nature of electrons, demanding any additional electrons fill unoccupied higher energy states.[21] In general 1D or 0D interstitial sites also exist, which are organized in either columns or points. Intercalated compounds of this type are especially popular in electrochemical storage materials.[22,23] While intercalated atoms are relatively isolated from the rest of the atomic structure, the lattice often expands in the directions perpendicular to the area of the interstitial, although lattice contraction is also possible, e.g. in $NaMO_3$ (M=Transition metal).[24] In Bi_2Se_3 and FeTe, increasing concentration of intercalating atoms translates to an expansion of the *c* axis.[25,26] Additional details of the effects of metal intercalation in Bi_2Se_3 and FeTe will be discussed in later sections.

1.4 OBJECTIVE #1: EFFECTS OF QUENCHING ON SUPERCONDUCTIVITY AND THE TOPOLOGICAL STATE IN BISMUTH SELENIDE

The appearance of superconductivity at atmospheric pressure in copper-intercalated bismuth selenide is perhaps the most direct manifestation of the coexistence of a topological insulator and a superconductor. While the topological state in Bi_2Se_3 is interesting on its own accord, the appearance of superconductivity in Bi_2Se_3 opens the door for many potential applications of the material, and answers to fundamental questions of the behavior of electrons in the system, including how superconducting electrons are formed and how they interact with the topological state. However, the study of this system is impeded by a lack of consistency in synthesizing

superconducting samples. The appearance of superconductivity only appears when intercalated samples are quenched, although the direct effects of quenching are not understood. The effects of quenching on the Fermi surface and Fermi energy must be determined with respect to appearance of the topological and superconducting state and will help to explain the origin of superconductivity in Bi_2Se_3 as well as a universal means of manipulating the Fermi energy of related systems.

1.5 OBJECTIVE #2: EFFECTS OF OXYGEN TREATMENT ON SINGLE-CRYSTAL IRON TELLURIDE

The properties of iron-based superconductors are influenced strongly by intercalated elements that modify low-temperature structural and magnetic phases in FeTe. Oxidation of FeTe is suggested to remove interstitial iron in single crystals and is shown to induce superconductivity in thin films. However, oxidation of FeTe does not reliably induce superconductivity in bulk FeTe. The difference in effects of oxygen in FeTe single crystals and thin films remains an open question, and a characterization and explanation of these differences will create a greater understanding of the control of superconductivity in Fe-based superconducting systems. Here we investigate the effects of oxidizing $Fe_{1+d}Te$ single crystals on interstitial iron and the surrounding crystal structure.

2.0 CRYSTAL GROWTH

To study the properties of Bi_2Se_3 and FeTe, synthesis of high-quality single crystals is first performed. While the manifestation of a topological state has no large requirement on the size of a crystal domain, the growth of single crystals is critical for the study of crystal properties. The appearance of large single crystals ensures sample homogeneity, as inhomogeneity usually results in defects such as grain boundaries. Many material properties depend on the quality of the atomic lattice, and a high defect density influences many material properties such as the robustness of the superconducting state and electron mobility. Additionally, angle-dependent measurements are not possible in samples with many small crystals of different orientations. Thus, the growth of large single crystals is a great advantage in the characterization of many material properties.

Single-crystal growth of FeTe and Bi_2Se_3 was primarily performed using a self-flux method. Here, stoichiometric ratios of constituent elements are sealed in an evacuated quartz ampule. This technique provides a method for synthesis of reactive compounds which precipitate a solid directly from a liquid, particularly in congruent ($S \leftrightharpoons L$) or syntactic ($L_1+L_2 \leftrightharpoons S$) reactions.[27] It is not possible to form large crystals which usually form via a solid state reaction ($S_1 \leftrightharpoons S_2$) unless a flux is used to dissolve the elements . Self-flux crystal growth via quartz ampules is applicable for a large variety of elements due to the relatively low reactivity of silica glass (also known as fused quartz) up to temperatures of ~1120 ºC, above which temperature the strength of quartz begins to significantly weaken. In some cases, our group has modified this method to use double walled quartz tubes, or alumina tubes sealed in quartz, when ampule failure is caused by element reactivity or expansion upon solidification.

2.1 IRON TELLURIDE

FeTe is a non-superconducting binary compound of the same structure as superconducting FeSe. This phase is of particular interest due to its status as the simplest variant of the Fe-based superconductors.[28,29] Samples of iron telluride were prepared to study the effects of oxygen on atomic valence states, interstitial iron, and crystallography via the following method. $Fe_{1+d}Te$ was prepared with tellurium pieces (Alfa Aesar 99.999%) and iron pieces (Alfa Aesar 99.99%) which are mixed in stoichiometric ratios under Argon atmosphere and sealed in quartz tubes under vacuum of <60 mTorr. The samples were heated to 425 °C at 10 °C/min, then to 960 °C at 1° C/min where the temperature was stabilized for one hour. The samples were then cooled to 750 °C at a rate of 6 °C/hour and quenched in room-temperature water. The quench temperature of 750 ºC was chosen to correspond to the broad area of the β phase (Fig. 2-2), to reduce the likelihood of impurity phases forming due to local inhomogeneity.[30]

The resulting single crystals were large and easily cleavable along the *ab* plane as seen in Fig 2-1. Oxygen annealing was performed by heating cleaved crystals or ground powders to 125 °C for 2.5 hours in a tube furnace of volume $1.5x10^3$ cm^3 while flowing oxygen gas at a rate of $1x10^4$ cm^3/hr during heating and cooling.

Figure 2-1. Single crystals of iron telluride

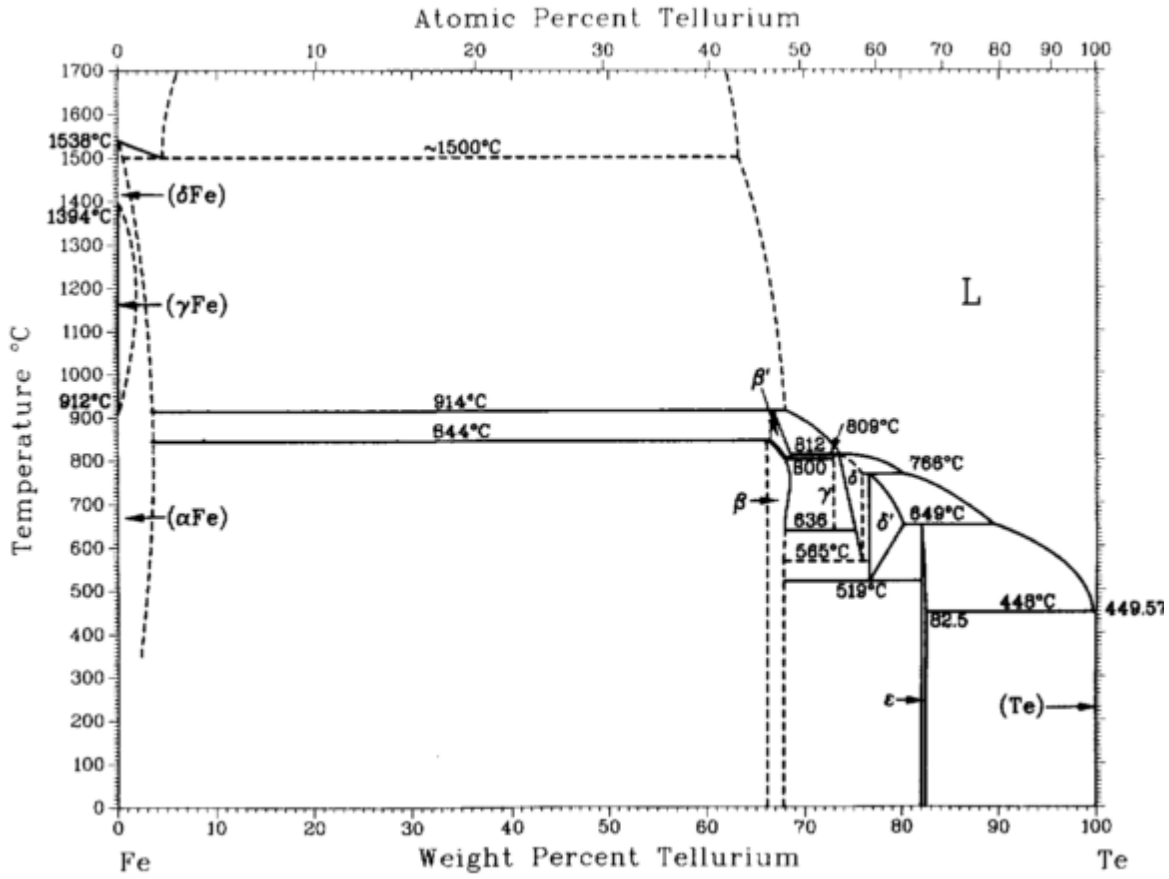

Figure 2-2. Phase diagram of the Fe-Te system. The phases labeled β, δ, and ε correspond to FeTe, Fe_2Te_3, and $FeTe_2$ phases respectively. The crystal structure of the γ phase has not been identified. Phases labeled γ, δ, and δ' are generally not stable at room temperature. [30]

Single crystals of FeTe do not typically show a superconducting phase transition, although $FeTe_{1-x}Se_x$ is superconducting for $0.3<x<1$ with the highest confirmed T_c for an iron-based superconductor (T_c=65K) obtained by growing monolayer FeSe on a $SrTiO_3$ (001) surface.[31] FeSe cannot be grown into bulk single crystals, even though the phase diagram of Fe-Se is very similar to that of FeTe. There is, however, an important difference in the disappearance of the Catatectic region of the phase diagram such that FeSe forms from a solid solution of α-phase Fe and δ-phase Fe_3Se_4.[32] In addition limitations on crystal size, the region of the phase diagram (shown in Fig. 2-3) leading to superconductivity (tetragonal phase) has only a narrow range of stoichiometry and

quench temperature leading to superconductivity. $Fe_{1+d}Se$ (d=0.01-0.03) samples must be quenched from between 300-450 °C in order for superconductivity to occur.[33] Although we have grown FeSe from a flux, the extreme sensitivity to stoichiometry has limited the ability to produce superconducting samples due to a flux's ability to alter characteristics of the phase diagram through factors such as precursor solubility and crystallization dynamics.

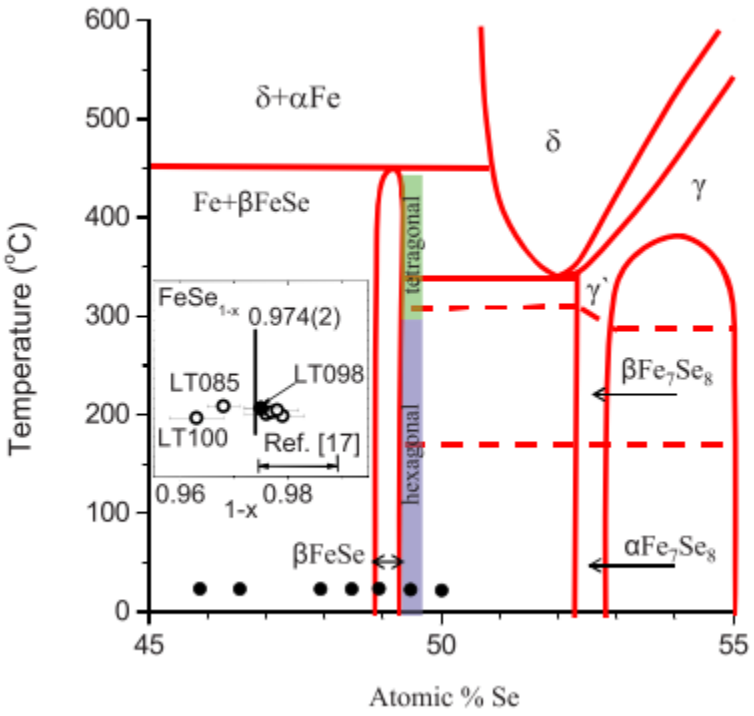

Figure 2-3. Phase diagram of the Fe-Se system[33]

The phase stability and iron intercalation concentration of $Fe_{1+d}Te$ are two of the factors thought to affect the onset of superconductivity in bulk $Fe_{1+d}Te$. In this dissertation, the control of interstitial iron via oxygen annealing in $Fe_{1+d}Te$ is used as a method of post-synthesis treatment to alter interstitial iron concentration and tune the structure into the optimal concentration for superconductivity. This method of generating single-crystal $Fe_{1+d}Te$ with controllable iron concentration will provide a valuable source of knowledge on the control of interstitial elements in iron-based superconductors.

2.2 BISMUTH SELENIDE

Bi_2Se_3 was prepared in a similar manner to FeTe, where stoichiometric ratios of bismuth and selenium were sealed in evacuated quartz ampules. Bi_2Se_3 crystallizes easily from the melt due to the crystallization directly from the self-flux. Superconductivity in this sample is only induced by quenching, which must be performed above 560 °C, according to Schneeloch et al.[34] However, the large number of phases with similar stoichiometry and crystallization temperatures in the Bi-Se system is a sign of the small amount of energy needed for a crystal phase transition.[35] This stark contrast to similar crystals such as Sb_2Te_3 is apparent in Fig. 2-4.[36] The Bi-Se system contains many stoichiometrically similar compounds (Bi_3Se_4, Bi_4Se_5, etc.) which are easily be formed via mechanical stress. This aspect makes the hexagonal Bi_2Se_3 particularly sensitive to mechanical stress. A consequence of this sensitivity is that the sample cannot be mechanically ground to a powder due to the crystal decomposing into multiple phases, making many measurements such as powder XRD of pure phase Bi_2Se_3 single crystals infeasible. Additionally, the sample surface oxidizes easily, requiring careful storage and minimization of time spent in air to maintain pure-phase samples.[37] While the crystal phase of Bi_2Se_3 is much more sensitive than similar topological insulators, such as Sb_2Te_3, it has a much larger bulk band gap of ~0.3 eV vs ~0.01 eV, meaning surface states can dominate transport properties at much higher temperatures when the Fermi energy lies in the bulk bandgap.[38]

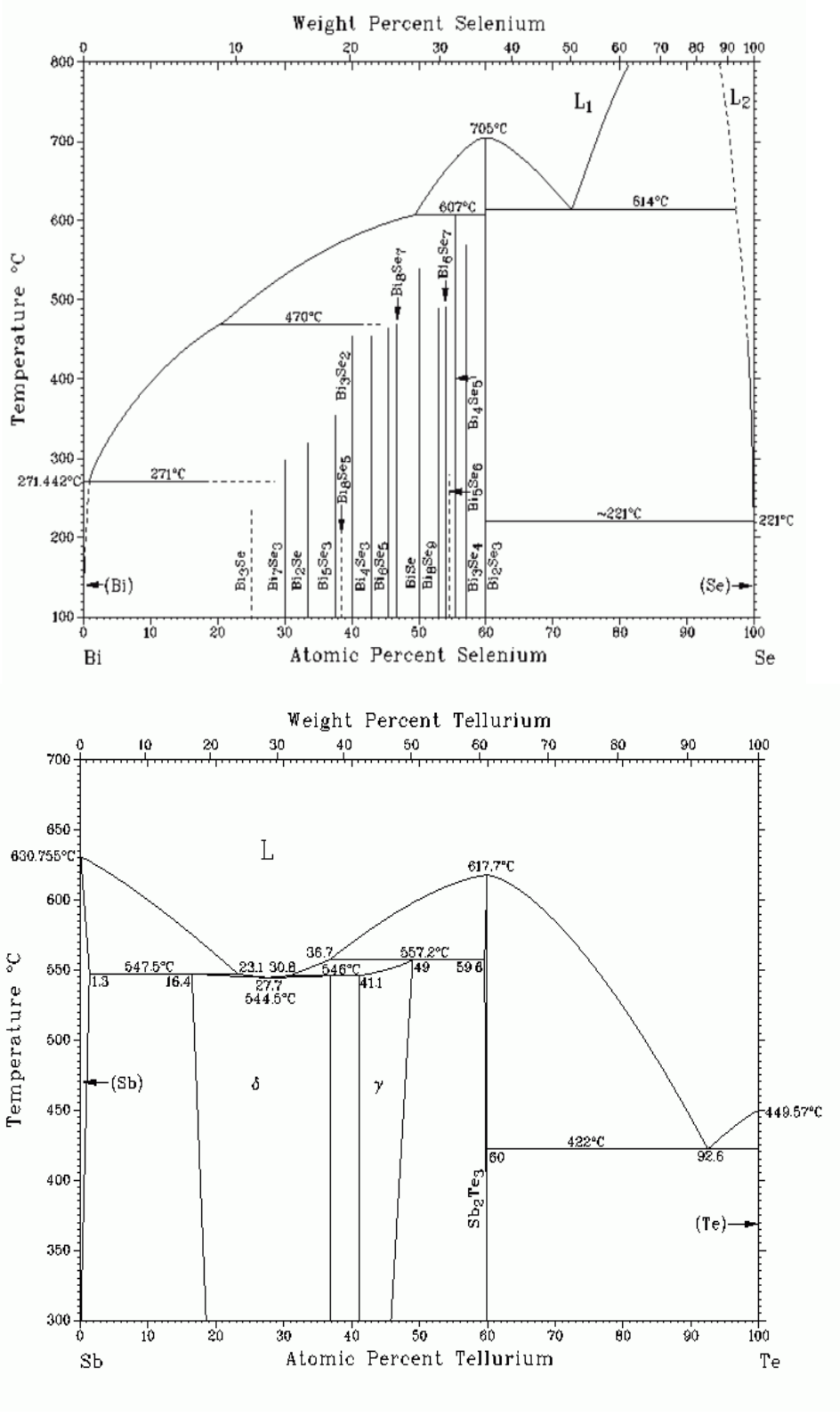

Figure 2-4. Phase diagrams of the Bi-Se and Sb-Te systems containing the isostructural topological insulators Bi_2Se_3 and Sb_2Te_3.[36]

3.0 SPECIAL TECHNIQUES

3.1 TRANSPORT MEASUREMENTS

Resistivity measurements were performed using a 4-probe inline measurement as diagrammed in Fig. 3-1. This configuration allows the measurement of sample resistance $R = V/I$ without needing to subtract the resistances of the wires or contacts. In the 4-probe technique, no current is sent through wiring to the voltmeter, guaranteeing no voltage drop due to the resistance of the wire (R_w), or the contact resistance.

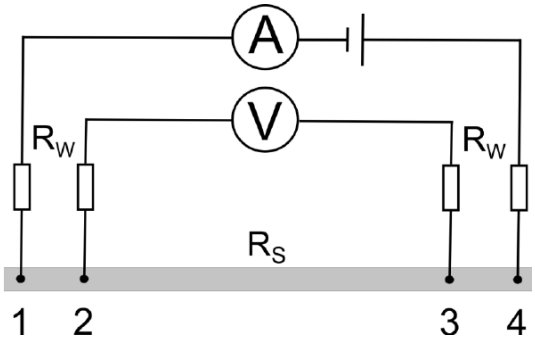

Figure 3-1. Schematic of 4-probe resistance measurement

At cryogenic temperatures, consideration of the current is made to minimize heating at the sample and maintain a uniform temperature between the sample and the cryostat. A current typically of the order of 1 mA was used. For $Cu_{0.12}Bi_2Se_3$ sample 2b (for example), this translates to a heating power at the sample of ~ $1x10^{-7}$ W, which has a negligible effect on the sample temperature due to the much higher cooling power of the cryostat.

Samples were mounted on a "Resistance Puck" by Quantum Design for use in a Physical Property Measurement System (PPMS) (Fig. 3-2a) and 8 contact DIP sockets (Fig. 3-2b) for use

at the National High Magnetic Field Laboratory. Crystals were fixed to the carriers using VGE-7031 varnish and cured at room temperature in inert atmosphere to minimize air exposure. Electrical connections were made using 20 μm gold wire affixed to samples and I-V contacts with silver paint. All wires in the probe channel were formed into twisted conducting pairs to minimize any signals from inductive effects.

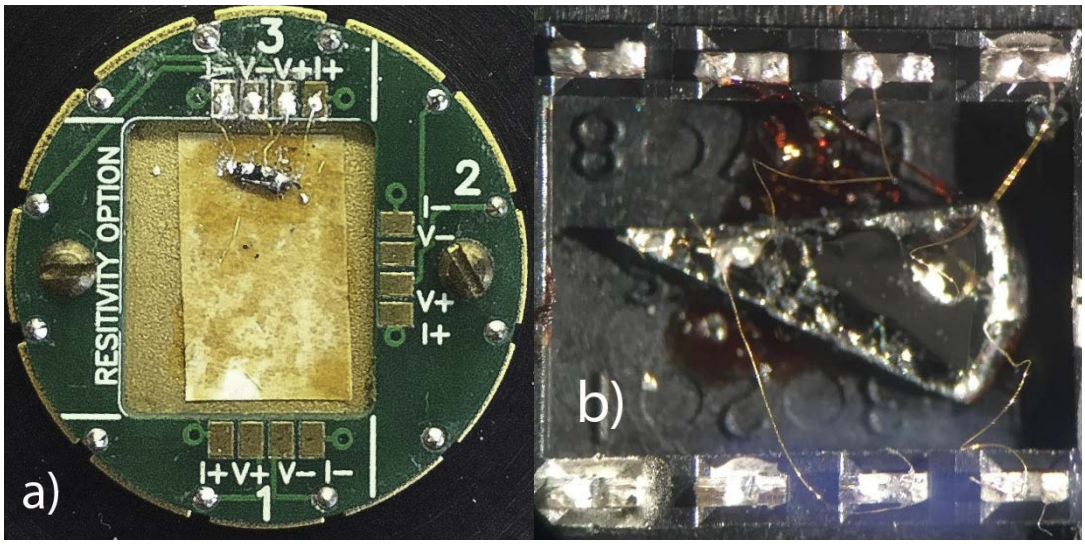

Figure 3-2. Inline contacts for resistance measurements on $Cu_xBi_2Se_3$ samples.

3.1.1 Shubnikov de Haas Oscillations

Shubnikov de Haas (SdH) oscillations in resistivity were analyzed to probe the Fermi surface of Bi_2Se_3. SdH oscillations appear in resistivity in strong magnetic fields at low temperatures as the result of a changes in the density of electron states at the Fermi level. When a strong magnetic field is applied, allowed orbital energies of electrons (E) are quantized into constant energy surfaces according to the equation

$$E = \left(n + \frac{1}{2}\right)\hbar\omega_c\,,\ \omega_c = \frac{eB}{m^*c}, \tag{3.1}$$

where m^* is the effective electron mass, B is the magnetic field, e is the electron charge, and c is the speed of light.

These energy levels have a finite width, which can cause the quantized energy levels to overlap. When the constant-energy surfaces are sufficiently separated on a 2D Fermi surface, the material enters the quantum Hall state discussed earlier, where the material becomes periodically insulating with magnetic field. Before this point, an increasing magnetic field causes sequentially numbered levels to pass through the Fermi level, causing a modulation in the density of electrons participating in conduction. The varying density of states causes a modulation in resistivity which is modeled using the Lifshits-Kosevich (LK) formula for SdH oscillations,

$$\Delta R = A\, sin\left(\frac{2\pi f}{B} + \beta\right) \tag{3.2}$$

$$A \propto B^{1/2} \frac{\alpha m^* T/B}{\sinh(\alpha m^* T/B)} \exp(-\alpha m^* T_D/B) \tag{3.3}$$

where ΔR is the change in resistance from the background magnetoresistance, f is the SdH frequency, B is the applied magnetic field, β is the Berry phase, $\alpha = 2\pi^2 c k_B/e\hbar \approx 14.69$ T/K, and $T_D = \hbar/2\pi k_B \tau_S$ is the Dingle temperature.[39,40] τ_S is the mean scattering time of electrons, which is directly related to electron mobility. Minimum resistance is achieved as Landau levels pass through extremal cross sections of the Fermi surface. The separation of energy levels under application of magnetic fields is illustrated for a spherical Fermi surface in Figs. 3-3 and 3-4.

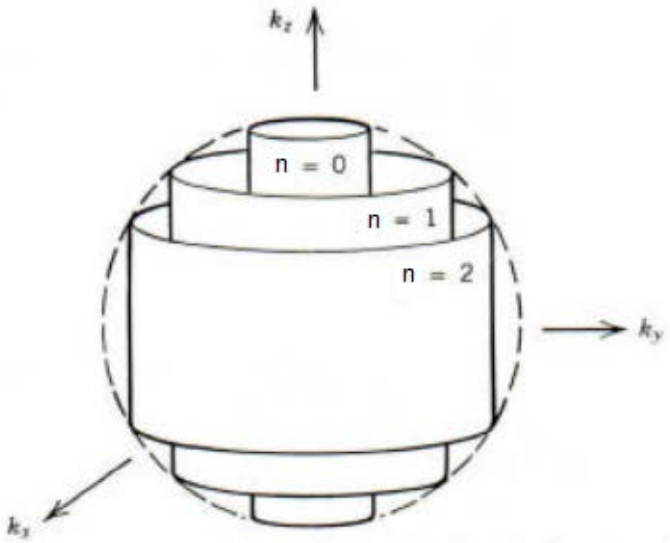

Figure 3-3. Under the application of a magnetic field $|\boldsymbol{B}| = \boldsymbol{B_z}$ electrons are quantized to constant momentum surfaces in k_x, k_y plane. The density of conducting electrons at the Fermi energy is modulated as Landau levels pass through extrema in the Fermi surface perpendicular to the applied field.

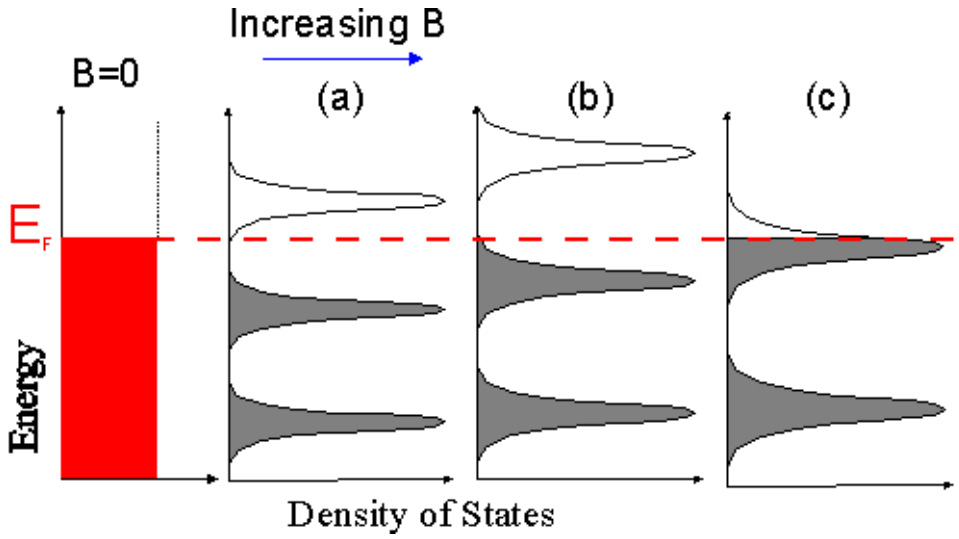

Figure 3-4. Occupation of Landau levels as a function of energy. In (a) and (b), there are no electrons at the Fermi energy leading to an insulating state (quantum Hall state). As the field continues to increase, Landau levels move through the Fermi energy, forming a metallic state.

The SdH frequency is proportional to the size of extremal cross sections of the Fermi surface in the plane perpendicular to the applied field through the LK formula for oscillation frequency,

$$f = \frac{\hbar}{2\pi e} S(\theta), \tag{3.4}$$

where $S(\theta)$ is the Fermi surface extremal cross section perpendicular to the magnetic field direction. The dependence only on extremal cross sections means for spherical or elliptical Fermi surfaces (for instance) there will be a single SdH oscillation amplitude observed at any particular angle while more complicated Fermi surfaces will show multiple frequencies. For 2D Fermi surfaces (cylindrical), all electrons at the Fermi surface have the same $k_{xy} = \sqrt{k_x^2 + k_y^2}$. This allows Landau levels to form an insulating state for well separated levels leading to the quantum Hall state discussed earlier. A 3D Fermi surface, however, will continue to have electrons at the Fermi energy even as the separation of electrons into Landau levels removes electrons from the Fermi energy in the k_{xy} plane as is seen in Fig. 3-3.

While SdH oscillations only measure the extremal cross section of the Fermi surface, much more meaningful information about the Fermi surface may be extracted if certain assumptions are made. Assuming a linear energy dispersion, the SdH frequency relates to Fermi surface size through the linear energy dispersion relation $E_F = v_F \hbar k_F$; where $\hbar k_F$ is the electron momentum and v_F is the Fermi velocity. Considering a Dirac-type band dispersion, we may consider E_F=0 at the Dirac point for simplicity. In the case of a non-linear band dispersion, we can still extract information about the Fermi energy if we include a more accurate model of the band dispersion. This is used with the LK formula for oscillation frequency to determine the Fermi energy. For circular cross sections, $S(\theta)$ is expressed in the reciprocal space as $S = \pi {k_F}^2$. The effective mass

is found by fitting the temperature-dependent amplitude of oscillations, and relates to the band structure through

$$m^* = \frac{\hbar^2}{2\pi}\frac{\partial \mathrm{S}}{\partial \mathrm{E}}. \tag{3.5}$$

These relations are used to calculate the Fermi energy above the Dirac point by measuring the temperature dependence of the SdH frequency using

$$E_F = v_F \hbar \mathrm{k}_F \tag{3.6}$$

$$v_F = \frac{(2e\hbar \mathrm{f})^{1/2}}{m^*} \text{ and } k_F = \left(\frac{2ef}{\hbar}\right)^{1/2}.$$

Due to the linear dispersion of surface states at the Dirac point combining with the extrema of bulk states in Bi_2Se_3 near the Dirac point, these estimates can represent a good estimation of the minimum energy above the Dirac point, even when the conduction is dominated by bulk electrons. This estimate's correspondence to the actual size of the Fermi surface will break down for high-energy states of the bulk conduction band where there is significant deviation from the modeled band structure. Nonetheless, this represents an estimation of the Fermi energy for a particular cross section.[41,42]

3.2 MAGNETIZATION

Magnetization measurements were performed using a Quantum Design AC measurement system (ACMS). An ACMS measurement coil is pictured in Fig. 3-5. Magnetization was determined using AC susceptibility. After loading, samples were placed in a DC field, typically ranging from 50 to 200 Oe, modulated with an AC field of 10 Oe at 1000 Hz. Magnetization was determined using the inductance of a secondary detection coil centered around the sample. When the sample temperature is lowered below T_c, samples entering the superconducting state become diamagnetic, creating negative magnetic susceptibility. H_{c1} is measured as the point at which magnetic field begins to enter the superconducting state and is most easily observed if diamagnetism is saturated regardless of superconducting phase fraction. H_{c2} is measured as the field value when the superconducting state is completely lost and the magnetic susceptibility is the same as that of the normal state above T_c.

Figure 3-5. Quantum Design ACMS probe

3.3 CRYSTAL DIFFRACTION

Numerous diffraction techniques are employed to probe the structure of materials after synthesis. All crystal diffraction techniques exploit scattering from atomic positions, although the

atomic scattering factors for different radiation may differ, e.g. x-ray, electrons, and neutrons. X-rays primarily interact with the electron cloud, electrons interact with the electric potential of the nucleus, and neutrons interact with the nuclei via nuclear forces.[43–45] For samples of FeTe, powder XRD (x-ray diffraction) was primarily used to determine the crystal symmetry and bulk atomic lattice parameters to probe the structure of samples. X-ray diffraction (XRD) of powdered samples is a standard characterization technique for crystal structure due to the fast acquisition times and illumination of many randomly oriented particles. This allows an averaging of many particles and allows a determination of the phase concentrations, particle size, lattice strain, and many other statistical factors. However, powder XRD is not ideal for structural determination in many cases, including Bi_2Se_3 crystals. Mechanically sensitive samples such as Bi_2Se_3, cannot be powdered due to low crystalline stability, nor is XRD ideal for the detection of weakly scattering phases, including superstructures, charge density waves, and low dimension phases. On the other hand, selected area electron diffraction (SAED) utilizing a transmission electron microscope (TEM) addresses many of these issues.

3.3.1 Transmission Electron Microscopy

The physics of diffraction in an electron microscope is very similar to diffraction via XRD with the same basic stages, as is simplified in Fig. 3-6. Firstly, particles are excited to a uniform energy. In XRD this is done via emission of photons from excited atomic energy levels and selected via a diffracting monochromator. In most lab-based XRDs this is typically a Cu-Kα photon with wavelength λ=1.5406 Å. In a TEM, electrons are accelerated using an electron gun, typically 300 keV (λ= 1.97 pm) for inorganic materials. Next the particles are collimated, using apertures and Soller slits or electromagnetic lenses for XRD and TEM respectively. After

interaction with a sample, the diffracted particles are detected, commonly via CCD camera. These systems have many notable differences including the wavelength and charge of diffracting particles, illuminated area, and beam optics.

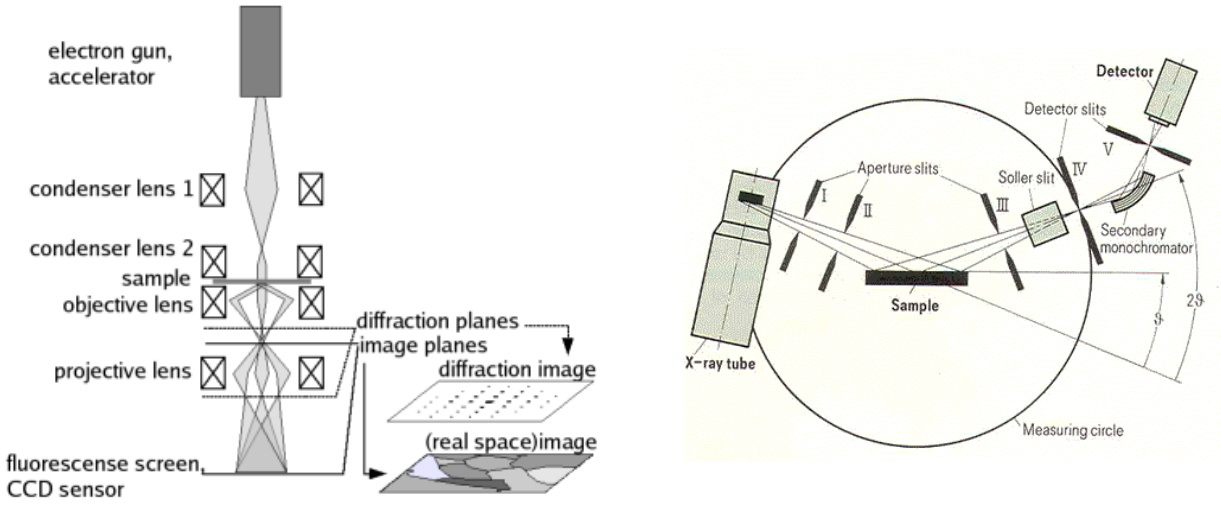

Figure 3-6. Simplified schematic of TEM and powder XRD systems.

The much higher energy of electrons in a TEM has many physical effects on diffraction, including the introduction of multiple scattering, which can make otherwise forbidden reflections present. While the inelastic scattering can complicate analysis by modifying scattering intensities, it can also reveal additional atomic spacings which may not be apparent in XRD. Differences in illuminated area also have a strong effect on the types of atomic periodicities that are detectable. In a TEM, a SAED aperture allows diffraction from only a small thin region of a sample, typically of dimension 10μm to 1 nm. Diffracting electrons need to transmit through the sample to be detected in a Laue geometry, unlike a lab based powder XRD for which photons scatter off the atomic planes of the sample, typically in a Bragg geometry. This restriction limits the size and quantity of particles which are used for diffraction but allows diffraction from single crystals of extremely small volume. The ability to diffract from a single small crystal provides greatly

increased signal to noise ratios, allowing for the detection of structures with weak scattering. Finally, the optical system of a TEM provides the ability to image samples in real space, instead of only performing diffraction, allowing for the analysis of non-periodic defect structures (e.g. crystal domains). TEM optics also extract a 2D diffraction pattern, like Laue XRD, rather than rotationally averaged diffraction patterns of many particles from powder XRD. Specific details on how these techniques were used to determine structural details in the FeTe and Bi_2Se_3 system are discussed in later sections.

4.0 BISMUTH SELENIDE

Bi_2Se_3 is part of the so called "second generation" of topological insulators which have larger band gaps, and simpler surface states than the first 3D topological insulators found.[46] The first generation of a 3D topological insulator was $Bi_{1-x}Sb_x$ for $0.07 < x < 0.22$ and while it was a revolutionary discovery, many challenges exist for this material in both the understanding of the physics of topological insulators and its potential for applications.[47] The alloyed nature of $Bi_{1-x}Sb_x$ makes the maintenance of elemental homogeneity difficult, unlike Bi_2Se_3's existence as a stoichiometric compound. Bi_2Se_3 is driven towards chemical homogeneity due to the unique locations of bismuth and selenium in its structure. This is unlike alloys which generally form with varied stoichiometry through crystallization. Additionally, Bi_2Se_3 only has a single topological band crossing, giving it the simplest band structure for a topological material, whereas the surface bands of $Bi_{1-x}Sb_x$ cross the Fermi energy 5 times. While a material will remain topologically nontrivial for any odd number of crossings, a large number of crossings makes the study of the topological state particularly difficult due to the differences in electron characteristics at band Dirac points occurring at different symmetry locations. Finally, Bi_2Se_3 has a much larger bulk bandgap than $Bi_{1-x}Sb_x$, reported in excess of 0.3 eV.[38] This relatively large band gap allows for protection of surface states above room temperature.

The non-trivial topological state of Bi_2Se_3 depends on many material characteristics, but is robust due to protections from relatively insensitive parameters including the crystal structure and spin orbit coupling parameters. In Bi_2Se_3, the topological state is protected by time-reversal symmetry of the Hamiltonian, meaning it will remain protected under non-magnetic disorder, although magnetic fields or magnetic impurities will break the topological state, and open a gap in

the surface states at the Dirac point. Magnetic impurities allow for scattering to induce a spin flip, and a continuous electronic state across what would otherwise be a time-reversal-invariant point in momentum space. The discovery of superconductivity in Bi_2Se_3 under atmospheric pressure allows the manifestation of all the properties of a topological superconductor previously discussed.

4.1 SUPERCONDUCTIVITY

Copper-intercalated bismuth selenide ($Cu_xBi_2Se_3$) is confirmed by many groups as a superconductor that becomes superconducting only under specific quenching conditions during synthesis. Other groups have studied the range of quenching temperature that leads to superconductivity and generally found to it to be between 560-620 °C with some reports of superconductivity occurring when quenched just below the melting point of Bi_2Se_3.[48] This work studies the effects of quenching on $Cu_xBi_2Se_3$ (x=0.12) to determine the effects of quenching on electronic and crystal properties and how the superconducting and topological states are impacted.

4.1.1 Magnetization

Temperature-dependent magnetization (MT) of samples quenched at 620 °C found a superconducting transition at 2.9 K shown in Fig. 4.1. No superconducting transition was detected for unquenched samples. Magnetization was performed by AC method with a 200 Oe DC field modulated by 10 Oe at 1000 Hz. The in-phase magnetization signal (M') is plotted as electromagnetic units/gram (emu/g).

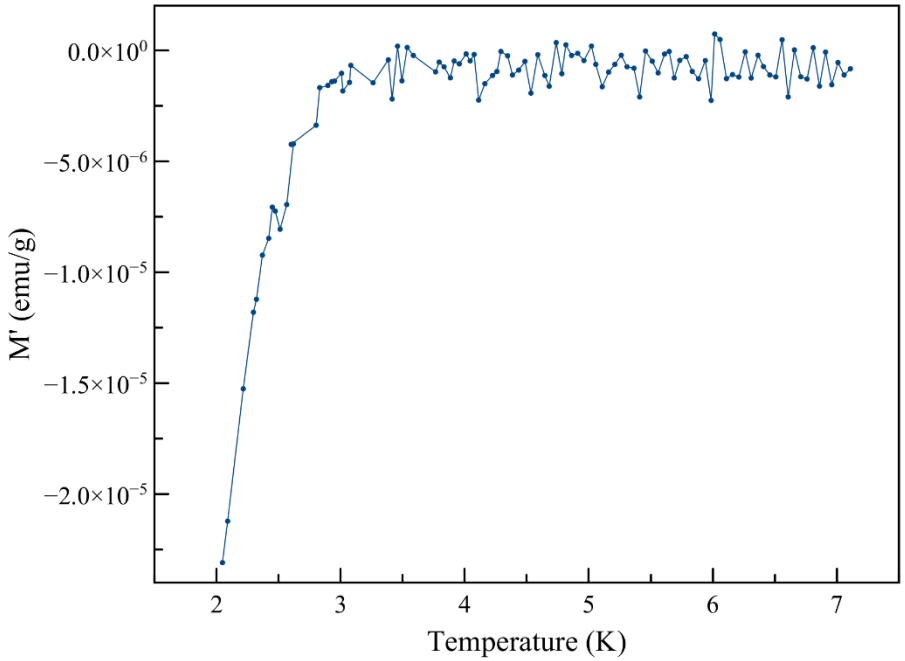

Figure 4-1. Magnetization vs. Temperature of $Cu_{0.12}Bi_2Se_3$ quenched at 620 °C.

Magnetization vs. applied magnetic field (MH) shown in Fig. 4-2 was also measured to determine the critical field of the superconducting state. MH measurements reveal a surprisingly low critical field, which brings most of the sample into a normal state at fields above ~100 Oe (10 mT). The weak critical fields suggest a T_c measured via magnetization will be closer to the resistive T_c of 3.2 K if weaker fields are used. While H_{c1} is difficult to quantify in these measurements due to the very low critical fields, H_{c2} is also difficult to determine due to the broad transition in MH measurements and the diamagnetic normal state of the material.

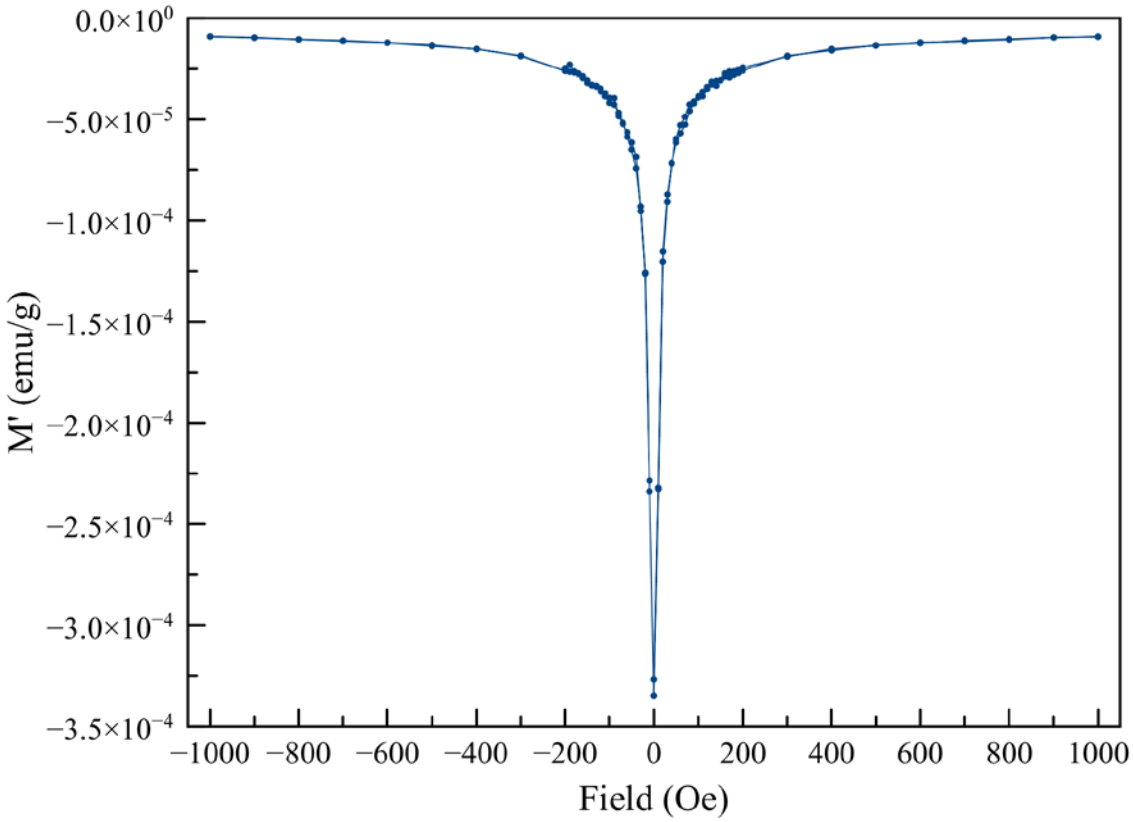

Figure 4-2. AC magnetization vs. magnetic field of $Cu_{0.12}Bi_2Se_3$ quenched at 620 °C.

4.1.2 Resistivity

While the superconducting state appears weak to applied magnetic fields, resistive data are surprisingly robust in comparison. Resistive data indicate a critical field (H_{c2}) of ~2.8 T at 0.3 K using an applied current of 1 mA. This difference has many possible origins, but many relate to measurements of magnetization as a bulk effect, while resistivity only gives an indication of total supercurrent through the sample leading to a drop in resistance. The relation of resistivity drop to superconductor volume is complicated by uncertainty in the shape of superconducting channels. The changes in resistivity and magnetization, combined, imply that the superconducting volume

fraction is not uniform due to the broad transitions in temperature, with small areas resistant to high magnetic fields while the bulk of the sample is driven into the normal state. While we expect a saturation of resistance and magnetization at low temperatures, H_c is strongly correlated with the critical current density (J_c), meaning larger applied currents will generate correspondingly smaller critical fields (and temperatures). This relation of critical current to field is due to the generation of the screening currents which expel magnetic fields.[49] A critical field of 100 Oe implies a critical current of ~3 mA for a 1 mm^2 cross section which is on the same order of magnitude as the 1 mA which was used in this sample. The sample used was of dimension ~ 1x5x5 mm^3, but uncertainty in the size of the superconducting channels makes a calculation of the actual current density impossible.

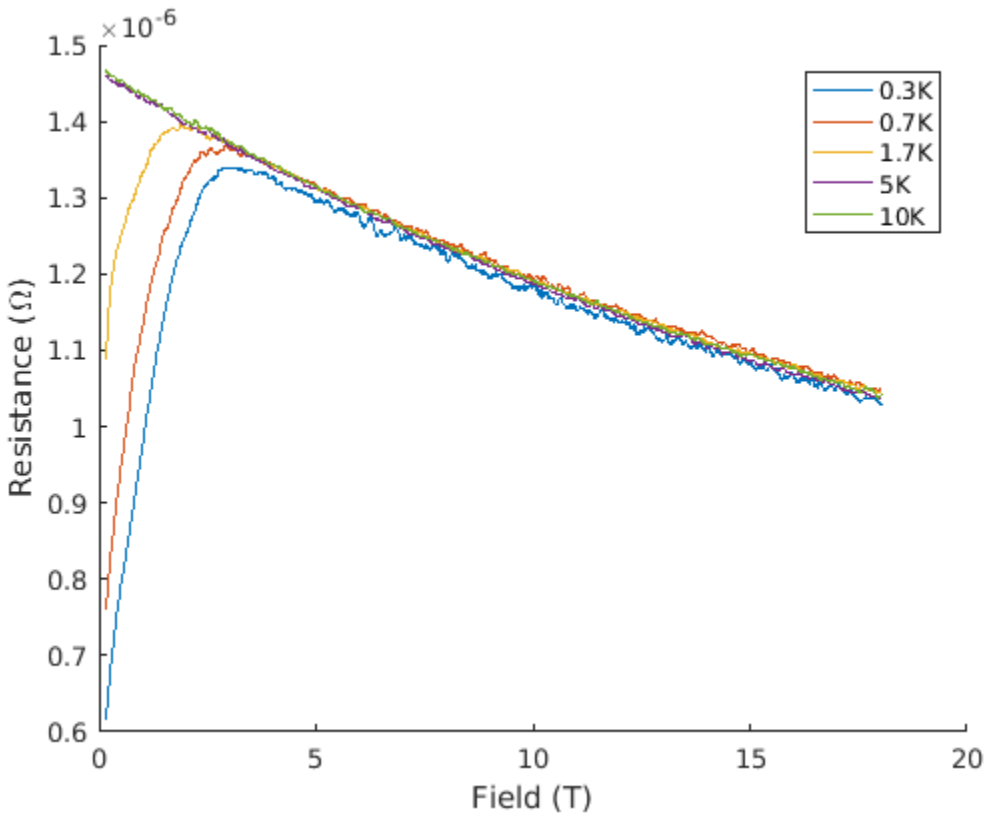

Figure 4-3. Magneto-resistance curves of $Cu_{0.12}Bi_2Se_3$ quenched at 620 ºC.

In this sample, inhomogeneity impeding the formation of superconductivity is likely due to crystal defects and finite-size effects. Lattice constants, intercalated copper, and chemical potential are unlikely to cause this inhomogeneity due to the uniformity of the Fermi energy found throughout the sample which is discussed later in the analysis of SdH oscillations. Further measurements of critical fields H_{c1} and H_{c2} through magnetization and resistive measurement will be able to shed some information on the influence of filamentary superconductivity based on the shape of the superconducting dome.

Samples are dependent on quenching to generate the superconducting state, which has been found to influence volume fractions, but not transition temperatures.[34] The total resistance drop in the samples presented here is ~63% at 350 mK. While this means the sample is not completely homogenous, this represents a greater volume fraction than found in many other reports, and all other reports that were able to measure SdH oscillations.[42,50,51]

4.2 STRUCTURAL ANOMALIES IN COPPER-INTERCALATED BISMUTH SELENIDE

TEM diffraction (SAED) of $Cu_xBi_2Se_3$ in Fig. 4-3 (a) generally shows pristine crystals with a high degree of hexagonal symmetry (R-3m:H space group), indicating the most areas have crystalized uniformly due to the slow cooling rate during crystallization. Preparation of TEM samples was performed via a combination of ion milling and mechanical exfoliation, which is able to thin the samples sufficiently without the formation of additional phases, unlike mechanical grinding. The most common defect seen is the appearance of satellite peaks, generally indicating

improper stacking of atoms. These regions are the result of either a local stretching of atomic lattice due to some crystal defect or other inhomogeneity, or peaks from a different zone axis, appearing due to the relative tilt of a smaller crystal domain. Occasionally, satellite peaks resembling a charge density wave (CDW) ordering are seen, as in Fig. 4-3 (b). This type of charge ordering is commonly seen in various layered dichloride systems, e.g. 1T-TaS_2.[52,53] The origin of CDWs in Bi_2Se_3 is not definitively known at this time, but some relevant explanations to this system are notable.

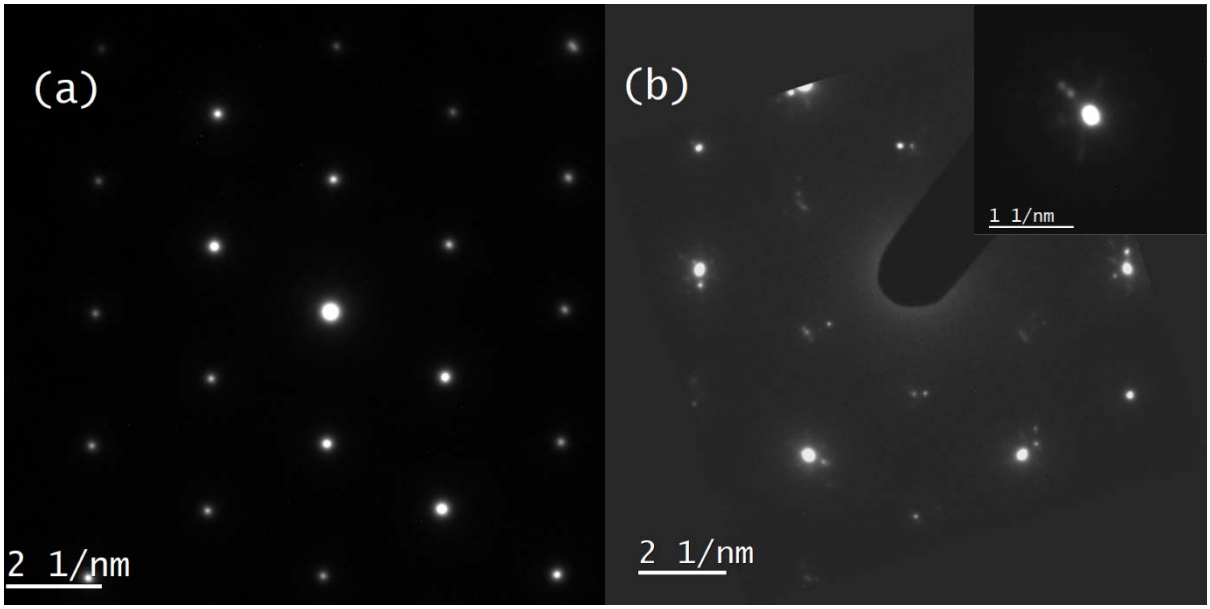

Figure 4-4. SAED patterns of unquenched $Cu_{0.12}Bi_2Se_3$.

4.2.1 Charge Density Waves

In some cases, CDW waves are interpreted as an ordered defect structure. Here, a minority region of the sample has slightly modified **a** and **b** lattice parameters, which are close enough to allow the minority lattice to match the host crystal in some areas through a flexibility in atomic bonding distances. This causes a buildup of stress in the crystal structure, which is concentrated

into regions where the bond distance can relax, causing a regular modulation of crystal lattice parameters. In $Cu_{0.12}Bi_2Se_3$ the inhomogeneity in local structure is most likely caused by the copper intercalant. While copper is intended to intercalate with uniform, random order into the van der Waals gap, this is most likely not the case, as the interaction of inhomogeneous copper intercalation with the lattice can cause the satellite peaks and CDWs. High concentrations of copper (x>~0.15) during the crystallization of $Cu_xBi_2Se_3$ are known to cause the substitution of bismuth in the form of $Cu_{x-y}(Bi_{2-y}Cu_y)Se_3$.[54] Excess bismuth from this substitution can form a Bi-Cu alloy and the parent phase can decompose into Cu_2Se.[55,56] These compounds will invariably form defects, and while these compounds were not observed via diffraction, their presence is also possible in a disordered form at grain boundaries. The effect of metallic intercalation on bulk a-b lattice parameters is not known in Bi_2Se_3 but has negligible effects in similar structures, e.g. Bi_2Te_3.[57] Even so, the sensitivity of the Bi_2Se_3 phase to mechanical deformation may indicate a difference in Bi_2Se_3 from the isostructural Bi_2Te_3 system. Due to the lack of flexibility of a-b parameters of the Bi_2Se_3 structure, CDW ordering is likely caused by ordering of the copper intercalant itself, rather than a direct effect on the host lattice. Near the intercalation density in question, (x=0.12) at least some metallic bonding is likely to begin. As copper acts as a charge donor to the system, copper atoms will share the conducting electrons, creating an attractive force between intercalating atoms and crystal defects. Due to the low density of intercalant, some amount of copper mobility is expected, similar to the case of mobile Fe intercalant in $Fe_{1+d}Te$ discussed later. CDWs may also form without inhomogeneity causing a lattice mismatch.

A common explanation for the formation of CDWs is the nesting of wave-vectors on an adjacent (cylindrical) flat surface of the Fermi surface.[58–60] This type of Fermi surface is theorized to manifest in Bi_2Se_3, although it is not observed in our measurements via SdH oscillations, or in

the work of other groups at the time of this writing.[38] While Fermi surface nesting may explain CDWs in Bi_2Se_3, the theory of nesting causing a CDW wave is much debated at this time, as groups have shown the energies associated with Fermi surface nesting as negligible compared with other energies.[60] Additionally, if Fermi surface nesting is responsible for CDW formation, a temperature-dependent transition into the CDW state should be observed (Peierls transition) but is not known to exist.

CDWs have been observed in Bi_2Se_3 by Koski et al., who found various superstructures and CDW orderings in Bi_2Se_3 nanoribbons with various intercalated zero-valent metals.[61] Interestingly, in cobalt-intercalated samples, CDWs were only found after the sample was heated for 5 min at 250 ºC in vacuum, indicating mobilization of the intercalant is crucial to manifest CDWs in Bi_2Se_3. While we did not observe the same type of orderings seen in Koski's copper-intercalated samples, it is possible the unique ordering observed was influenced by the low dimensionally of Kolski's crystals, or the increased copper concentration possible in copper-intercalated nanoribbons.

Interestingly, samples quenched in the same manner used to induce superconductivity show unique orderings compared to unquenched samples. Firstly, a superstructure ordering was observed as seen in Fig. 4-5(a). The exact form of this ordering is unclear because the ordering was not observable from alternate high-symmetry directions. Secondly, some areas of the sample also exhibited a "stripe" ordering as seen in Fig. 4-5 (b). This crystal is not uniformly ordered in one crystallographic direction, although it remains ordered in the orthogonal direction. This disorder pinned along a crystallographic direction may relate to the anomalous symmetry-breaking of the superconducting state found in some superconducting $Cu_xBi_2Se_3$ samples as observed by

other groups and may explain the proposed "pinning" of the superconducting state along a crystallographic axis in these samples.[62,63]

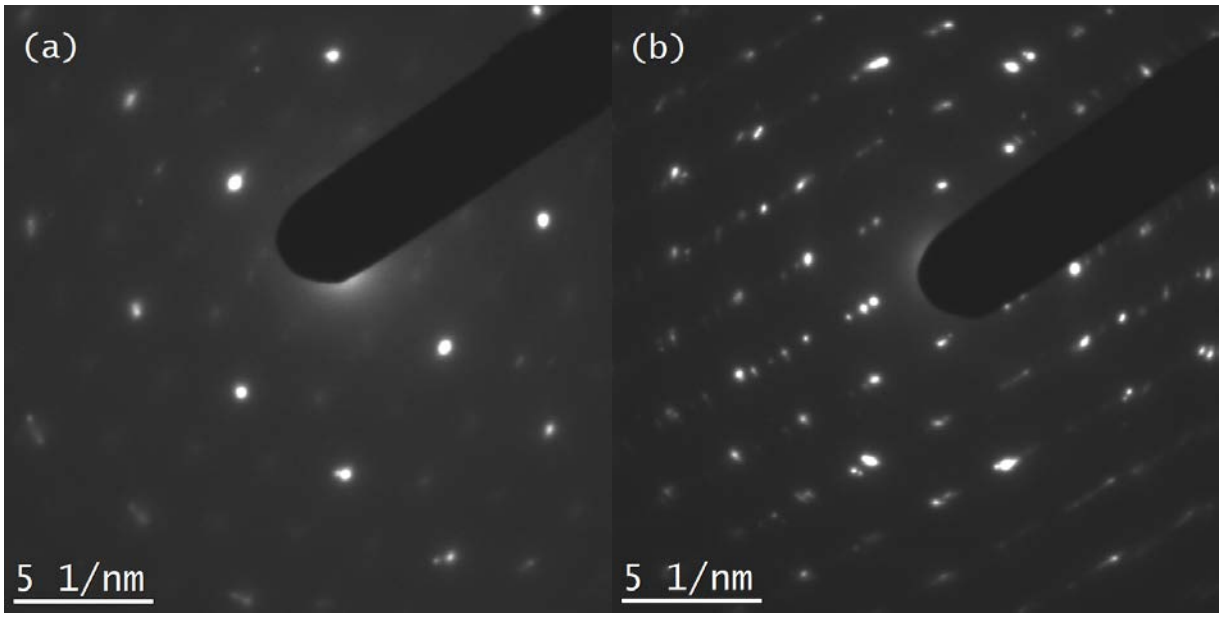

Figure 4-5. SAED of quenched $Cu_{0.12}Bi_2Se_3$.

While it is both advantageous and interesting to study the effects of quenching on copper ordering and CDWs, observation of these atypical, well-ordered phases are inconsistent from sample to sample. This is matched by the relatively low superconducting volume fractions in $Cu_xBi_2Se_3$, weakening any correlation between novel structures and the superconducting state. Further investigations are performed on the electronic properties at high field to determine information on changes in the Fermi surface.

5.0 FERMI SURFACE OF BISMUTH SELENIDE

To more directly observe properties of the superconducting Fermi surface of $Cu_xBi_2Se_3$, investigations were carried out via magneto-resistive measurements of SdH oscillations. Accurate measurements of the Fermi surface of $Cu_xBi_2Se_3$ have gathered much interest due to its relation to topological superconductivity, including the maintenance of the Dirac state in a superconducting material. Specifically, do the topological states remain in a sample that has become superconducting; are these states isolated from bulk states by a Fermi energy in the bulk band gap; and is the origin of superconductivity in the superconducting topological insulator $Cu_xBi_2Se_3$ from pairing of topological surface states, or bulk states? While the most detailed measurements of the Fermi surface are performed by ARPES measurements, there are two main impediments to its full success in this system. Firstly, ARPES is an angle-resolved measurement, which is extremely surface sensitive.[64–66] Because of this, extremely uniform crystalline samples are needed to take meaningful measurements. Unfortunately, samples of superconducting $Cu_xBi_2Se_3$ tend to have low volume fractions, and many crystal defects. This means that even if a region with high crystallinity can be found to give a clear picture of the Fermi surface, there is no guarantee this region is one that exhibits superconductivity. Correlating ARPES measurements with the origin of superconductivity is further complicated by a lack of established differences in structural differences between superconducting and non-superconducting Bi_2Se_3. Additionally, the effective operating temperature of ARPES measurements is generally higher than the T_c of $Cu_xBi_2Se_3$, meaning the superconducting gap is not directly observable with this technique. The most direct way of identifying features of the Fermi surface without ARPES is through the measurement of SdH or de Haas-van Alphen (dHvA) oscillations. SdH and dHvA oscillations

measure the extremal cross section of the Fermi surface, without measuring the Fermi level, or a momentum-energy dispersion. However, this information can still be particularly useful in characterizing the Fermi surface, especially if the momentum-energy dispersion is already known as described in section 3.1.2.

5.1 SHUBNIKOV DE HAAS OSCILLATIONS

The following study of the dependence of quenching on the Fermi surface is performed using samples quenched from the minimum and near-maximum temperature that superconductivity is known to occur. Sample 1 was quenched from 620 °C and sample 2 was quenched from 560 °C. samples labeled with "a" and "b" are single crystals of size ~5x5x1 mm^3 extracted from the same boule. Magnetoresistance (MR) curves at 0.35 K exhibiting SdH oscillations are shown in Fig. 5-1, and the results of fitting MR curves in Table 1. These results show a higher Fermi energy in samples quenched from higher temperature. One can see in the background-subtracted data in Fig. 5-3 the amplitude of oscillations is also much smaller for sample 1 than sample 2, which is discussed later. Sample 1 had a much greater SdH frequency than sample 2 indicating a much larger Fermi surface cross-section in the superconducting sample. This is likely due to the Fermi energy of the non-superconducting sample being closer to the Dirac point than the superconducting sample, assuming the linear dispersion of the bands found through ARPES measurements.[41,42,67] While a superconducting transition is not observed in all samples, this is attributed to the small superconducting phase fractions generally found in these types of samples, as is commonly reported in literature.[34] Nonetheless, the single frequency of oscillation observed in Fig. 5-2 indicates a defined Fermi surface and homogenous structure.

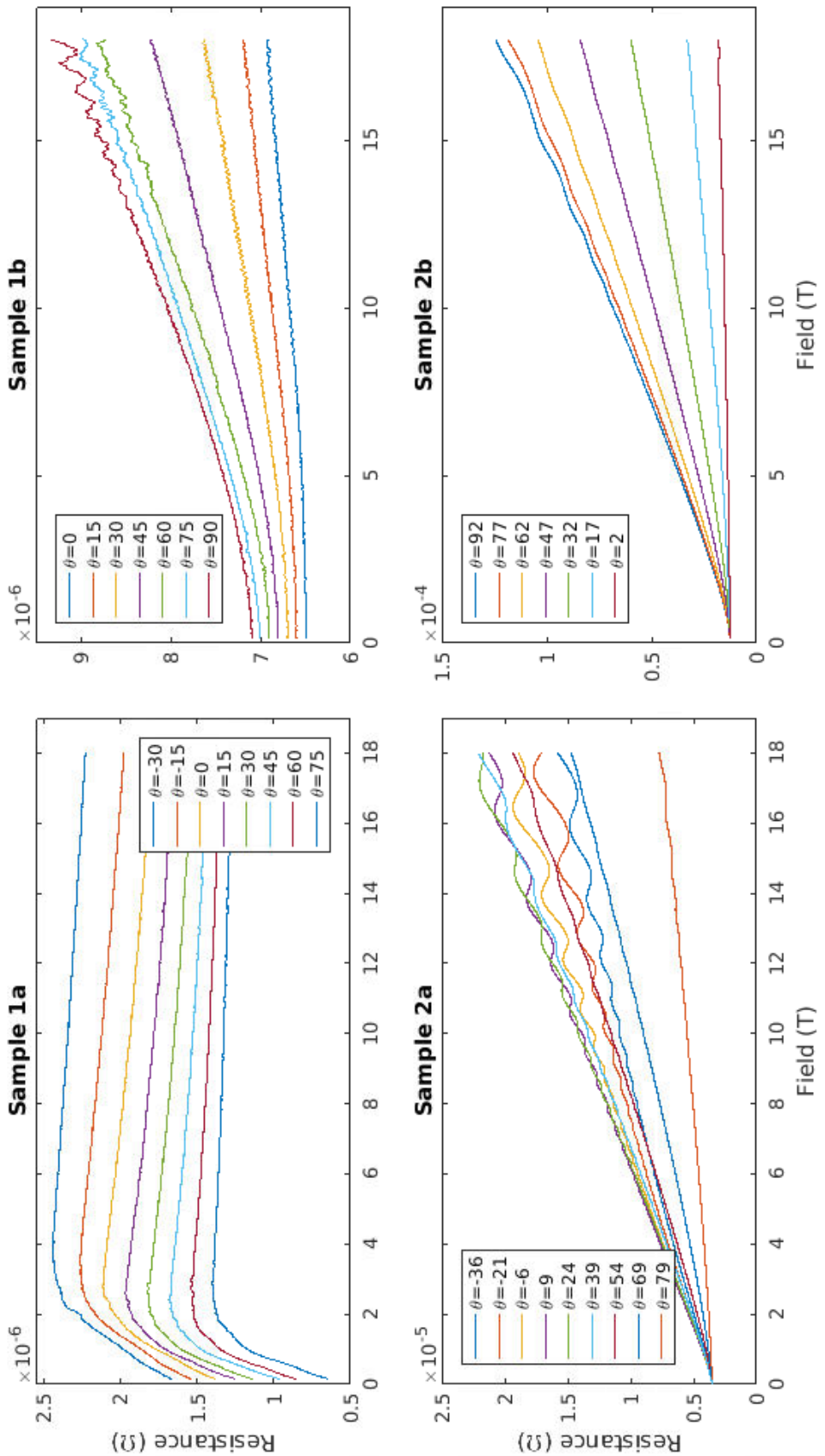

Figure 5-1. Magnetoresistance curves of $Cu_{0.12}Bi_2Se_3$ at 350 mK.

Sample	1a (SC)	1b	2a	2b
F (T)	378.8	370.4	89.9	91.9
m^* (m_e)	-	-	0.119	0.165
Δm^* (m_e)	-	-	0.03	0.052
k_f (Å $^{-1}$)	1.07	1.06	0.52	0.53
v_F (m/s)	8.87E+05	8.77E+05	5.08E+05	3.71E+05
E_F (meV)	626.14	612.62	174.82	128.89
T_D (K)	26.32	44.3	15.39	19.96
ΔT_D (K)	9.27	16.43	1.22	1.3
τ_s (s)	4.62E-14	2.74E-14	7.89E-14	6.09E-14

Table 1. Modeled parameters of SdH oscillations in $Cu_xBi_2Se_3$ samples.

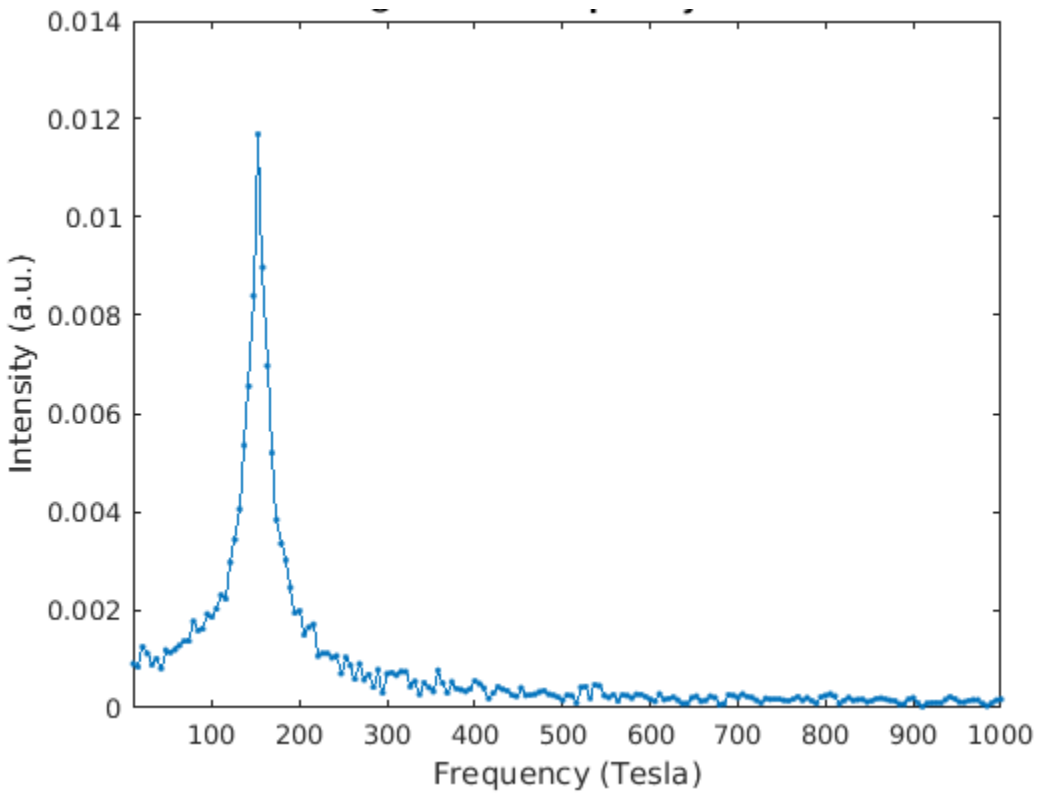

Figure 5-2. Fourier transform of magnetoresistance curve of $Cu_{0.12}Bi_2Se_3$ quenched at 560 °C.

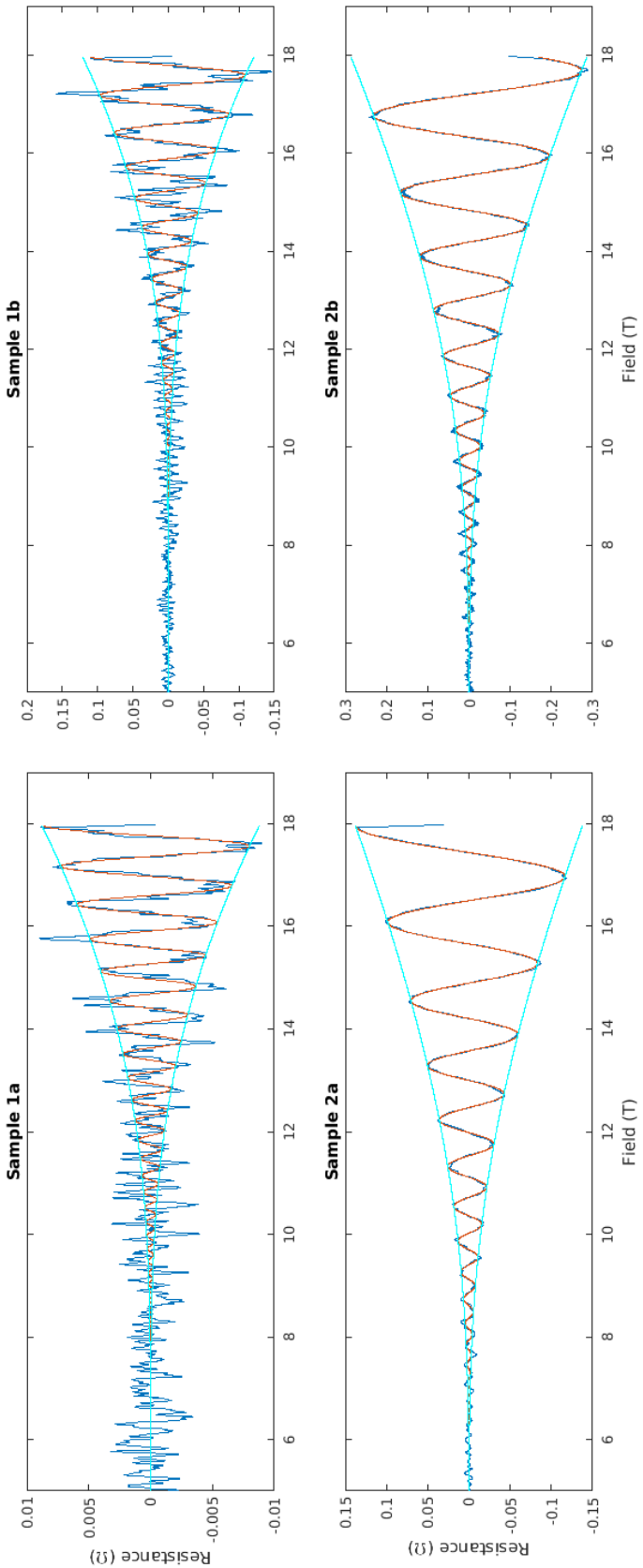

Figure 5-3. SdH fits of $Cu_{0.12}Bi_2Se_3$ samples. Raw data is blue, best fit of oscillations is orange, and envelope of oscillation is cyan.

The appearance of SdH oscillations in the samples indicates the electrons travel through the sample with small enough scattering to preserve a coherent electron energy. In principle these may be topological or bulk electrons, so long as the scattering-induced energy broadening $\hbar/\tau$ is smaller than the Landau level spacing $\hbar\omega$, where τ is the scattering time constant and ω is the cyclotron frequency.[68] In a TI, topological properties protect electrons from scattering, whereas there is no such protection in the conducting phase.[6,69,70] It is observed that in samples with a higher Fermi energy, the electron density and conductance increase, while electron mobility μ is reduced.[42,50] This is likely due to an increasing fraction of conduction electrons occupying bulk electron states instead of topological states. In this manner, the diminished amplitude of oscillations in the superconducting sample is an indication that a larger fraction of electrons is occupying bulk states that are not protected from scattering, due to the increased Fermi energy. Analysis of the oscillation frequency by Fourier transform in Fig. 5-2 and SdH fitting in Fig. 5-3 shows a single oscillation frequency. Exact frequencies were found by fitting background-subtracted curves to the LK formula (Fig. 5-3); f=378.8/370.4 T for sample 1a/1b, and f=89.9/91.9 T for sample 2a/2b, respectively.

Calculating the Fermi energies of the surfaces using the technique by Fang et al. yields E_F=626 eV/613 eV for sample 1a/1b and 175 eV/129 eV for sample 2a/2b, respectively.[71] The ARPES data of Analytis et al. show the distance from the Dirac point to the Fermi energy in Bi_2Se_3 is ~155 meV indicating the non-superconducting samples lie near the bottom of the bulk conduction bands, while the Fermi level of the superconducting sample is well into the bulk conduction bands.[41] If bulk states are needed for superconductivity, this suggests oscillations in superconducting samples will have a frequency f >90.7 T given an effective mass of 0.136 m_e. Indeed, superconducting samples in the literature have an SdH or dHvA frequency f>300 T, while

non-quenched, non-superconducting samples have a much lower frequency.[42,50,72] This indicates the Fermi level must be well into the bulk states for superconductivity to appear, suggestive of bulk electrons leading to superconductivity rather than topological ones.

5.1.1 Electron Mass

The effective mass (m^*) was determined by fitting the temperature dependence of the modeled amplitude of oscillations of data sets at 18 T and 0 degrees of tilt. Amplitudes are plotted in Fig. 5-4. This analysis yielded m^*_{2a} = (0.165 ± 0.030) m_e, and m^*_{2b}= (0.119 ± 0.012) m_e for samples 2a and 2b, respectively. The effective mass for sample 1a/1b was not measured due to the narrow range of tilt for which SdH was observed leading to a lack of temperature-dependent data. Because these masses are in line with reports by Vendelev et al. and Lawson et al. which found little difference of effective mass between $Cu_xBi_2Se_3$ and Bi_2Se_3 samples, the effective mass $m^*=0.136\ m_e$ is used for modeling SdH oscillations and calculations of electron characteristics in the superconducting sample and calculated electron characteristics shown in Table 1.[41,73]

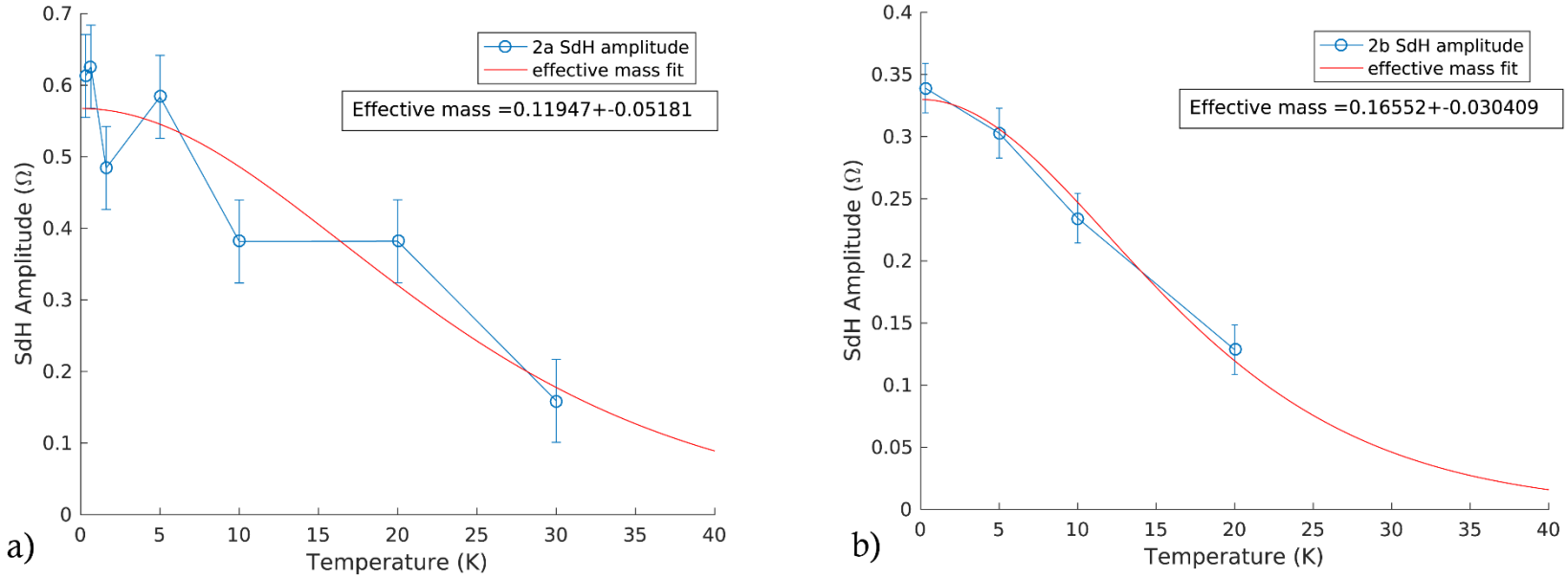

Figure 5-4. Effective mass plots of $Cu_{0.12}Bi_2Se_3$ quenched at 560 °C.

5.1.2 Fermi surface shape

The Fermi surfaces of samples 2a and 2b are well fit (Fig. 5-5) to an ellipsoidal Fermi surface using $f(\theta) = f_o\left(sin^2(\theta) + (e)^2 cos^2(\theta)\right)^{1/2}$, where $e = k_F^x/k_F^z$ with eccentricity e_{2a}=0.585 and e_{2b}=0.563, confirming the 3D nature of conduction electrons in these samples. Very few angles yielded oscillations for the superconducting sample, leaving the shape of the Fermi surface in the superconducting sample ambiguous. Other groups have found a quasi-2D Fermi surface for electrons with similar Fermi cross-sections, with a more limited range of measurable frequencies at high rotation angles.[42,50,51,73] A 2D Fermi surface has a diverging cross section, leading to an inability to measure a frequency at all angles. Our data show a measurable frequency

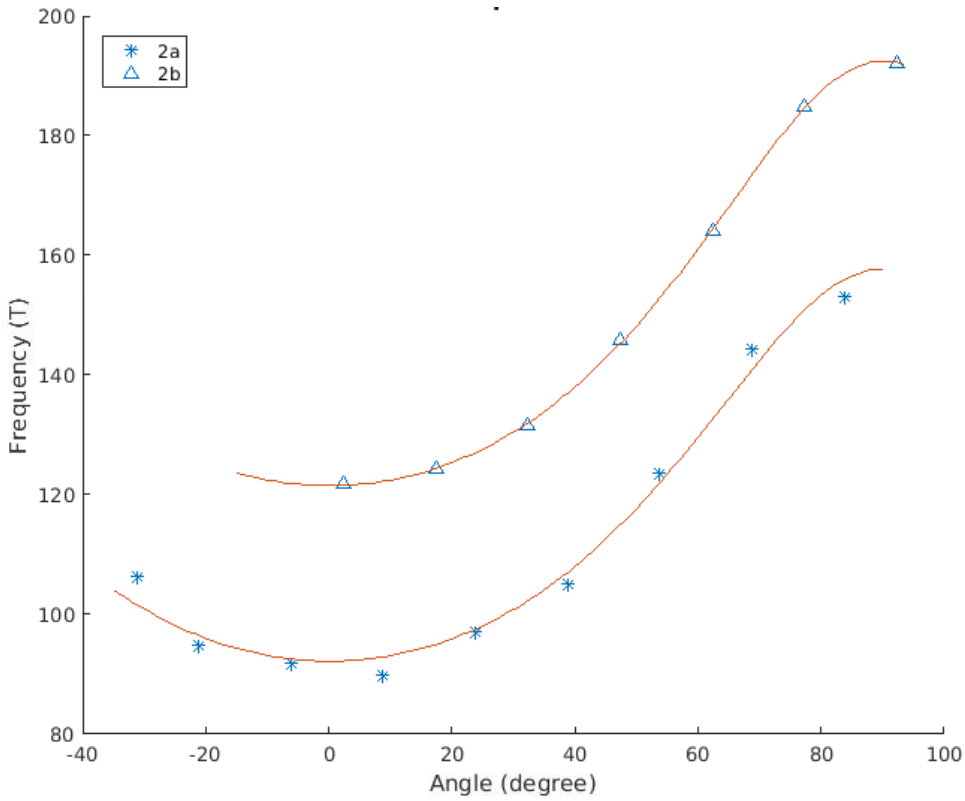

Figure 5-5. Ellipsoidal fit of Fermi surface shape for samples 2a and 2b. Data points for sample 2b are shifted up by 30 Tesla for clarity.

through a maximum frequency, making the shape of the cross section unambiguous. Regardless of the Fermi surface shape, these electrons in superconducting $Cu_xBi_2Se_3$ can be confirmed as originating from bulk states, due to the large cross-section, indicating an increased Fermi energy.

5.1.3 Electron mobility

To find the Dingle temperature (T_D), the maximum amplitude of oscillations at 0.3 K was modeled to the non-oscillatory component of the LK formula manipulated to the following form:

$$\ln\left(AB^{-1/2}\sinh\left(\frac{\alpha m^* T}{B}\right)\right) = Const. - \frac{\alpha m^* T_D}{B} \quad . \tag{5.1}$$

The slope of the data set plotted vs. 1/B then relates to the slope as $-\alpha m^* T_D$. Dingle temperature fitting is shown in Fig. 5-6 and tabulated with uncertainty ΔT_D in Table 1.

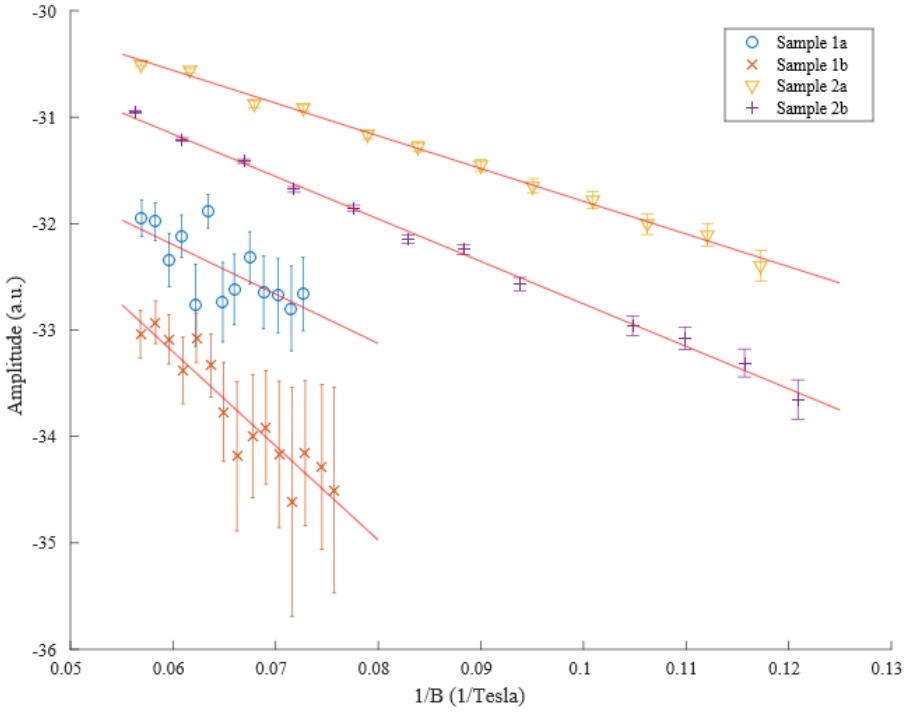

Figure 5-6. Dingle plot of $Cu_{0.12}Bi_2Se_3$ samples.

This dataset suggests a higher Dingle temperature in the superconducting sample consistent with a shorter scattering time, although with a high margin of error due to the small amplitude of SdH oscillations. A higher Dingle temperature in the superconducting sample indicates quenching incites crystal defects which may contribute to the increased Fermi energy. This is at odds with the general properties of superconductors for which a shorter scattering time, and lower electron mobility, are generally negative impacts on the superconducting state.[74–76] Additionally, quenching generally results in smaller grain sizes and higher defect density, hampering the superconducting state.[77,78] However, in $Cu_xBi_2Se_3$, the crystallographic stress induced from quenching is an important factor in the emergence of superconductivity, likely due to the elevation of the Fermi level and population of bulk electron states.

5.1.4 Effect of Quenching

While the Fermi energy in Bi_2Se_3 is raised by copper intercalants charge-doping the system, quenching is also necessary in the onset of the superconducting state, as all samples in this study had the same nominal stoichiometry, and no copper-intercalated samples are known to superconduct without a quenching treatment. Intercalated copper is thought to induce superconductivity by raising the Fermi energy. However, few other intercalated elements are known to induce superconductivity in Bi_2Se_3, even though the Bi_2Se_3 crystal phase is generally very sensitive to copper stoichiometry. Samples with Cu_x below $x < 0.10$ are nonsuperconducting, and samples with too much copper can lead to substitution of bismuth and formation of copper selenide instead of intercalation.[79] This research shows that quenching induces superconductivity by raising the Fermi energy independently from adding additional copper into the system, which causes phase degradation. It is noteworthy that in our experience,

samples with higher concentration of copper have more dislocations, as evidenced by the surface finish after cleaving, are more "stressed", indicated by difficulty in maintaining a pure phase after grinding, and are less stable in air.[80] Increased defect density indicates that the inclusion of copper, in addition to donating conduction electrons, acts as a crystal stressor similar to quenching. Indeed, Schneeloch et al. has found the greatest phase fraction from a "furnace cool-quench" preparation, indicating the importance of both phase stabilization and quenching stress to induce superconductivity.[34,81]

A fast quench from high temperature is needed to induce superconductivity in $Cu_xBi_2Se_3$, which is correlated with an increase in Fermi energy, although the relation between the increase in Fermi energy and superconductivity is not immediately clear. The most direct effect of raising the Fermi energy in Bi_2Se_3 relates to increasing the DOS at the Fermi energy. This will dramatically increase the T_c of the superconducting state, especially if the pairing of superconducting electrons depends on the density of electrons being exponential as found in other systems.[82,83] In Bi_2Se_3, the change in the DOS upon raising the Fermi energy is particularly dramatic when the Fermi energy is ~600 meV above the Dirac point.[38] At this energy, the bulk bands near the Γ point combine with bulk states between the $\Gamma - M$ point. If the superconducting states only pair across the Γ point, and no pairing occurs in the side bands, as is generally the case, this would result in a rapid increase in the DOS available for superconducting electrons. This rapid change would not be clearly apparent in measurements of carrier concentration since the net DOS would still change continually upon increasing the Fermi energy.

5.2 LINEAR MAGNETORESISTANCE

In addition to differences in Fermi cross-section, large differences are seen in the magnetoresistance (MR) of Samples 1 and 2 from typical materials which exhibit a change in conductance $\Delta\sigma \propto B^2$. Several conflicting theories have been proposed to explain the linear magnetoresistance (LMR) found in Bi_2Se_3 with generally inconsistent or incomplete explanations. Here, we will clarify the factors which lead to LMR in bulk $Cu_xBi_2Se_3$ samples.

5.2.1 WAL-WL crossover

The background function of MR can be well fit to the Lu-Shi-Shen (LSS) formula for magneto-conductance, modeling a crossover from weak anti-localization (WAL) to weak localization (WL). Assuming the inelastic scattering time is much longer than the spin-orbit and elastic scattering times, the change in conductance can be modeled using a modified version of the HLN equation

$$\Delta\sigma = \sum_{i=0,1} \frac{\alpha_i e^2}{2\pi e\hbar}\left[\psi\left(\frac{1}{2}+\frac{B_{\varphi i}}{B}\right) - ln\left(\frac{B_{\varphi i}}{B}\right)\right], \tag{5.2}$$

where $B_\varphi = \hbar/4el_\varphi$ and l_φ is the phase coherence length, and ψ is the digamma function.[84] Here, $\alpha_0 \in [0,1/2)$ is the WL term and $\alpha_1 \in [-1/2,0)$ is the WAL term. In this equation, 'α's are fitting parameters related to an opening of the band gap, $\alpha_0 = \Delta/2E_F$. In our samples, we can interpret the band-gap opening as a result of finite-size effects such as crystal defects and inhomogeneity, due to the lack of magnetic impurities. The best-fit constants used for samples near 0 degrees rotation at 0.3 K are shown in Table 2. WL terms are seen as having more weight for the samples quenched at higher temperatures. Weakening of WAL(WL) MR is represented in

the LSS formula through a decrease in $\alpha_1(\alpha_0)$, and/or an increase in $B_{\varphi 1}(B_{\varphi 0})$. Here an increase in B_φ is analogous to a decrease in the phase coherence length l_φ.

	α_0	$B_{\phi 0}$	α_1	$B_{\phi 1}$
1a	0.379	0.17	-0.289	0.014
1b	0.007	4.094	-0.499	2.76
2a	0.5	5.175	-0.447	0.381
2b	0	-	-0.411	1.851

Table 2. Fitting parameters for background magnetoresistance curves using Lu-Shi-Shen (LSS) formula for magnetoconductance. Parameters with subscript "0" are due to WL terms, and subscripts with "1" are due to WAL terms.

The large MR in the non-superconducting samples 2a/2b appears to be due to WAL resultant from a φ=π Berry phase and short phase coherence length.[84] While l_φ is small for all samples, l_φ must only be greater than the electron mean free path in order for WAL to occur.[84] Since we expect a lack of magnetic scattering in all samples, this indicates electrons in sample 2 have a much larger spin orbit interaction than in sample 1, where electron-phonon interactions are disregarded at low temperatures. The larger spin-orbit coupling is consistent with samples 2a and 2b having a lower Fermi energy, and less electrons in bulk bands.[84] The general differences in the decrease of MR slope is also observed in sample 1b where no superconductivity was observed. Unlike sample 2, sample 1a is not well fit to the HLN formula for magnetoconductance based solely on WAL terms alone and appear to be in a WAL-WL (weak localization) crossover, as

evidenced with the fitting parameter $\alpha_1 \neq -0.5$, which is consistent with the loss of the topologically protected surface state, and Berry phase changing from π to 0.[85]

Assuming this model is correct, we can explore the angle dependence of these measurements. Since WL/WAL is a 2D model of conduction, we would generally expect

$$R \propto B\cos(\theta)\,. \tag{5.3}$$

When the superconducting sample is rotated, we see very little angular dependence in MR unlike the large angular dependence in samples 2a and 2b. Beyond 2D, we may expect the magnitude still depends on $l_\phi(\theta)$ assuming the increased MR under rotation is due to anisotropy in the phase-coherence length. In this interpretation, the reduction in anisotropy in the superconducting sample is due to increased dislocation density, further reducing the magnitude of SdH oscillations. This large number of defects will destroy the $\cos(\theta)$ angular dependence; however, it is not clear the WL/WAL characteristics will still appear under these conditions due to their 2D nature.

5.2.2 Inhomogeneous semiconductor

Linear MR is also achieved in samples with large inhomogeneity in sample conductance. This has been demonstrated in inhomogeneous semiconductors.[86] While our samples have dislocations, the samples are high enough quality that only a single-frequency SdH oscillation appears, indicating homogeneity in Fermi energy and sample conductance. For an inhomogeneous semiconductor interpretation to be consistent with the single frequency seen in SdH oscillations, the samples would need to consist of two types of regions, with large differences in electron mobility and resistance. While this effect is sometimes cited as an explanation for linear resistance in Bi_2Se_3-type compounds, it is unlikely in our samples for a variety of reasons. This interpretation relies on a high degree of sample inhomogeneity, while SdH oscillations show a single frequency,

and thus fixed Fermi energy in our sample. The model of an inhomogeneous semiconductor agrees with the results only if we consider a dual-phase system, with one having sufficiently low electron mobility that SdH oscillations are smeared out. This second phase is presumably caused by variations in copper concentration. This is unlikely due to the relatively small differences in conductance between clean and copper-intercalated Bi_2Se_3.[87–89]

5.2.3 Quantum Linear Magnetoresistance

Linear magnetoresistance is also directly tied to quantization of energy levels in magnetic field using the theory of quantum linear magnetoresistance (QMR) first proposed by Abrikosov in 1969, but applies only when electrons are in the lowest of well-separated Landau levels.[90–92] This model requires a linear band dispersion, but not necessarily the existence of a topological state. In $Cu_xBi_2Se_3$, we have shown the Fermi surface lies in the bulk bands. Therefore, the samples with a linear resistance must have a linear dispersion formed from the bulk band-gap closing due to sample inhomogeneity at zero field, or simply a linear region of the dispersion at higher energies.[93] However, as pointed out by Abrikosov in 1998, this scenario is only possible to show oscillations if there are two well-separated regions, one with high mobility giving a single SdH oscillation frequency, and another with a very low density of charge carriers such that all electrons lie in the lowest Landau level, allowing QMR.[94] The low-density state would also have to have low mobility, which has suppressed SdH oscillations at low fields. This is quite unlikely for the same reasons as the model of an inhomogeneous semiconductor.

5.2.4 Wang-Lei Model of Magnetoresistance

The Wang-Lei model of magnetoresistance may explain the linear behavior in Bi_2Se_3 even when the conduction electrons are in bulk states.[95] In this model, Landau levels on a linear topological band occur at energies:

$$\varepsilon_n^{\pm} = \pm\sqrt{2n\varepsilon_s^2 + \delta^2} \quad (n = 1,2,\dots) \tag{5.4}$$

$$\varepsilon_0 = \delta$$

where $\varepsilon_s = v_F\sqrt{eB}$ and $\delta = -\frac{1}{2}g\mu_B B$. Here, g is the Landé g factor for conduction electrons and μ_B is the Bohr magneton. While all states for n>0 have energy pairs on opposite sides of the Dirac point, there is only one ε_0 state below (above) the Dirac point for positive (negative) g. For samples with g >0, an increasing magnetic field causes an increasingly large distance between overlapping Landau levels. This gradually lowers the density of electrons participating in conduction, and thus raises resistance. The amount of level overlap is strongly dependent on g, μ, v_F, and N, restricting the determination of these constants solely by the magnetoresistance. While the model by Wang and Lei is only considered on a topological surface, it will generally apply to any band structure, although it may not lead to linearity. The assumption of a topological Bi_2Se_3 surface merely guarantees a linear dispersion of a single electron band, which is relevant in calculating the overlap of Landau levels. If the model is applied to bulk states, the model must be altered to calculate the net carrier concentration over all bulk states, instead of a single topological state.

While the slope of magnetoresistance is most strongly dependent on g in the Wang Lei model, differences in slope between sample 1 and 2 must be influenced by other factors, since the higher Fermi energy of sample 1 will generally lead to a smaller effect from Landau splitting due

to conducting electrons primarily occupying higher Landau levels than in sample 2. For a linear band dispersion, the levels are spaced as $\varepsilon_n \propto \sqrt{nB}$, for $\delta \ll n\varepsilon_s$. This means that higher-order n levels will overlap more, in a similar way to when g is increased. However, the comparatively larger Fermi velocity in sample 1 will make sequential Landau levels spaced farther apart in energy, with less overlap, making the relation between energy and magnetoresistance complex.

The angular anisotropy in magnetoresistance is at least in part due to anisotropy in effective-g factor which has been measured by Wolos et al. in Bi_2Se_3 with $g_\perp = 19.48 \pm 0.07$ vs. $g_\parallel = 27.3 \pm 0.15$ for magnetic field perpendicular or parallel to the c-axis, respectively.[96] While the particularly large electron g-factor in Bi_2Se_3 is attributed to the strong spin-orbit coupling present, the dependency on copper intercalation and quenching is currently unknown. A full 3D model of magnetoresistance would include all anisotropic electron properties, such as g, μ, and v_F, summed over all conducting electron states, which has not been applied to bulk Bi_2Se_3 to date. In our magnetoresistive measurements we see a large anisotropy in samples 2a/b. However, the anisotropy in samples 1a/b is much smaller. These differences are likely due to the additional states which are summed over when Fermi energy is increased. In addition, the effects of quenching on g, μ, and v_F are currently unknown.

The differences in resistive measurements revealed in SdH oscillations and MR background are consistent with quenching raising the Fermi energy of the system further into bulk bands, with a smaller fraction of electrons occupying topological bands. Quenching likely creates increased dislocation density, causing incomplete bonding of bismuth and selenium at grain boundaries. Crystal vacancies at the boundaries creates an increased density of free electrons, which further raises the chemical potential. Correlations with the appearance of superconductivity

suggest the superconducting state relies on the much higher density of electrons in the bulk states and is not resultant from topological electrons.

5.3 OTHER TOPOLOGICAL SUPERCONDUCTOR CANDIDATES

5.3.1 Bismuth Selenide-Telluride

While the superconducting state in Bi_2Se_3 remains interesting, an isostructural analog Bi_2SeTe_2, provides some advantages over Bi_2Se_3. Bi_2Se_3 theoretically has a Fermi energy in the band gap, but numerous defects tend to push up the Fermi energy into bulk states. While Bi_2Te_3's Dirac point lies below the bulk band gap, the mixed Se-Te compound (Bi_2SeTe_2) has a theoretical Dirac point in the band gap and generally has less crystalline defects than Bi_2Se_3, causing a lower Fermi energy.[97] Additionally, van der Waals forces are weakened, allowing easier intercalation of atoms.[98] The challenge in growing the mixed compound intercalated with copper is phase separation into additional Bi_2Se_2Te and Bi_2Se_3 phases. We have successfully intercalated copper into this material and verified this result by studying expected effects on the lattice using procedures developed by Yanan Li, who added an annealing step which homogenizes the material.

While $Cu_xBi_2Se_3$ is not stable under the conditions needed to prepare samples for XRD and Raman spectroscopy (i.e. mechanical grinding and air exposure), the increased stability of $Cu_xBi_2SeTe_2$ allows these techniques to verify the phase purity and copper intercalation. Under the addition of copper, the *c*-axis increases monotonically in Bi_2SeTe_2 while the a-b axis remains relatively unchanged due to copper residing primarily in the van der Waals gap. Copper's occupation of the van der Waals gap adds an additional force constant for vibrations happening

out of the plane of Bi and Se(Te) layers, resulting in the softening of the A1g modes. After copper concentration of $x > 0.2$, the A1g2 mode stops softening due to copper substituting the bismuth site. Current work is aimed at probing the low-temperature phases of $Cu_xBi_2SeTe_2$, in particular the potential for superconductivity through the control of copper doping and quenching conditions.

5.3.2 Antimony Selenide

Another related system to the $Bi_2(Se/Te)_3$ system of materials is Sb_2Se_3, which has the same stoichiometry and similar elements, but different crystal structure than other Pn_2Ch_3 compounds (Pn=Bi, Sb; Ch=Se,Te) with an orthorhombic rather than hexagonal crystal structure at atmospheric pressure. While the structure of Sb_2Se_3 is very different, some similarities in electronic states exist due to the strong spin-orbit coupling present within this group of elements. Indeed, new topological insulators have been discovered in thin-film bilayers of SnTe and $Pb_xSn_{1-x}Se(Te)$ which are protected by mirror symmetry rather than time-reversal symmetry.[5] Initially starting as a strong insulator, the sample transitions under pressure to a conductor at ~3 GPa, and to a superconductor at ~10 GPa. The origin of this transition remains unclear, but our measurements of SdH oscillations in similar experiments detect a peculiar Fermi surface. Analysis performed by Uma Garg finds a Fermi surface which appears ellipsoidal in a measurement range of 45-90 degrees, however, the sudden loss of data oscillations at 45 degrees suggests either a rapidly expanding Fermi surface cross section, or a sudden decrease in electron mobility of electrons traveling in these directions. The loss in oscillation amplitude may be the result of differences in the properties of bands which are centered on symmetries corresponding to the crystallographic *a* and *b* axes.

We measure a consistent Berry phase of π in this material, consistent with the existence of a topological state in a superconducting compound and a material harboring Majorana Fermions. However, many challenges exist in this material's application for devices including the appearance of the topological state only at high pressures and relatively small single-crystal size. This material still will provide greater understanding of the role of spin-orbit coupled states and the coexistence of topological and superconducting states.

6.0 IRON-BASED SUPERCONDUCTORS

While $Cu_xBi_2Se_3$ has become a prototype for the study of topological superconductivity, many other materials have gained interest for their potential as topological superconductors. FeCh type superconductors (Ch = chalcogen) are one such class of materials which show promise of holding topological properties. FeCh-type materials have many similarities to $Cu_xBi_2Se_3$, including a quasi-cylindrical Fermi surface core, similar to that of highly charge-doped Bi_2Se_3.[99] This matching dimension of the Fermi surface means that topological triviality of the superconducting state is calculated in the same manner in these materials, namely, by counting the number of time-reversal-invariant momenta enclosed by the Fermi surface.[7] This similarity becomes particularly relevant in interfacial superconducting states formed in these materials, which manifest a topological superconductor through the superconducting proximity effect. In these instances, the superconducting state tunnels into the topological insulator to a depth proportional to the superconducting coherence length. This forms a superconducting state inside of the topological insulator as long as unoccupied states are available for tunneling of electrons to occur. In order for electrons to occupy both materials in this manner, a degree of control is needed over the Fermi surface of one or both materials. Superconducting-topological interfaces are of keen interest in FeCh systems due to the magnetic ordering present, which adds additional interest in the symmetry states present to form a topologically insulating state. As new abilities to control the anti-ferromagnetic ordering present in Fe-based superconductors are found, avenues will open to modify the topological state. These effects may be controlled through manipulation of spin orbit coupling, modified symmetry, and magnetic interactions.

6.1 TOPOLOGICAL STATES IN IRON-CHALCOGEN SYSTEMS

Realization of Fe superconductor-topological insulator interfaces is difficult due to the lattice mismatch in this material. FeCh (Ch=Chalcogen) superconductors have a tetragonal crystal structure, while Bi_2Se_3 type topological insulators are hexagonal. Nonetheless, some success has been found with interfaces of Bi_2Te_3/FeTe, including finding superconductivity in 7 nm FeTe thin films and an apparent superconducting gap in monolayer FeTe films on Bi_2Te_3.[100,101] A larger superconducting gap is found in 1 unit-cell layers than 2 unit-cell layers, indicating sample dimension holds importance. This is opposite to the typical behavior of materials losing the superconducting state when dimensionality is reduced and is indicative of novel superconducting characteristics.[78]

Beyond interfaces of inherently topological materials with superconductors, iron selenide thin films are suspected to be topological.[102,103] These speculations arise from multiple directions, including the existence of superconductivity on monolayer films and tunability of the band structure to a non-trivial form via modified spin-orbit coupling parameters. FeSe films on $SrTiO_3$ have a much higher superconducting temperature, with many reports of T_c ~65 K.[102,104] This represents an order-of-magnitude increase from bulk superconducting temperatures of ~8 K.[105] The increase in temperature is not fully understood, as the superconducting state is typically lost in thin films when the dimension is reduced.[78] In FeSe, lattice mismatch between FeSe/$SrTiO_3$ can induce a phase transition in the band structure near the M symmetry point from a gapless phase to a gapped phase and simultaneously suppress the hole-like band at the Γ point indicating lattice interactions can tune a topological insulator phase.[103] Additionally, tuning the spin-orbital coupling can drive monolayer FeSe from the trivial metal or semiconductor phase to a nontrivial topological insulating phase. Very recently, 2D topological superconductivity was reportedly

discovered in $FeSe_{0.55}Te_{0.45}$.[106] The tunability of spin-orbit coupling parameters in FeSe into a non-trivial state, combined with the quasi 2D Fermi surface suggest the superconducting state is novel in these systems, and has a potentially unconventional pairing mechanism.

A handful of groups have now confirmed that non-superconducting iron telluride thin films become superconducting upon exposure to oxygen, but have ruled out the role of interfacial strain.[107] In FeTe, Nie et al. demonstrate that superconductivity in iron telluride thin films is reversible upon oxygenation and vacuum annealing: superconductivity appears upon oxygenation, disappears upon vacuum annealing, and reappears upon re-annealing in oxygen.[108] In the FeTe system, recent work shows the appearance of superconductivity outside of thin-film systems, with a report by Rößler et al. finding traces of superconductivity on the surface of bulk single crystals exposed to air for over 6 months.[109] While superconductivity is well known to manifest in bulk systems of $FeSe_{1-x}Te_x$ ($0<x<0.85$), the enhancement of superconductivity via the introduction of oxygen and finite-size effects is particularly novel, as the reduction of dimensionality typically has a negative effect on the superconducting state in the BCS theory of superconductivity, but may be used in iron-based superconductors to generate novel electronic states.[78]

6.2 ROLE OF OXYGEN

The role of oxygen incorporation in FeCh systems is unclear, as it enhances superconductivity in FeTe and $FeSe_{1-x}Te_x$ ($0.15<x<1$), but poisons superconductivity in FeSe.[29] Investigations into the origin of superconductivity in the Fe-Te-Se via oxygen treatment have focused on role of oxygen in: (1) oxygen-induced change in oxidation state and its effect on charge doping and magnetic and electronic structure, and (2) de-intercalation of interstitial Fe and

consequent effects on sample stoichiometry, charge doping and magnetic states. Superconductivity in $FeSe_{1-x}Te_x$ is tied strongly to the anti-ferromagnetic (AFM) phase present at low temperatures in this system, and many modern "high-temperature" superconductors have antiferromagnetic (AFM) and spin density wave (SDW) phases correlated with the superconducting state which are influenced by interstitial concentrations and charge doping.[110,111] Additionally, changes to the oxidation state of iron, selenium, or tellurium, charge-dope the system, which will lead to superconductivity if the density of charge carriers is too low for pairing to occur between superconducting electrons or by changing the Fermi surface through influences on the Fermi energy. The introduction of oxidizing elements to $Fe_{1+d}Se_{1-x}Te_x$ is shown to leach iron from the interstitial areas and similar effects are expected to take place in the $Fe_{1+d}Te$ system. In the $Fe_{1+d}Se_{1-x}Te_x$ system, metallic iron in the interstitial region acts as a charge donor which uses the interstitial space as a conduction channel.[112–114] This planar mobility is apparent in the columnar shape of the Fermi surface representing sheet-like conduction channels.[99] Interstitial iron also has strong impacts on the phase stability of the system. The presence of interstitial iron is of great importance in all $Fe_{1+d}Ch$ systems, with narrow stoichiometries often needed for superconductivity.[33] In $Fe_{1+d}Te$ in particular, self-flux growth of the stoichiometric compound (d=0) is not possible, resulting in the formation of Fe_2Te_3 or $FeTe_2$ depending on cooling conditions Interstitial iron concentration also influences the low-temperature magneto-structural phase of $Fe_{1+d}Te$, leading to a monoclinic, incommensurate SDW phase for $d<0.15$ and an orthorhombic. commensurate SDW phase for $d>0.15$.[115] Magnetic and structural phases, valence state, and Fermi surface have strong influences on the superconducting state, and control over interstitial iron concentration is needed if superconductivity is to be found in this system.

6.2.1 Synthesis of Iron Superconductors

The exact details of synthesis often have dramatic consequences on electronic states. These details, which include stoichiometry, cooling rate, annealing, and oxygenation, are investigated to determine which factors control the superconducting state in Fe(Se/Te). $FeSe_{0.5}Te_{0.5}$ was first investigated, as a parent superconductor of this class of materials. While $Fe_{1+d}Se$ single crystals are difficult to grow based on the lack of precipitation from a self-flux, single crystals of $FeSe_{0.5}Te_{0.5}$ are crystallized from a self-flux. Superconducting samples are known to exist for a very small range of stoichiometries deviating from the stoichiometric compound with $0.015 < d < 0.03$.[32] Oxygen and iodine have been used to leach intercalants from similar materials, and are used to explore the effects of modified interstitial iron concentration. The effects of oxygenation are extremely varied, however, as oxygen exposure is known to poison superconductivity in FeSe samples, even when only exposed during grinding, and induce superconductivity in FeTe.[32,109] Iron leaching through fluorine treatment is first explored using the decomposition of polytetrafluoroethylene (PTFE) as a fluorine source.[116] Samples of FeSe powders were placed in a custom-made ampule (Fig. 6-1), sealed with PTFE.

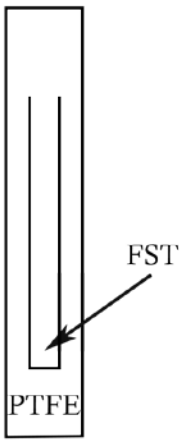

Figure 6-1. Ampule style used for fluorination of $FeSe_{0.5}Te_{0.5}$ (FST)

Fluorine treatment shows a greater T_c than as-grown $FeSe_{0.5}Te_{0.5}$, although with much smaller volume fraction as shown in Fig. 6-2. Samples annealed in the same manner without adding fluorine show similar T_c with little loss of volume fraction. Though fluorine has little influence itself on the superconducting state, annealing has positive impacts on superconductivity, likely through homogenization of interstitial iron and removal of crystal defects. While little effect was seen in fluorinated samples, oxygen is known to have a strong influence in $FeSe_{1-x}Te_x$ ($0.1<x<0.9$), and further investigations are focused on the role of oxygen treatments in $Fe_{1+d}Te$.

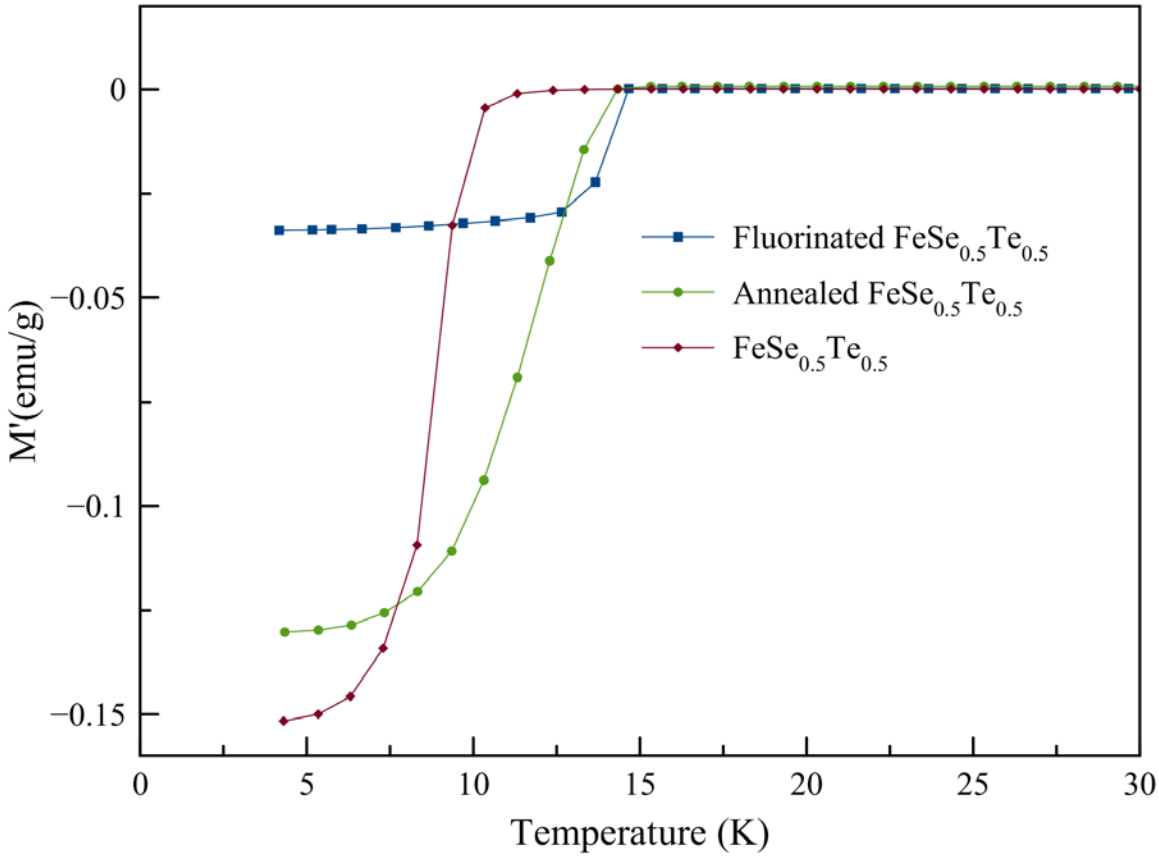

Figure 6-2. Magnetization of fluorinated and annealed $FeSe_{0.5}Te_{0.5}$ performed under 50 Oe field**.**

Oxygenation is known to have a generally positive effect on $FeSe_{0.5}Te_{0.5}$, although the root effect of oxygenation is unknown. The general sensitivity to iron concentration in FeSe motivated this research into the chemical manipulation of interstitial iron concentration in $Fe_{1+d}Se_{0.5}Te_{0.5}$ and $Fe_{1+d}Te$ to induce a superconducting state. The effects of oxidation on the magnetization of $Fe_{1+d}Te$ are complex to decipher, due to difficulties isolating changes due to interstitials from changes due to the apparent formation of $FeTe_2$. Structural investigations of $FeTe_2$ formation via oxygen annealing will be discussed later. Pure $Fe_{1+d}Te$ samples such as $Fe_{1.13}Te$ have a single PM to AFM transition around 60 K accompanied by a structural transition from tetragonal to either monoclinic or orthorhombic, depending on stoichiometry as seen in Fig. 6-3.[115] The monoclinic phase has a commensurate AFM phase, while the orthorhombic is incommensurate. In samples with stoichiometry $0.13 < d < 0.15$, magnetic phases are suppressed at grain boundaries between phases, potentially leading to a different topological state locally.[115,117] Additionally, altered crystal symmetry has a strong effect on the superconducting and topological insulator state. $Fe_{1+d}Se$ and $Fe_{1+d}Se_{1-x}Te_x$ superconductors have orthorhombic low-temperature phases, and therefore FeTe will need the same orthorhombic phase for superconductivity to exist, which is only stable for high interstitial iron concentration as seen in Fig. 6-3.[115] We chose to investigate if interstitial iron concentration can be lowered, while maintaining the orthorhombic phase, if altered by chemical means.

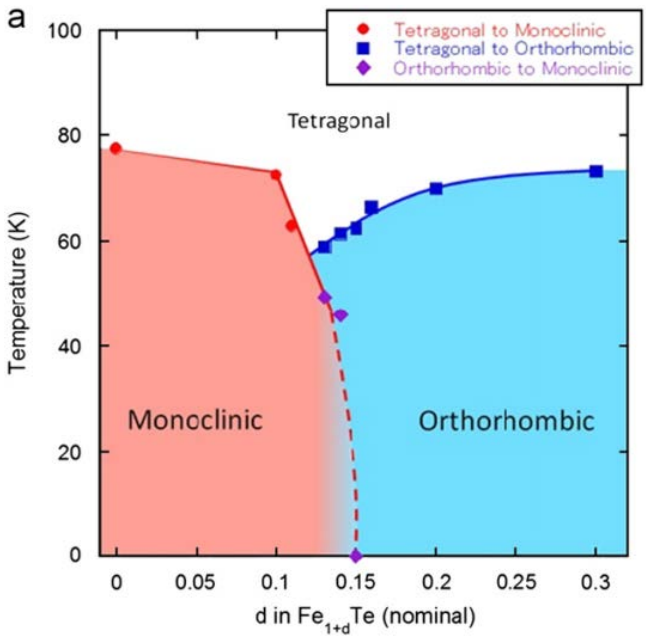

Figure 6-3. Magnetic phase diagram of $Fe_{1+d}Te$.[115]

6.2.2 Low-temperature phases of Iron Telluride

Two magneto-structural effects from competition between these phases are easily related to theories for the emergence of superconductivity in the FeSe/FeTe system. Firstly, it is possible that the competition from competing phases at low temperature induce strain, which leads to superconductivity. This narrow region conducive to superconductivity in $Fe_{1+d}Se$ may relate to the inability to form superconducting $Fe_{1+d}Te$ single crystals. Secondly, the interstitial iron concentration itself may play an important role by providing charge carriers or tuning spin-orbit coupling parameters. Indeed, the magnetic and structural effects of interstitial iron are linked in this system, as indicated by the magneto-structural transition. Beyond magneto-structural alterations from interstitial iron, the post-synthesis modification of iron via oxygen annealing may have an independent role in the formation of secondary phases.

The as-prepared sample of $Fe_{1+d}Te$ exhibits a two-stage magnetic transition at 55 K with a residual AC magnetization of ~$3x10^{-5}$ emu/g as seen in Fig. 6-4. After oxygen annealing the single crystal, the susceptibility increases to ~$4.3x10^{-5}$ emu/g. Interestingly, the same oxygen treatment of powder samples indicates an atypical rising magnetization with temperature in the PM magnetization region. This is indicative of the formation of a magnetic spin glass phase. In a spin glass, the magnetic moments are not ordered with the crystal structure, and at low temperatures the magnetic moments are "frozen" in place, leading to low magnetic susceptibility. As the temperature increases, thermal energy gradually liberates the fixed moments, increasing the

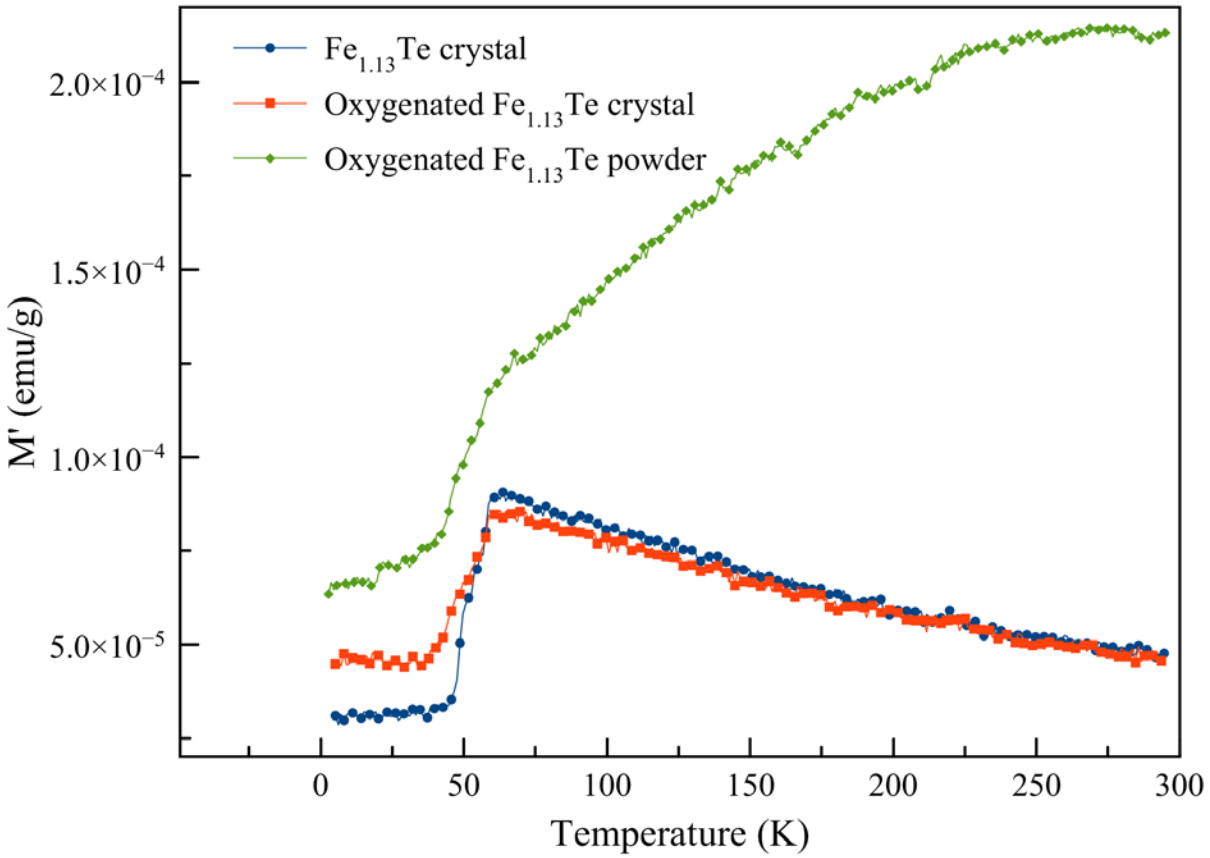

Figure 6-4. AC magnetization of $Fe_{1+d}Te$.

susceptibility, and eventually saturating. At even higher temperatures, the spin-glass ordering breaks down, and the sample transitions into a paramagnetic state.

The appearance of a spin-glass magnetic state appears to happen in only the powdered sample due to the increased penetration ability of oxygen into these samples. Under oxidation of powdered samples, the much higher surface to volume ratio leads to leaching of interstitial iron much faster, and the formation of nanoscale and smaller $FeTe_2$ compounds. This phase provides so many magnetic domain boundaries that the sample takes on a spin glass character due to the magnetic phase transition of $FeTe_2$ usually seen at 125 K. This spin-glass behavior is not ubiquitous to all $Fe_{1+d}Te$ stoichiometries as seen in Fig. 6-5. The transition seen at 125K in

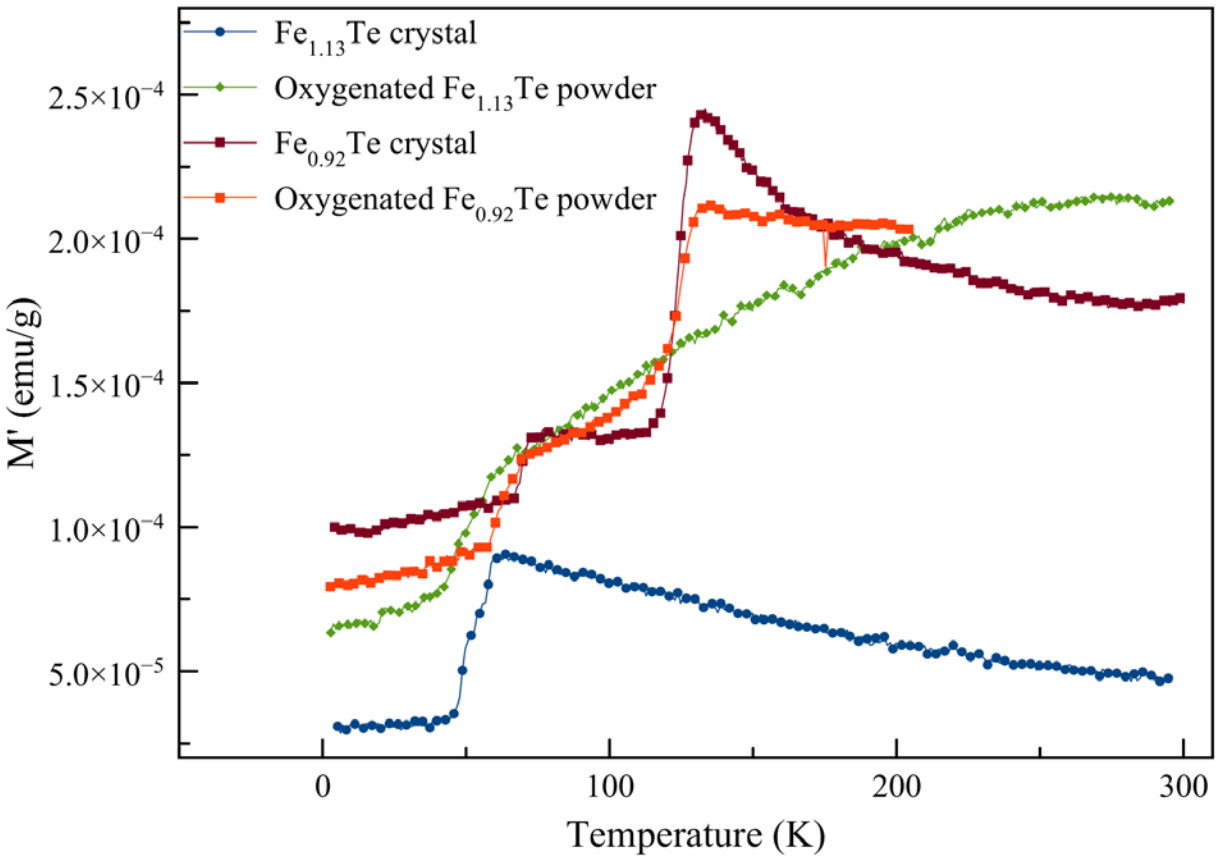

Figure 6-5. Magnetization of oxygenated Fe-Te powders and crystals.

$Fe_{0.92}Te$ is due to an $FeTe_2$ phase which was present before oxygen annealing. In samples with large volume fractions of $FeTe_2$ before annealing, a spin glass behavior does not appear upon oxygenation due to the larger magnetic domains of $FeTe_2$ already present. Following the nomenclature of Okamoto and Tanner,[30] we will refer to both samples of $Fe_{1.22}Te$ and $Fe_{1.13}Te$ as "$Fe_{1+d}Te$ (β)," or the "β-phase." In contrast, single crystals grown with a nominal composition of $Fe_{0.92}Te$ contain two phases: the β phase (tetragonal $Fe_{1+d}Te$) and the ε phase (orthorhombic $FeTe_2$), as also anticipated from the study by Okamoto and Tanner.[30] We will refer to samples of this type as "$Fe_{1-d}Te$" or "β+ε phase," to keep in mind that it contains both β and ε phases.

The magnetic transition between 60 and 125 K is smoothed in β+ε samples, and the typical 1/T paramagnetic-magnetization dependence is lost, indicating some spin-glass characteristics are still imposed in this sample. From these comparisons we can conclude the spin-glass behavior is the result of a high concentration of magnetic defects in the $Fe_{1+d}Te$ phase caused by the mobilization of Fe to sample surfaces and grain boundaries and the formation of very small $FeTe_2$ domains. The spin glass effect is partially lost when $FeTe_2$ exists in the sample before oxygenation, since less interstitial Fe is available for transport, and oxygen's ability to cause the growth of existing $FeTe_2$ crystals, rather than the forming new domains. A similar spin-glass phase is known to exist at ~20 K for $FeSe_{1-x}Te_x$ for $0.9<x<0.7$ between the superconducting and SDW magnetic phases. [118] In $FeSe_{1-x}Te_x$ the spin glass phase exists due to a large defect concentration creating a random distribution of ferromagnetic and antiferromagnetic interactions between iron ions. In FeTe, the spin-glass phase is due to numerous ferromagnetic nanometer-scale formations of $FeTe_2$, which is discussed in chapter 7.

The possibility exists that oxygen-annealed bulk crystals only superconduct on a thin surface region where oxygen interacts sufficiently with the lattice. This implies that the superconducting volumes would be too small to be detectable by conventional magnetic susceptibility measurements. For this reason, we employed the extremely sensitive magnetic field modulated microwave spectroscopy (MFMMS) technique to search for traces of superconductivity. This technique is proven to detect superconducting volumes as small as 10^{-12} cm^3 within otherwise non-superconducting material.[119] Despite this technique's sensitivity, we did not observe superconductivity. MFMMS data collected from all three oxygen-annealed single crystals is shown in Fig. 6-6. A superconducting transition would correspond to a peak-like

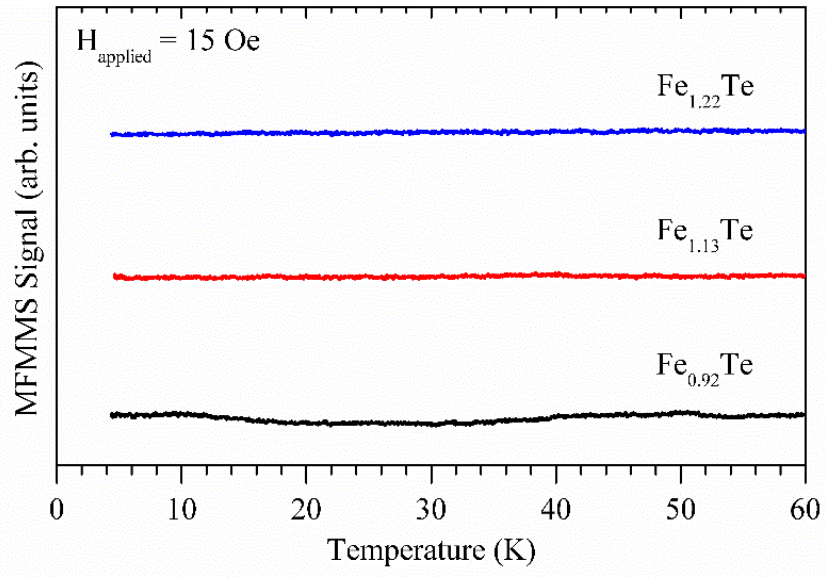

Figure 6-6. MFMMS data showing absence of superconductivity for all three oxygen annealed samples described in this work. The presence of superconductivity would have yielded a peak in the intensity at T_c.

feature in MFMMS.[120] The lack of features in data from our samples indicates a lack of a superconducting volume down to at least 10^{-12} cm^3.[119]

6.3 OXIDATION STATE OF IRON AND TELLERIUM

Samples of FeTe were also studied to investigate the role of mobilized interstitial iron on the oxidation state of lattice iron and tellurium. The relationship between oxidation state, electronic charge doping, and superconductivity is well known in systems such as the cuprates and pnictides.[82,83] However, the oxidation-state data in literature on superconducting iron telluride is contradictory. *In situ* total electron yield (TEY) and resistivity measurements show superconductivity in iron telluride films emerges upon exposure to oxygen, along with Te^0 changing to a mixed $Te^{0/4+}$ state and Fe^0 changing progressively through Fe^{2+} to Fe^{3+}. [108,121,122] Subsequent vacuum re-annealing causes the thin films to become non-superconducting, with corresponding shifts in the Fe valence from Fe^{3+} to Fe^{2+} and the Te valence from mixed $Te^{0/4+}$ back to Te^0. Telesca et al. conclude based on these results that superconductivity is accompanied by the presence of Te^{4+}, and non-superconductivity by the absence of Te^{4+}.[122] In contrast, data from Zhang et al. show no change towards Fe^{3+} in oxygen-exposed, superconducting single crystals of $Fe_{1.05}Te$, but instead an increase in the signal intensity corresponding to Fe^0.[109] The lack of Te oxidation-state data from Zhang et al. leaves the role of Te^{4+} in superconducting iron telluride unexplored in single crystals.

These valence changes are explored through X-ray absorption TEY data from $Fe_{1+d}Te$ (β) for Fe 2p (700-730 eV) and the Te 3d (568-590 eV) energy regions, in Figs. 6-7 and 6-8 respectively. Note that oxygen annealing causes a decrease in intensity of the Te $3d_{5/2}$ and $3d_{3/2}$ peaks centered at 573 and 583 eV, and an increase in the intensity of the peaks at 577 and 587 eV. This is consistent with an increase in the Te^{4+} population, along with a corresponding decrease in Te^0.[123] TEY data from Fe $2p_{3/2}$ shows a superposition of peaks at 707.5 eV and 709 eV,

corresponding to the Fe^{2+} and Fe^{3+} oxidation states, respectively.[121] The Fe^{2+} peak is higher in the parent crystal, whereas the peak corresponding to Fe^{3+} becomes higher upon annealing in oxygen.

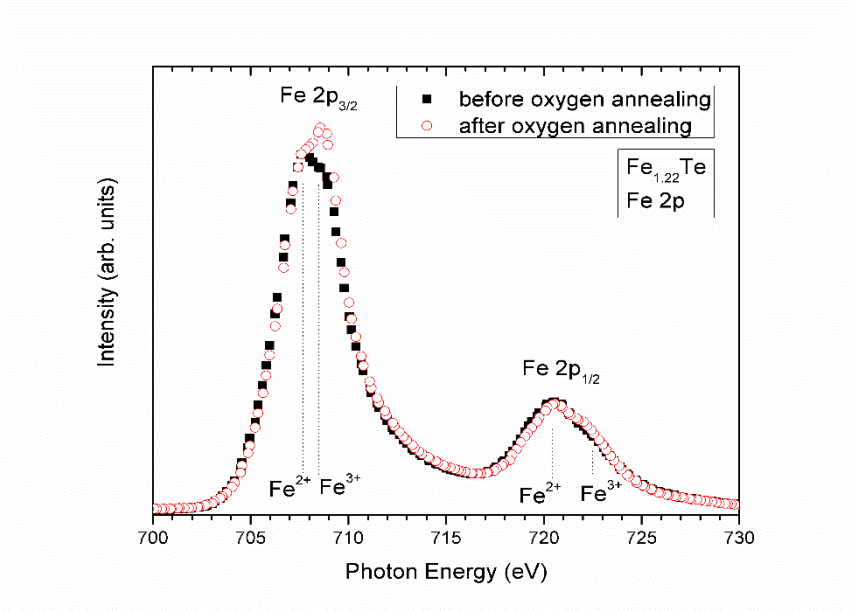

Figure 6-7. Fe $2p_{3/2}$ energy region for $Fe_{1+d}Te$ (β) before (black squares) and after (red circles) oxygen annealing. Note the increase in the intensity of the Fe^{3+} peak at ~708.5 eV (indicated by the vertical line) upon oxygen annealing.

Fig. 6-8 provides evidence that the effect of oxygen annealing on the oxidation state of Te in our single crystals is remarkably similar to that in oxygen-annealed FeTe thin films.[122] Of particular interest is the fact that the intensity of the Te^{4+} signal in our single crystals increases drastically upon oxygen exposure, just as it does with thin films studied by Telesca et al. However, this increase in Te^{4+} is not accompanied by the appearance of superconductivity in our single

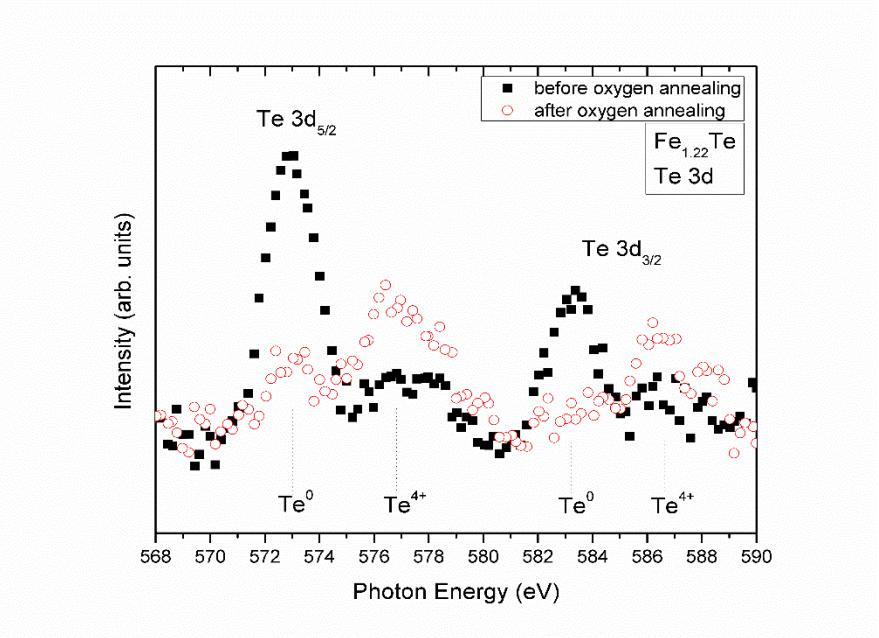

Figure 6-8. Te $3d_{5/2}$ and $3d_{3/2}$ energy regions for $Fe_{1+d}Te$ (β) before (black squares) and after (red circles) oxygen annealing. Note the increase in the peak intensities corresponding to Te^{4+} and decrease in the Te^{0} peak intensities.

crystals. Thus, our results in Figs. 6-7 and 6-8 provide the first evidence that the observation of Te^{4+} is not necessarily correlated with superconductivity in this system.

We next explore the effect of oxygen on Fe oxidation state in our single crystals in light of the conflicting published data from thin films[108,121,122] and single crystals.[109] Whereas Telesca, Nie, and colleagues show a disappearance of Fe^{0} and an increase of Fe^{3+} upon oxygenation, Zhang and colleagues report exactly the opposite: a significant increase in Fe^{0} but no increase of Fe^{3+}. Zhang et al. infer that an enhancement of the itinerant nature of Fe 3d electrons would correlate with the suppression of AFM and emergence of superconductivity in FeTe. However, this is in contradiction with published results in oxygenated superconducting thin films and the results from our oxygenated single crystals. TEY from our single crystals shows an increase in Fe^{3+} signal

intensity upon oxygen annealing, in agreement with Telesca, Nie, and colleagues but in contradiction with Zhang et al.

It is reasonable to assume that the more dramatic increase of Fe^{3+} in thin films is due to an increased penetration ability for O_2 molecules given the large surface area of the films, especially considering that some films show pin holes and grain boundaries which may significantly increase the avenues for oxygen to diffuse into the van der Waals gap of the crystal.[124] Narangammana et al. indicate that when thicker, smoother films are grown it is necessary to incorporate oxygen during growth, rather than after growth, in order to observe superconductivity.[125] However, oxygenation during growth appears to initiate substitution of tellurium in contrast with oxygen annealing interacting with interstitial elements.[107,109]

For samples around d=0.13, small changes in the amount of interstitial Fe in $Fe_{1+d}Te$ (β) determine if the low-temperature structure is orthorhombic or monoclinic.[115,126] This narrow dependency of phase stability on intercalating elements is mirrored in iron selenide ($Fe_{1+d}Se$), which is extremely sensitive to the amount of excess iron.[33] Various Fe de-intercalation techniques (including oxygen annealing) have been shown to promote superconductivity in Fe(Se,Te) compounds, but is not apparent in our samples.[112–114] The inability to transition to the superconducting state is investigated by examination of secondary effects to changes in oxidation state, namely the formation of the $FeTe_2$ minority phase.

7.0 MINORITY STRUCTURES IN OXYGENATED IRON TELLURIDE

Structural effects of oxygenation are explored through XRD and SAED which show the formation of additional oriented crystal periodicities upon oxygen exposure. Figure 7-1(a) shows a powder XRD profile of a pulverized single crystal of $Fe_{1+d}Te$ (β) before oxygen annealing, together with a Rietveld refinement profile. Powder reflections from this parent (un-annealed) single crystal agree with ICDD card number 29-0729 and have no impurity phases detectable by XRD. Rietveld refinement of XRD from the as-grown sample yields lattice parameters of a = 3.826 Å and c = 6.272 Å in a tetragonal unit cell (space group P4/nmm), consistent with previously published values.[127]

7.1 XRD

Figure 7-1(b) highlights the effects of thermal and atmospheric treatments on the XRD profile of $Fe_{1+d}Te$ (β). A small, broad feature appears in the XRD pattern around $2\theta \approx 32°$ (lattice spacing ~ 0.279 nm); this is the only change in XRD observed in $Fe_{1+d}Te$ (β) upon exposure to oxygen. This feature, with full width at half max of 0.9° in 2θ, emerges most strongly upon oxygen annealing of single crystals, but is also present after exposure of pulverized crystals to air for several days. We identify this feature as arising from the (111) reflection of $FeTe_2$ resulting from $FeTe_2$ growth in both post-annealed and air-exposed single crystals, indicating that this change arises from exposure to oxygen.

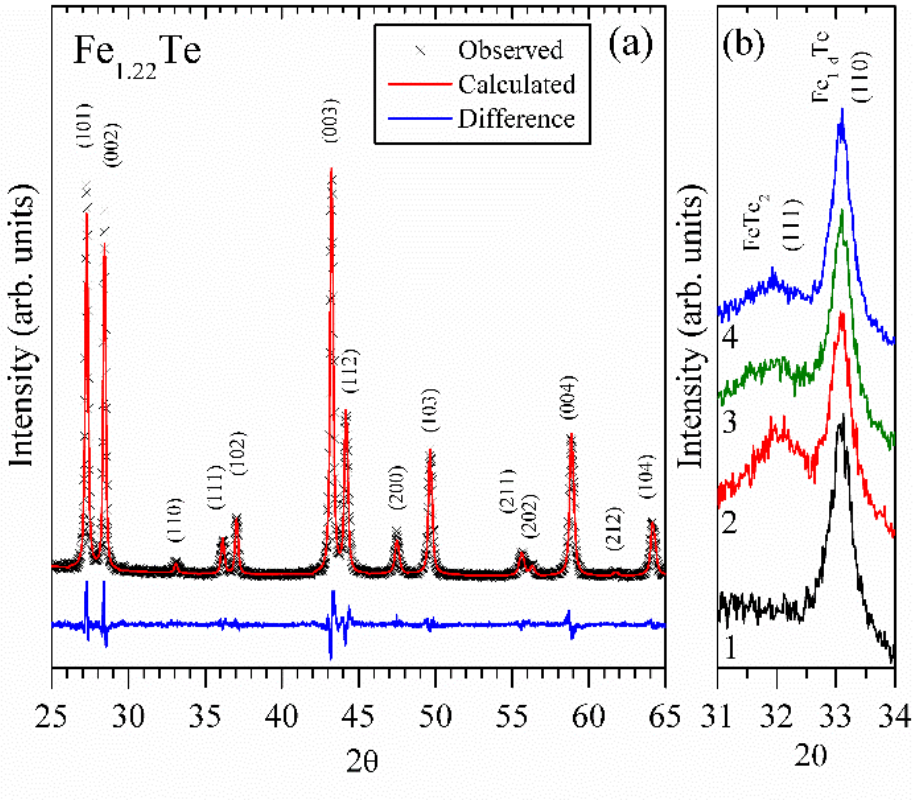

Figure 7-1. (a) Powder X-ray diffraction data of $Fe_{1.22}Te$ before oxygen annealing (black), Rietveld refinement (red line), and difference (blue line). (b) Effects of atmospheric treatments on the XRD profile of the same "parent" $Fe_{1.22}Te$ sample, [1] parent $Fe_{1.22}Te$ as shown in part (a), [2] parent sample after oxygen annealing at 125C, [3] parent sample after 7 days air exposure at room temperature, and [4] parent sample after 64 days of air exposure at room temperature.

Figure 7-1(b) of oxygen-exposed $Fe_{1+d}Te$ (β) shows a broad pre-peak of the {110} reflection emerging around a lattice spacing of 2.79 Å upon both oxygen annealing and multiple day exposure of powdered crystal to air [Fig. 7-1(b)]. This is the only change observed in the XRD profile; no accompanying peaks could be discerned with our lab-source XRD. The low intensity and broad nature of the feature makes definitive assignment using XRD data alone difficult, compounded by the fact that many iron telluride phases have reflections obscured within the strong majority phase reflections. As described below, our results from electron diffraction

help confirm that this XRD feature arises from orthorhombic $FeTe_2$ (111). The data presented in Fig. 7-1b, for a sample with d = 0.22, is typical of oxygenated $Fe_{1+d}Te$ (β) for $1.05 \leq (1+ d) \leq 1.22$.

7.2 TEM

Figure 7-2 shows two SAED patterns, (a) from as-grown $Fe_{1+d}Te$ (β) unexposed to oxygen and (b) from the same parent $Fe_{1+d}Te$ (β) crystal after annealing in oxygen. Both patterns are recorded in the same [001] zone axis orientation of the parent tetragonal phase. The square diffraction pattern in Fig. 7-2(a) is self-consistently indexed with the a-b plane Miller indices of tetragonal $Fe_{1+d}Te$ (β). The same Bragg reflections are visible in the oxygen-annealed crystal in Fig. 7-2(b), showing that the parent phase persists as the dominant phase. However, the oxygen-annealed crystal shows additional Bragg reflections in electron diffraction, with substantially lower intensity than the tetragonal pattern. These additional reflections are consistent with minority ε phase growing in an orientational relationship with the parent β phase. This is illustrated in Fig. 7-3 and discussed in the following section in further detail. Similar phase separation in $FeSe_{0.5}Te_{0.5}$ has been found by oxygen annealing and formation of an Fe_7Se_8-type phase.[128]

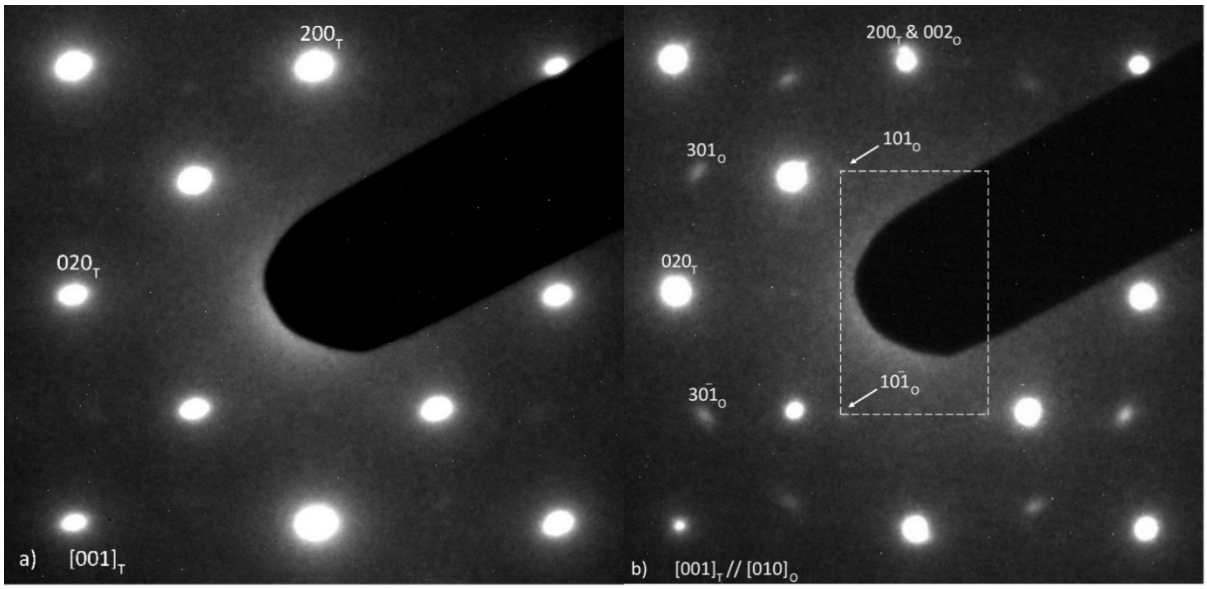

Figure 7-2. SAED patterns from as-grown $Fe_{1.13}Te$ a) and oxygen annealed $Fe_{1.13}Te$ b) crystals showing indexed reflections of the dominant tetragonal $Fe_{1+d}Te$ phase labeled with subscript "T", and secondary orthorhombic phase of $FeTe_2$ labeled with subscript "O". $Fe_{1+d}Te$ in [001] zone axis orientation yields a square pattern, as shown in a). A secondary phase is induced by annealing in oxygen, where the sublattices in b) correspond to two 90-degree oriented domains of orthorhombic $FeTe_2$. Only one of the two orientations have been labeled in this figure for the sake of clarity.

An examination of the minority phase reflections in the selected area diffraction [dashed lines in Fig. 7-2(b)] reveals two mutually-orthogonal intergrowths that can be indexed as orthorhombic diffraction patterns from $FeTe_2$ in the [010] zone axis. The $(002)_O$ planes align crystallographically with the $(200)_T$ and $(020)_T$ planes of $Fe_{1+d}Te$, as further clarified in Fig. 7-3. A cursory examination of the weak electron diffraction reflections leads one to assign these reflections to hexagonal (*P*63/*mmc*) Fe_2Te_3 phase. However, a careful analysis reveals that these reflections are more consistent with orthorhombic $FeTe_2$ phase (*Pnnm*). The new XRD reflection at $2\theta = 32°$, which arises upon oxygenation, is inconsistent with Fe_2Te_3. Further, we show in Fig.

7-4(a) results from single crystal $Fe_{0.92}Te$. Here, $Fe_{1+d}Te$ grows with an inherent $FeTe_2$ intergrowth. Oxygenation of this crystal clearly results in a growth of the $FeTe_2$ phase.

The orientation of these intergrowths corresponds to the $(002)_O$ planes of the orthorhombic phase aligning with either the $(200)_T$ or the $(020)_T$ planes of the tetragonal phase, as indexed in Fig. 7-2(b). Note that the {200} tetragonal reflections overlap with the {002} orthorhombic reflections; the {301} and {101} orthorhombic reflections from $FeTe_2$ are visible as well. Traces of the orthorhombic minority phase appear in the parent crystal, with much weaker diffraction intensities and without a measurable distortion to the a-b plane of the tetragonal parent structure. Since this sample was exposed to air during preparation and transferred into the vacuum of the microscope, the trace orthorhombic phase could be due to this exposure to air. From this, we interpret that even a short period of oxygenation initiates an intergrowth of orthogonally aligned $FeTe_2$ crystals within the bulk $Fe_{1+d}Te$ crystal, as modeled in Fig. 7-3.

7.2.1 Effects of $FeTe_2$ Intergrowth

Both the X-ray pre-peak feature in Fig. 7-1(b) and the SAED pattern shown in Fig. 7-2(b) are consistent with the results of Hu et al. in their study of oxygen-annealed $Fe_{1.08}Te_{0.55}Se_{0.45}$.[128] In that study, superconductivity in $Fe_{1.08}Te_{0.55}Se_{0.45}$ was induced via low-temperature oxygen annealing, and was accompanied by the appearance of additional reflections in electron diffraction. Hu et al. assigned these reflections to a hexagonal minority phase. Additionally, they observed a broad feature in XRD which they left unassigned. This work presents evidence that the broad feature in XRD and the additional reflections in electron diffraction can be explained by oxygen-induced growth of an orthorhombic $FeTe_2$ minority phase. We assign the unassigned feature in the XRD observed by Hu et al., as well as the feature observed by us, to the {110} set of reflections

in orthorhombic $FeTe_2$. Though the $Fe_{1+d}Te$ and $FeTe_2$ crystals have different space groups and somewhat different lattice parameters, the nearly matching Te-Te distance (as shown in Fig. 7-3) allows $FeTe_2$ to grow within the FeTe host lattice, possibly via domain boundaries. Viewing the proposed intergrowth configuration of the crystals in real space from the <100> direction of FeTe [Fig. 7-3(a)] allows us to see that both crystals share a similar stacking of tellurium atoms allowing an epitaxial crystal growth. Viewing the structures from the <010> direction of the FeTe parent [Fig. 7-2(b)] demonstrates the relative iron deficiency of the $FeTe_2$ structure and similar distance between tellurium layers. Oxygen-mediated mobility of both lattice and interstitial iron (not shown in Fig. 7-3) is likely the cause of this iron-deficient orthorhombic phase.

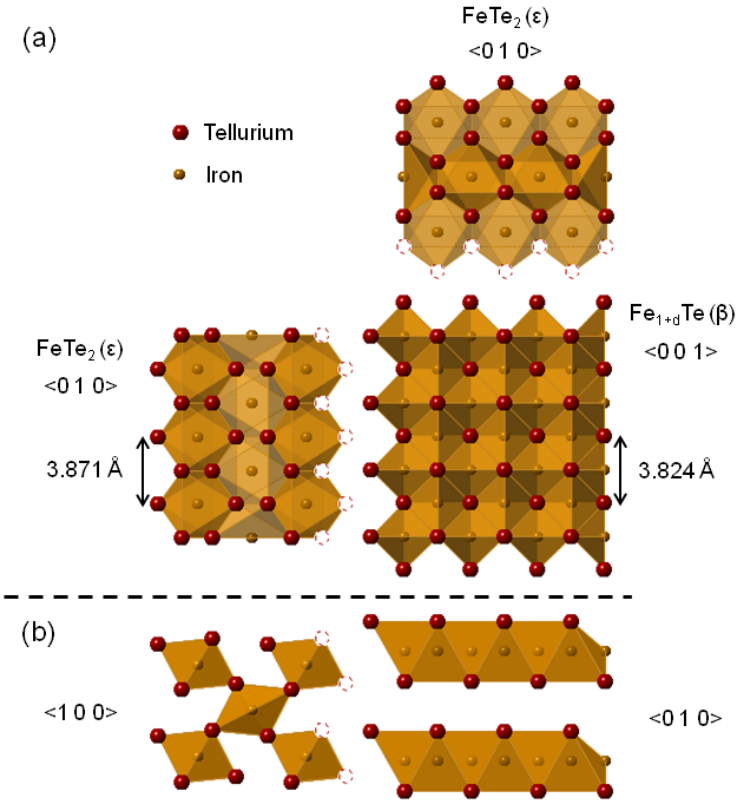

Figure 7-3. Proposed model of the intergrowth of $FeTe_2$ within $Fe_{1+d}Te$, upon oxygen annealing. (a) shows the structures as viewed in the tetragonal <001> direction, the same direction as shown in Fig. 7-2. Note the similar Te-Te distances at the interface. (b) shows the structures rotated 90 degrees into the tetragonal <100> direction.

The proposed model of the growth of $FeTe_2$ on $Fe_{1+d}Te$ upon exposure to oxygen, is shown from the β <001> direction in Fig. 6a and from the β <010> direction in Fig. 7-3(b). The interatomic distances shown here were derived from Rietveld refinement of the XRD profile in Fig. 7-1(a) (after annealing) and are consistent with reported values [ICDD cards 29-0729 and 07-0367].[129,130] Excess Fe in the $Fe_{1+d}Te$ phase is not shown (for clarity) but would reside within the interstitial spaces between stacked layers of the FeTe structure shown in Fig. 7-3(b).[131] The $FeTe_2$ phase in Fig. 7-3(a) is shown twice, one rotated 90 degrees relative to the other, in order to show that the two growth directions are crystallographically equivalent. Both directions of growth are evident in the analysis of Fig. 7-2.

It has been shown that oxygen annealing bulk $Fe_{1+d}Se_{0.6}Te_{0.4}$ causes the de-intercalation of interstitial iron and results in an iron-rich surface on the exterior a-b plane of the crystal.[114] This implies ionic conduction of both interstitial and lattice Fe since the only path to the a-b plane surface for an interstitial Fe would be through the lattice, not through the van der Waals gap. Thus as lattice iron atoms are pulled out of the structure and onto the surface of the crystal, nearby interstitial iron atoms are simultaneously pulled into the structure. However, when there are no longer any free interstitial iron atoms available to replenish vacant lattice iron, the result is a structural change to an iron-deficient phase within the majority lattice, as we see in our data.

This identifies what may be a complicating factor towards the appearance of superconductivity in bulk iron telluride. Oxygen-annealing of bulk single crystals clearly causes mobility of both interstitial and structural iron in the system, leading to local structural inhomogeneity. However, the literature, which describes oxygen annealing induced superconductivity at similarly low temperatures in thin films, does not report the growth of any

structural minority. In fact, the structure and transport properties of as-grown crystals and oxygen-annealed superconducting films are reported to be remarkably similar.[125] The absence of superconductivity and presence of a minority structural phase upon oxygen annealing bulk single crystals thus indicate the possibility that this minority-phase growth may be impeding the onset of superconductivity. The presence of a minority phase in thin-film samples is largely unknown, possibly due to the lack of sensitivity of diffraction methods in oriented thin films.

7.2.2 Oxygenation state of Intergrowths

It is important to confirm that a minority growth of $FeTe_2$ (ε) in oxygenated single phase $Fe_{1+d}Te$ (β) is not responsible for the observed changes in valence shown in Figs. 6-7 and 6-8. To explore this possibility, Fig. 7-4 examines the effect of oxygen annealing on the structure of $Fe_{1-d}Te$ (β+ε) and compares the valence states with the results obtained from $Fe_{1+d}Te$ (β). Figure 7-4(a) shows changes in XRD peak intensity corresponding to changes in relative content of the β and ε phases before and after oxygen annealing $Fe_{1-d}Te$ (β+ε). Up arrows in Fig. 7-4(a) indicate locations of non-overlapping ε peaks and down arrows indicate locations of non-overlapping β peaks, highlighting the areas to inspect for relative change. Care was taken to control for changes in XRD peak intensity due to changes in preferred orientation before and after annealing. To mimic an *in situ* anneal, we annealed the powder in the XRD sample holder without disturbing it, then returned it to the diffractometer in the same orientation for the post-anneal measurement. Rietveld refinement of the XRD before and after oxygen annealing yields a relative change in β:ε ratio (by weight) from 79:21 to 49:51.

Figures 7-4(b) and 7-4(c) compare the pre and post oxygen annealed TEY spectra of single-phase, Fe-excess $Fe_{1+d}Te$ (β) with mixed-phase, Fe-deficient $Fe_{1-d}Te$ (β+ε). The spectra of the

single-phase and the mixed-phase samples are identical with respect to changes in the oxidation states of Te and Fe before and after oxygen annealing. We interpret from this that the valence shifts observed upon oxygenation are not due to the formation of the minority ε phase.

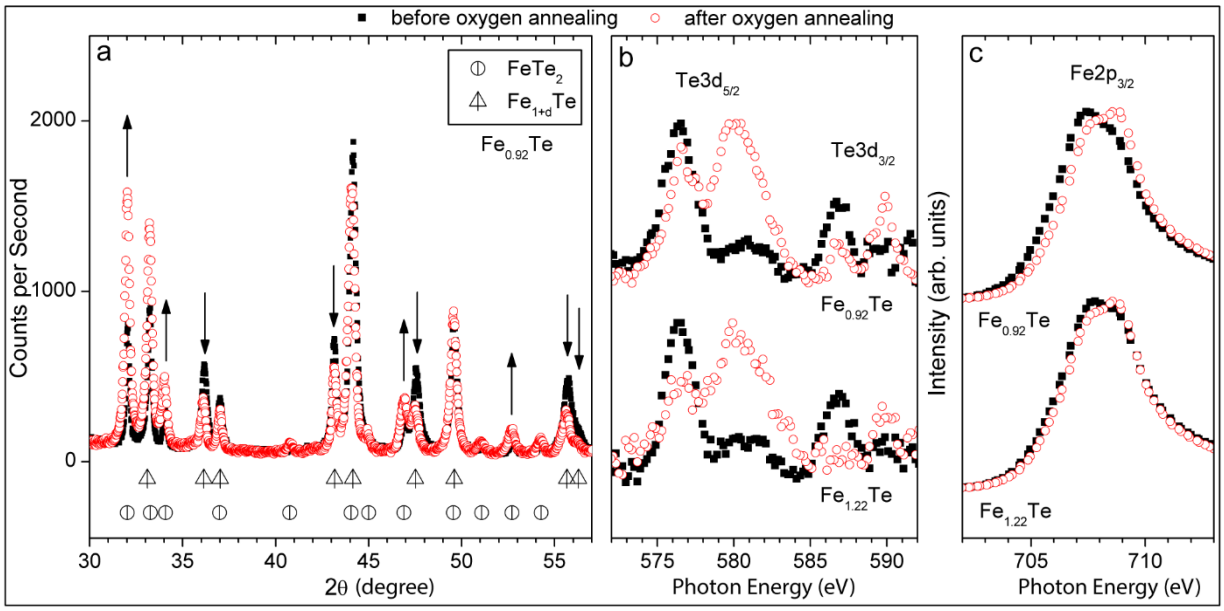

Figure 7-4. XRD of $Fe_{1+d}Te$ before (black squares) and after (red circles) oxygen annealing. (a) the XRD for $Fe_{0.92}Te$ highlighting the change in relative amounts of the β and ε phases upon oxygen annealing. Arrows indicate the growth or decrease of non-overlapping $FeTe_2$ "ε" reflections. Lines under the data indicate the positions of reflections for the constituent $Fe_{1+d}Te$ "β" and $FeTe_2$ "ε" phases. (b) and (c) compare the TEY spectra of $Fe_{0.92}Te$ to $Fe_{1.22}Te$. Note the pre- and post-annealing similarity in the x-ray absorption spectroscopy TEY data between the mixed-phase and single-phase samples.

To investigate the potential connection between the observed oxygen-induced valence change from the minority growth we studied a sample with intentional iron deficit $Fe_{1-d}Te$ ($Fe_{0.92}Te$), which had an unambiguously mixed $FeTe/FeTe_2$ phase, both before and after oxygen annealing. Figure 7-4 demonstrates that oxygen induces the growth of $FeTe_2$ at the expense of $Fe_{1+d}Te$: every non-overlapping peak assigned to $FeTe_2$ increases after oxygen annealing, and every non-overlapping peak assigned to $Fe_{1+d}Te$ decreases after oxygen annealing. As described

previously, quantitative Rietveld refinement of the XRD profile demonstrates that the proportion of orthorhombic ε phase increases dramatically upon oxygenation at the expense of the tetragonal β phase, lowering the ratio of β to ε from 79:21 to 49:51 (β:ε). In addition, TEY data presented in Figs. 7-4(b) and 7-4(c) shows remarkable similarity of both pre- and post-oxygen annealing when compared to the data presented earlier of the $Fe_{1+d}Te$ single-phase sample [Figs. 6-7 and 6-8, reprinted in Figs. 7-4(b) and 7-4(c)]. We conclude from these observations that the growth of the minority phase of $FeTe_2$ is not responsible for the changes seen in $Fe_{1+d}Te$ oxidation state. If $FeTe_2$ were responsible for changes in the oxygenation state, one would expect the pre-oxygen-annealed $Fe_{1-d}Te$ spectra to resemble the post-oxygen-annealed $Fe_{1+d}Te$ spectra. Therefore, although there is evidence of oxygen-induced minority-phase growth in pure-tetragonal-phase $Fe_{1+d}Te$, it is not likely correlated with the changes in the overall iron or tellurium valence as observed with TEY.

8.0 CONCLUSIONS

The manipulation of parameters leading to superconductivity in topological insulators is crucial to understanding the fundamental physics behind novel superconductors, as well as the construction of devices based on these materials. Many factors control the emergence of these quantum states, which are not easily decoupled. The topological state, for example, is easily broken by the modification of spin-orbit coupling parameters, the modification of which generally changes the Fermi energy through carrier concentration. The studies presented in this dissertation present a means of controlling some of these parameters and an ability to influence the crystal structures into those that harbor the coexistence of superconducting and topological states.

8.1 MANIPULATION OF THE FERMI SURFACE IN COPPER-DOPED BISMUTH SELENIDE

Quenching temperature is shown to strongly influence the Fermi surface of bismuth selenide by raising the Fermi energy. This increase of Fermi energy, in part through the introduction of defects has the correlated effect of expanding the Fermi surface. Other authors have found charge doping through off-stoichiometric elemental concentration (i.e. $Bi_{2-x}Se_3$) or copper intercalation increases the Fermi energy, eventually creating a quasi-2D Fermi surface.[42] However, these reports do not find a superconducting state, and are therefore unable to fully correlate effects of charge doping with superconductivity. This dissertation shows high-temperature quenching of $Cu_xBi_2Se_3$ induces superconductivity due to a combination of charge doping and effects on the crystal

structure. Effects of quenching on the Fermi energy are supported by a combination of results from SdH oscillations and magnetoresistance. Additionally, SAED suggests quenching influences the appearance of superstructures and CDWs resultant from copper ordering.

8.2 EFFECTS OF OXYGENATION TREATMENT ON IRON TELLURIDE

The primary effect of oxygen treatment of FeTe crystals, in a similar manner to those that induce superconductivity in $FeSe_{1-x}Te_x$ single crystals and FeTe thin films, is the formation of a $FeTe_2$ minority phase. The $FeTe_2$ phase formed is highly oriented, with the lattice of the parent FeTe crystal structure suggesting it is epitaxially bonded. Oxygen is believed to leach iron out of the system through the van der Waals gap, followed quickly by bonding to iron in the lattice. The leaching of iron from the lattice causes an iron deficiency, leading to a phase transition into $FeTe_2$. Oxidation also causes changes in the valence state of Te from Te^0 to Te^{4+} and increases the ratio of Fe^{3+} to Fe^{2+}. This change in oxidation state happens regardless of the phase purity of the compound, indicating the change in oxidation state is not caused by the appearance of $FeTe_2$. The transition of Fe valence from Fe^{2+} to Fe^{3+} is less complete than what is found in oxygenated thin films, indicating an important difference in oxygen dynamics between bulk crystals and thin films.

8.3 LIMITATIONS

8.3.1 Bi_2Se_3-type topological insulators

In bismuth selenide, unreliable superconducting phase fractions make definitive identification of factors leading to superconductivity difficult. Methods that reliably produce superconductivity tend to lead to small volumes of superconductivity, even at 0.3 K. These small volumes of superconducting phase at low temperatures point to sample inhomogeneity, which limits the ability to distinguish properties from superconducting and non-superconducting regions. Additionally, efficient structural characterization via XRD is limited due to the material's sensitivity to oxidation and mechanical stress. Isolation of surface electron properties is also difficult due to the formation of selenium vacancies raising the Fermi energy into bulk bands, even without addition of charge doping intercalants.

8.3.2 FeTe-type superconductors

The translation of novel superconducting states in iron telluride thin films to bulk systems is limited by intrinsic differences between films and bulk samples. Thin films are necessarily grown on a substrate, which provides a stabilization of lattice parameters through coupling to the substrate. Additionally, low dimensionality of thin films will have influences on magnetic ordering and 2D interfacial electronic states. The anomalously high-temperature superconductivity found in monolayer FeSe is unlikely to appear in other 11-type bulk systems. Oxygen treatment on epitaxial thin films is inherently different from bulk crystals; the former only exposes the (001) surface of thin films to oxidation, whereas single crystals expose all faces. The

dynamics of oxidation on the (100) surface will have differing effects on interstitial iron due to an ability to access interstitial areas directly, without first interacting with interstitial iron.

8.4 FUTURE WORK

8.4.1 Bi_2Se_3-type topological insulators

The technique used to modify the Fermi energy and induce superconductivity in copper doped Bi_2Se_3 is directly translatable to isostructural crystal systems including Bi_2Te_3 and Sb_2Te_3 binary systems. The isostructural Bi_2SeTe_2 structure, which has a reduced Se site defect density and lower Fermi energy, will likely have analogous effects. The control of the Fermi energy via quenching allows a greater control of conducting electron states by tuning the Fermi energy with respect to the Dirac point and bulk electron states, independently from copper intercalation. The discovery of superconductivity in compounds isostructural to Bi_2Se_3 will bring an increased understanding of the superconducting state in this system. Bi_2Se_3-type materials host many other intercalants including other transition metals, and easily form heterostructures with lead-based compounds of the PbSe type. Reliable control of Fermi energy in these systems will give increased understanding as superconducting and topological properties are found in these materials with varied band structures and Fermi energies.

The tunability of quenching to manipulate the Fermi surface is not well understood, in particular, if quenching provides continuous manipulation of the Fermi energy by means such as random defects, or creating a high-temperature phase, e.g. superstructures and CDWs. Comparison of the effects of quenching in isostructural compounds will provide increased

knowledge about the effects of quenching, particularly with compounds which are more homogenous and stable to mechanical stress. The decoupling of effects from mechanical stress, Fermi energy, and intercalation ordering, is particularly important to understanding the origin of the superconducting state.

8.4.2 FeTe-type superconductors

Differences in the effects of oxygen treatments in thin films are at least in part due to the mobility of iron and oxygen diffusion in the material. Oxygen reacting with substrate-stabilized films will uptake oxygen more slowly than single crystals due to oxygen needing to diffuse through the lattice, rather than reacting with interstitial iron directly. The formation of $FeTe_2$ caused by iron deficiency can be mediated by allowing oxygen to diffuse uniformly into the system. The diffusion of oxygen into bulk systems can be further explored by controlling the oxygen pressure, density, and temperature. Other methods of controlling iron deintercalation and phase stability are of interest in the FeCh system and should be explored as a combination of the effects on interstitial iron concentration and the superconducting state. The factors likely to impact the superconducting state with deintercalation are control of oxygen environment, particle size, exposure time, and choice of chemical oxidizer. The small range of iron stoichiometry leading to superconductivity in $Fe_{1+d}Se$ is likely mirrored in the $Fe_{1+d}Te$ and other systems leading to a narrow range of treatment parameters resulting in a superconducting state.

REFRENCES

1. Kitaev, A. Y. Fault-tolerant quantum computation by anyons. *Ann. Phys. (N. Y).* **303,** 2–30 (2003).

2. Ivanov, D. A. Non-Abelian statistics of half-quantum vortices in p-wave superconductors. *Phys. Rev. Lett.* **86,** 268–271 (2001).

3. Read, N. & Green, D. Paired states of fermions in two dimensions with breaking of parity and time-reversal symmetries and the fractional quantum Hall effect. *Phys. Rev. B - Condens. Matter Mater. Phys.* **61,** 10267–10297 (2000).

4. Lin, Y.-M., Rabin, O., Cronin, S. B., Ying, J. Y. & Dresselhaus, M. S. Semimetal–semiconductor transition in Bi1−xSbx alloy nanowires and their thermoelectric properties. *Appl. Phys. Lett.* **81,** 2403–2405 (2002).

5. Tian, W., Yu, W., Shi, J. & Wang, Y. The property, preparation and application of topological insulators: A review. *Materials (Basel).* **10,** (2017).

6. Hasan, M. Z. & Kane, C. L. Topological Insulators. *Physics (College. Park. Md).* **82,** 23 (2010).

7. Sato, M. & Ando, Y. Topological superconductors: A review. *Reports Prog. Phys.* **80,** (2017).

8. Björnson, K. Spin-orbit interactions in topological insulators. (2010).

9. Tong, D. Lectures on the Quantum Hall Effect. *TIFR Infosys Lectures* (2016).

10. Ren, Y., Qiao, Z. & Niu, Q. Topological phases in two-dimensional materials: A review. *Reports Prog. Phys.* **79,** (2016).

11. Hasan, M. Z. & Kane, C. L. Colloquium: Topological insulators. *Rev. Mod. Phys.* **82,** 3045–3067 (2010).

12. Lu, H. Z. & Shen, S. Q. Weak localization of bulk channels in topological insulator thin films. *Phys. Rev. B - Condens. Matter Mater. Phys.* **84,** (2011).

13. Feng, W., Liu, C. C., Liu, G. Bin, Zhou, J. J. & Yao, Y. First-principles investigations on the Berry phase effect in spin-orbit coupling materials. *Comput. Mater. Sci.* **112,** 428–447 (2016).

14. Hirsch, J. E. The origin of the Meissner effect in new and old superconductors. *Phys. Scr.* **85,** (2012).

15. Wilczek, F. Majorana returns. *Nat. Phys.* **5,** 614–618 (2009).

16. Brun, C., Cren, T. & Roditchev, D. Review of 2D superconductivity: the ultimate case of epitaxial monolayers. *Supercond. Sci. Technol.* **30,** 013003 (2017).

17. Uchihashi, T. Two-dimensional superconductors with atomic-scale thickness. *Supercond. Sci. Technol.* **30,** 013002 (2017).

18. Majorana, E. Teoria simmetrica dell'elettrone e del positrone. *Nuovo Cim.* **14,** 171–184 (1937).

19. Fu, L., Kane, C. L. & Mele, E. J. Topological Insulators in Three Dimensions. *Phys. Rev. Lett.* **98,** 1–4 (2007).

20. Nayak, C., Simon, S. H., Stern, A., Freedman, M. & Das Sarma, S. Non-Abelian anyons and topological quantum computation. *Reviews of Modern Physics* **80,** 1083–1159 (2008).

21. Gerischer, H., Decker, F. & Scrosati, B. The electronic and ionic contribution to the free energy of Alkali Metals inIntercalation Compounds. *J. Electrochem. Soc.* **141,** 2297–2300 (1994).

22. Bruce, P. G., Armstrong, A. R. & Gitzendanner, R. L. New intercalation compounds for lithium batteries: layered LiMnO2. *J. Mater. Chem.* **9,** 193–198 (1999).

23. Van der Ven, A., Bhattacharya, J. & Belak, A. A. Understanding Li Diffusion in Li-Intercalation Compounds. *Acc. Chem. Res.* **46,** 1216–1225 (2013).

24. Sharma, N. *et al.* The Unique Structural Evolution of the O3-Phase $Na_{2/3}$ $Fe_{2/3}$ $Mn_{1/3}$ O_2 during High Rate Charge/Discharge: A Sodium-Centred Perspective. *Adv. Funct. Mater.* n/a-n/a (2015). doi:10.1002/adfm.201501655

25. Chen, K. P., Chung, F. R., Wang, M. & Koski, K. J. Dual element intercalation into 2D layered Bi2Se3 nanoribbons. *J. Am. Chem. Soc.* **137,** 5431–5437 (2015).

26. Krzton-Maziopa, A., Svitlyk, V., Pomjakushina, E., Puzniak, R. & Conder, K. Superconductivity in alkali metal intercalated iron selenides. *J. Phys. Condens. Matter* **28,** (2016).

27. Legendre, B. & Querniard, F. Glossary for binary phase diagram reactions. *J. Phase Equilibria Diffus.* **35,** 11–14 (2014).

28. Awana, V. P. S. *et al.* Superconductivity of Fe based pnictides and chalcogenides: Material aspects, doping routes, future prospects and challenges. **8,** 8–11 (2012).

29. Aswathy, P. M., Anooja, J. B., Sarun, P. M. & Syamaprasad, U. An overview on iron based superconductors. *Supercond. Sci. Technol.* **23,** 073001 (2010).

30. Okamoto, H. & Tanner, L. E. The Fe-Te (Iron-Tellurium) System. *J. Phase Equilibria* **11,**

371–376 (1990).

31. Wang, Q. Y. *et al.* Interface-induced high-temperature superconductivity in single unit-cell FeSe films on SrTiO3. *Chinese Phys. Lett.* **29,** (2012).

32. Pomjakushina, E., Conder, K., Pomjakushin, V., Bendele, M. & Khasanov, R. Synthesis, crystal structure, and chemical stability of the superconductor FeSe1−x. *dw* **80,** 024517 (2009).

33. McQueen, T. M. *et al.* Extreme sensitivity of superconductivity to stoichiometry in Fe_{1+δ}Se. *Phys. Rev. B* **79,** 014522 (2009).

34. Schneeloch, J. a., Zhong, R. D., Xu, Z. J., Gu, G. D. & Tranquada, J. M. Dependence of superconductivity in CuxBi2Se3 on quenching conditions. *Phys. Rev. B* **91,** 144506 (2015).

35. Hansen, M. Bi-Se phase diagram. in *Phase diagrams of Binary alloys* (ed. Anderko, K.) 334–335 (The Maple Press Company, 1958).

36. Hansen, M. Sb-Te phase diagram. in *Phase diagrams of Binary alloys* (ed. Anderko, K.) 1177–1179 (The Maple Press Company, 1958).

37. Kong, D. *et al.* Rapid surface oxidation as a source of surface degradation factor for Bi2Se3. *ACS Nano* **5,** 4698–4703 (2011).

38. Zhang, H. *et al.* Topological insulators in Bi2Se3, Bi2Te3 and Sb2Te3 with a single Dirac cone on the surface. *Nat. Phys.* **5,** 438–442 (2009).

39. Fujita, S. & Ito, K. Chapter 12: Magnetoresistance. in *Quantum Theory of Conducting Matter* 151–169 (Springer, 2007).

40. Lifshits, I. & Kosevich, A. On the Theory of Magnetic Susceptibility of Metals At Low Temperatures. *Sov. Phys. JETP* **2,** 636–645 (1956).

41. Analytis, J. G. *et al.* Bulk Fermi surface coexistence with Dirac surface state in Bi2 Se3: A comparison of photoemission and Shubnikov-de Haas measurements. *Phys. Rev. B - Condens. Matter Mater. Phys.* **81,** 1–5 (2010).

42. Lahoud, E. *et al.* Evolution of the Fermi surface of a doped topological insulator with carrier concentration. *Phys. Rev. B - Condens. Matter Mater. Phys.* **88,** 1–9 (2013).

43. Sears, V. F. Neutron scattering lengths and cross sections. *Neutron News* **3,** 26–37 (1992).

44. Henke, B. L., Gullikson, E. M. & Davis, J. C. X-Ray Interactions: Photoabsorption, Scattering, Transmission, and Reflection at E = 50-30,000 eV, Z = 1-92. *At. Data Nucl. Data Tables* **54,** 181–342 (1993).

45. Electron–Specimen Interactions. in *Transmission Electron Microscopy* 139–192 (Springer New York). doi:10.1007/978-0-387-40093-8_5

46. West, D., Sun, Y. Y., Wang, H., Bang, J. & Zhang, S. B. Native defects in second-generation topological insulators: Effect of spin-orbit interaction on Bi 2Se 3. *Phys. Rev. B - Condens. Matter Mater. Phys.* **86,** 1–4 (2012).

47. Zhang, H. *et al.* Bi1-xSbx Alloy Nanocrystals: Colloidal Synthesis, Charge Transport, and Thermoelectric Properties. *ACS Nano* **7,** 10296–10306 (2013).

48. Kondo, R., Yoshinaka, T., Imai, Y. & Maeda, A. Reproducible Synthetic Method for the Topological Superconductor Cu x Bi 2 Se 3. *J. Phys. Soc. Japan* **82,** 063702 (2013).

49. Talantsev, E. F., Crump, W. P. & Tallon, J. L. Universal scaling of the self-field critical current in superconductors: From sub-nanometre to millimetre size. *Sci. Rep.* **7,** 1–15 (2017).

50. Lawson, B. J. *et al.* Quantum oscillations in CuxBi2Se3 in high magnetic fields. *Phys. Rev. B* **90,** 195141 (2014).

51. Vedeneev, S. I., Knyazev, D. A., Prudkoglyad, V. A., Romanova, T. A. & Sadakov, A. V. Quantum oscillations in strong magnetic fields, berry phase, and superconductivity in three-dimensional topological Bi2–x Cu x Se3 insulators. *J. Exp. Theor. Phys.* **121,** 65–75 (2015).

52. Yoshida, M. *et al.* Controlling charge-density-wave states in nano-thick crystals of 1T-TaS2. *Sci. Rep.* **4,** 1–5 (2014).

53. Fujisawa, Y., Shimabukuro, T., Kojima, H., Demura, S. & Sakata, H. Effect of Fe-doping on CDW state in 1 T -TaS 2 investigated by STM / STS. in *Journal of Physics; Conference Series* 1–4 (2017).

54. Bray-Ali, N. & Haas, S. How to turn a topological insulator into a superconductor. *Physics (College. Park. Md).* **3,** 11 (2010).

55. Hansen, M. Bi-Cu phase diagram.pdf. in *Phase Diagrams of Binary alloys* (ed. Anderko, K.) 308–309 (The Maple Press Company, 1958).

56. Hansen, M. Cu-Se phase diagram.pdf. in *Phase diagrams of Binary alloys* (ed. Anderko, K.) 628–629 (The Maple Press Company, 1958).

57. Zhu, X. G. *et al.* Doping nature of Cu in epitaxial topological insulator Bi2Te3thin films. *Surf. Sci.* **617,** 156–161 (2013).

58. Wray, L. A. Spectroscopic studies of unconventional superconductivity in iron pnictides and doped topological insulators. *PhD Thesis* (2010).

59. Hu, W. Z., Zhang, Q. M. & Wang, N. L. Optical and Raman spectroscopy studies on Fe-based superconductors. *Phys. C Supercond.* **469,** 545–558 (2009).

60. Johannes, M. D. & Mazin, I. I. Fermi surface nesting and the origin of charge density waves in metals. *Phys. Rev. B - Condens. Matter Mater. Phys.* **77,** 1–8 (2008).

61. Koski, K. J. *et al.* Chemical intercalation of zerovalent metals into 2D layered Bi2Se3 nanoribbons. supp. *J. Am. Chem. Soc.* **134,** 13773–9 (2012).

62. Yonezawa, S. *et al.* Thermodynamic evidence for nematic superconductivity in Cu x Bi 2 Se 3. *Nat. Phys.* **13,** 123–126 (2017).

63. Matano, K., Kriener, M., Segawa, K., Ando, Y. & Zheng, G. Q. Spin-rotation symmetry breaking in the superconducting state of CuxBi2Se3. *Nat. Phys.* **12,** 852–854 (2016).

64. Zhu, Z. H. *et al.* Layer-by-layer entangled spin-orbital texture of the topological surface state in Bi2Se3. *Phys. Rev. Lett.* **110,** 1–5 (2013).

65. Hajlaoui, M. *et al.* Ultrafast surface carrier dynamics in the topological insulator Bi2Te3. *Nano Lett.* **12,** 3532–3536 (2012).

66. Lindau, I. & Spicer, W. E. The probing depth in photoemission and auger-electron spectroscopy. *J. Electron Spectros. Relat. Phenomena* **3,** 409–413 (1974).

67. Tanaka, Y. *et al.* Evolution of electronic structure upon Cu doping in the topological insulator Bi_{2}Se_{3}. *Phys. Rev. B* **85,** 125111 (2012).

68. Chou, S. Y., Antoniadis, D. A. & H.I., S. Application of Shubnikov-de Haas oscillations in the Characterization of Si MOSFET's and GaAs MODFET's. 883–888 (1987).

69. Li, Y., Wu, K., Shi, J. & Xie, X. Electron transport properties of three-dimensional topological insulators. *Front. Phys.* **7,** 165–174 (2012).

70. Taskin, A. A., Sasaki, S., Segawa, K. & Ando, Y. Manifestation of topological protection in transport properties of epitaxial Bi2Se3 thin films. *Phys. Rev. Lett.* **109,** 1–5 (2012).

71. Fang, L. *et al.* Catalyst-free growth of millimeter-long topological insulator Bi 2Se3 nanoribbons and the observation of the pi-berry phase. *Nano Lett.* **12,** 6164–6169 (2012).

72. Taskin, A. A., Sasaki, S., Segawa, K. & Ando, Y. Manifestation of Topological Protection in Transport Properties of Epitaxial Bi 2 Se 3 Thin Films. **066803,** 1–5 (2012).

73. Lawson, B. J., Hor, Y. S. & Li, L. Quantum oscillations in the topological superconductor candidate Cu 0.25Bi2Se3. *Phys. Rev. Lett.* **109,** 1–5 (2012).

74. Patton, B. R. Fluctuation theory of the superconducting transition in restricted dimensionality. *Phys. Rev. Lett.* **27,** 1273–1276 (1971).

75. Eagles, D. M. Possible pairing without superconductivity at low carrier concentrations in bulk and thin-film superconducting semiconductors. *Phys. Rev.* **186,** 456–463 (1969).

76. Xi, X. X., Geerk, J., Linker, G., Li, Q. & Meyer, O. Preparation and superconducting properties of ultrathin YBa2Cu3O7−x films. *Appl. Phys. Lett.* **54,** 2367 (1989).

77. Herzer, G. Grain Size Dependence of Coercivity and Permeability in Nanocrystalline

Ferromagnets. *IEEE Trans. Magn.* **26,** 1397–1402 (1990).

78. Hanak, J. J., Gittleman, J. I., Pellicane, J. P. & Bozowski, S. The effect of grain size on the superconducting transition temperature of the transition metals. *Phys. Lett. A* **30,** 201–202 (1969).

79. Vasko, A., Tichy, L., Horak, J. & Weissenstein, J. Applied Physics Amphoteric Nature of Copper Impurities in B i 2 Se3 Crystals. *Appl. Phys.* **5,** 217–221 (1974).

80. Koski, K. J. *et al.* High-Density Chemical Intercalation of Zero-Valent Copper into Bi2Se3 Nanoribbons. 12–15 (2012).

81. Wang, M. *et al.* A combined method for synthesis of superconducting Cu Sample Preparation. *Nat. Sci. Reports* 1–13 (2016). doi:10.1038/srep22713

82. Miyakawa, N., Guptasarma, P., Zasadzinski, J., Hinks, D. & Gray, K. Strong Dependence of the Superconducting Gap on Oxygen Doping from Tunneling Measurements on Bi2Sr2CaCu2O8-δ. *Phys. Rev. Lett.* **80,** 157–160 (1998).

83. Basov, D. N. & Chubukov, a. V. Manifesto for a higher Tc -- lessons from pnictides and cuprates. *Nat. Publ. Gr.* **7,** 272–276 (2011).

84. Lu, H. Z., Shi, J. & Shen, S. Q. Competition between weak localization and antilocalization in topological surface states. *Phys. Rev. Lett.* **107,** 8–10 (2011).

85. Lang, M. *et al.* Competing weak localization and weak antilocalization in ultrathin topological insulators. *Nano Lett.* **13,** 48–53 (2013).

86. Parish, M. M. & Littlewood, P. B. Non-saturating magnetoresistance in heavily disordered semiconductors. *Nature* **426,** 162–165 (2003).

87. Hor, Y. S. *et al.* Superconductivity in Cu_{x}Bi_{2}Se_{3} and its Implications for Pairing in the Undoped Topological Insulator. *Phys. Rev. Lett.* **104,** 057001 (2010).

88. Butch, N. P. *et al.* Strong surface scattering in ultrahigh-mobility Bi2 Se 3 topological insulator crystals. *Phys. Rev. B - Condens. Matter Mater. Phys.* **81,** 1–5 (2010).

89. Caywood, L. P. & Miller, G. R. Anistropy of the constant-energy surfaces in n-Type Bi2Te3 and Bi2Se3 from galvanomagnetic coefficients. *Phys. Rev. B* **2,** 3209–3220 (1970).

90. Abrikosov, A. A. Quantum linear magnetoresistance. *Europhys. Lett.* **49,** 789–793 (2000).

91. Abrikosov, A. A. Quantum magnetoresistance of layered semimetals. *Phys. Rev. B* **60,** 4231–4234 (1999).

92. Abrikosov, A. A. Galvanomagnetic Phenomena in Metals in the Quantum Limit. *Sov. Phys. JETP* **29,** 746–753 (1969).

93. Hu, J. & Rosenbaum, T. F. Classical and quantum routes to linear magnetoresistance. *Nat*

Mater **7,** 697–700 (2008).

94. Abrikosov, A. A. Quantum magnetoresistance. *Phys. Rev. B* **58,** 2788–2794 (1998).

95. Wang, C. M. & Lei, X. L. Linear magnetoresistance on the topological surface. *Phys. Rev. B - Condens. Matter Mater. Phys.* **86,** 1–7 (2012).

96. Wolos, A. *et al.* G -factors of conduction electrons and holes in B i2 S e3 three-dimensional topological insulator. *Phys. Rev. B* **93,** 1–8 (2016).

97. Shi, H., Parker, D., Du, M. H. & Singh, D. J. Connecting thermoelectric performance and topological-insulator behavior: Bi2Te3 and Bi2Te2Se from first principles. *Phys. Rev. Appl.* **3,** 1–10 (2015).

98. Park, K., Nomura, Y., Arita, R., Llobet, A. & Louca, D. Local strain and anharmonicity in the bonding of Bi2Se3-xTex topological insulators. *Phys. Rev. B* **88,** 224108 (2013).

99. Subedi, A., Zhang, L., Singh, D. J. & Du, M. H. Density functional study of FeS, FeSe, and FeTe: Electronic structure, magnetism, phonons, and superconductivity. *Phys. Rev. B - Condens. Matter Mater. Phys.* **78,** 1–6 (2008).

100. Manna, S. *et al.* Interfacial superconductivity in a bi-collinear antiferromagnetically ordered FeTe monolayer on a topological insulator. *Nat. Commun.* **8,** 1–8 (2017).

101. He, Q. L. *et al.* Two-dimensional superconductivity at the interface of a Bi2 Te3 /FeTe heterostructure. *Nat. Commun.* **5,** 1–8 (2014).

102. Hao, N. & Shen, S. Q. Topological superconducting states in monolayer FeSe/ SrTiO3. *Phys. Rev. B - Condens. Matter Mater. Phys.* **92,** 1–10 (2015).

103. Hao, N. & Hu, J. Topological phases in the single-layer FeSe. *Phys. Rev. X* **4,** 1–17 (2014).

104. Zhang, Z. *et al.* Onset of the Meissner effect at 65 K in FeSe thin film grown on Nb-doped SrTiO 3 substrate. *Sci. Bull.* **60,** 1301–1304 (2015).

105. Hsu, F.-C. *et al.* Superconductivity in the PbO-type structure alpha-FeSe. *Proc. Natl. Acad. Sci. U. S. A.* **105,** 14262–4 (2008).

106. Zhang, P. *et al.* Observation of topological superconductivity on the surface of an iron-based superconductor. *Science (80-.).* **360,** 182–186 (2018).

107. Zheng, M. *et al.* Uniform Oxyge Doping Leads to Superconductivity in FeTe Films. *arXiv:1301.4696* **1,** 1–4 (2013).

108. Nie, Y. F., Telesca, D., Budnick, J. I., Sinkovic, B. & Wells, B. O. Superconductivity induced in iron telluride films by low-temperature oxygen incorporation. *Phys. Rev. B* **82,** 020508 (2010).

109. Zhang, Z. T. *et al.* Superconductivity in Fe1.05Te:Ox single crystals. *Phys. Rev. B* **88,**

214511 (2013).

110. Fang, C., Xu, B., Dai, P., Xiang, T. & Hu, J. Magnetic frustration and iron-vacancy ordering in iron chalcogenide. *Phys. Rev. B* **85,** 134406 (2012).

111. Wang, Z. *et al.* Microstructure and structural phase transitions in iron-based superconductors. *Chinese Phys. B* **22,** 087409 (2013).

112. Hu, J., Wang, G. C., Qian, B. & Mao, Z. Q. Inhomogeneous superconductivity induced by interstitial Fe deintercalation in oxidizing-agent-annealed and HNO 3 -treated Fe 1+ y (Te 1− x Se x). *Supercond. Sci. Technol.* **25,** 084011 (2012).

113. Rodriguez, E. E. *et al.* Chemical control of interstitial iron leading to superconductivity in Fe1+xTe0.7Se0.3. *Chem. Sci.* **2,** 1782 (2011).

114. Sun, Y. *et al.* Dynamics and mechanism of oxygen annealing in Fe1+yTe0.6Se0.4 single crystal. *Sci. Rep.* **4,** 4585 (2014).

115. Mizuguchi, Y. *et al.* Evolution of two-step structural phase transition in Fe1+dTe detected by low-temperature x-ray diffraction. *Solid State Commun.* **152,** 1047–1051 (2012).

116. Patocka, J. & Bajgar, J. Toxicology of Perfluoroisobutene. *Appl. Sci. Anal. ASA Inc.* (1998).

117. Zhao, P. H. *et al.* O2 Annealing Induced Superconductivity in FeTe1−x Se x : on the Origin of Superconductivity in FeTe Films. *J. Supercond. Nov. Magn.* **30,** 871–876 (2017).

118. Yesigat, A. Study of coexistance of superconductivity and Spin Glass in Iron Pnictide (Fe1+ySexTe1-x). (Addis Ababa University, 2011).

119. de la Venta, J. *et al.* Corrigendum: Methodology and search for superconductivity in the La–Si–C system. *Supercond. Sci. Technol.* **25,** 049501 (2012).

120. Kim, B. F., Bohandy, J., Moorjani, K. & Adrian, F. J. A novel microwave technique for detection of superconductivity. *J. Appl. Phys.* **63,** 2029–2032 (1988).

121. Telesca, D., Nie, Y., Budnick, J. I., Wells, B. O. & Sinkovic, B. Impact of valence states on the superconductivity of iron telluride and iron selenide films with incorporated oxygen. *Phys. Rev. B* **85,** 214517 (2012).

122. Telesca, D., Nie, Y., Budnick, J. I., Wells, B. O. & Sinkovic, B. Surface valence states and stoichiometry of non-superconducting and superconducting FeTe films. *Surf. Sci.* **606,** 1056–1061 (2012).

123. Balitskii, O. A. & Jaegermann, W. XPS study of InTe and GaTe single crystals oxidation. *Mater. Chem. Phys.* **97,** 98–101 (2006).

124. Telesca, D. A. Local Electronic Structure of Magnetic and Superconducting Thin Films. (University Of Connecticut, 2010).

125. Narangammana, L. K. *et al.* Low temperature crystal structure and large lattice discontinuity at T c in superconducting FeTeOx films. *Appl. Phys. Lett.* **103,** 0–4 (2013).

126. Rößler, S. *et al.* First-order structural transition in the magnetically ordered phase of Fe_{1.13}Te. *Phys. Rev. B* **84,** 174506 (2011).

127. Mizuguchi, Y., Hamada, K. & Miura, O. Structural and magnetic properties of Fe1+dTe single crystals. *Phys. Procedia* **27,** 6 (2012).

128. Hu, H. *et al.* Structure of the oxygen-annealed chalcogenide superconductor Fe_{1.08}Te_{0.55}Se_{0.45}O_{x}. *Phys. Rev. B* **85,** 064504 (2012).

129. Fruchart, D. *et al.* Structure antiferroma gnetique de Fe1. 125Te accompagnee d'une deformation monoclinique. *Mater. Res. Bull.* **10,** 169–174 (1975).

130. Grønvold, F., Haraldsen, H. & Vihovde, J. Phase and Structural Relations in the System Iron Tellurium. *Acta Chem. Scand.* **8,** 1927–1942 (1954).

131. Zheng, M. Superconductivity in Oxygen Doped Iron Telluride By Molecular Beam Epitaxy. (University of Illinois at Urbana-Champaign, 2013).

CIRRICULUM VITAE

Nathaniel Smith

Education:

B.S., University of Wisconsin-Madison, May 2011
Major: Physics
Certificate: Mathematics

Dissertation Title: Crystal Growth and Manipulation of Intercalated Chalcogenides as Superconductors and Topological Insulators

Research Expertise:

- Research and analysis
- Experimental design
- Computer programming
- Laboratory organization
- Equipment troubleshooting and maintenance
- TEM microscopy
- XRD, Synchrotron, electron and neutron diffraction
- Structural and Magnetic analysis

Programming languages: MatLab, Python, LabView, Maple, Mathematica

Appointments:

- Teaching Assistant, Department of Physics, University of Wisconsin: Milwaukee, 2011-2018
- Teaching Laboratory Manager, Department of Physics, University of Wisconsin: Milwaukee, 2017-2018
- Science Graduate Student Research Fellow (SCGSR), Oak Ridge National Lab & Argonne National Lab, 2016
- Undergraduate Research Assistant, University of Wisconsin: Madison, 2008-2011
- Research Experience for Undergraduates (REU) Fellowship: Johns Hopkins University, 2010

Research Experience:

2012 – 2018 ***Graduate Research Assistant***
University of Wisconsin: Milwaukee, Milwaukee, WI
• Design and implementation of experiments investigating quantum properties of single crystals at cryogenic temperatures

• Programming and data modeling of a variety of experimental systems
• Installation and troubleshooting of instrumentation including high temperature furnaces, cryogenic systems, and data collection instrumentation.
• Group training on laboratory safety, equipment use, analysis techniques, and laboratory policy.

SCGSR Fellow

1/2016 – 9/2016 Oak Ridge National Lab, Oak Ridge, TN

• Initiated new experimental directions in protype sodium ion battery cathodes.
• Calibration of equipment for use in neutron diffraction expiments
• Design, manufacture, characterization, and failure testing of sodium ion battery cells.

National High Magnetic Field Labratory User

5/2016 – 3/2017 National High Magnetic Field Laboratory, Tallahassee, FL

• Low temperature-high field magneto-resistive studies of single crystals of superconducting topological insulators
• High pressure THz frequency magnto-resistive studies on topological insulators

Teaching:

Over five years as a Teaching Assistant, with experience designing lab practicals, designing new laboratory experiments, grading, and overseeing labs

Teaching Assistant

2011-2018 Department of Physics, University of Wisconsin: Milwaukee

• TA for Astronomy 104; Physics 110, 121, 123, 209, 210, 214, 215
• Physics tutor for introductory physics courses
• Grader for Physics 720, 721
• 3.74/4 TA rating- rating given from students, to TA's while teaching

Awards:

• **CGSA Physics Scholarship**, University of Wisconsin: Milwaukee, 2011, 2012, 2013, 2014, 2015, 2017
• **UWM Scholarship**, University of Wisconsin: Milwaukee, 2011, 2012, 2013, 2014, 2015
• **David Lichtman Memorial Scholarship**, University of Wisconsin: Milwaukee, 2013, 2014, 2015, 2016

• **Physics Foundation Award**, University of Wisconsin: Milwaukee, 2016
• **Physics Research Excellence Award**, University of Wisconsin: Milwaukee, 2017

Service and Leadership:

• Referee, *Advances in Condensed Matter Physics*, 2017
• Officer, Physics Club, Department of Physics, The University of Wisconsin: Madison, 2010-2011
• Officer, GRADS club, Graduate student advocacy and outreach organization, University of Wisconsin: Milwaukee 2014-2015

Outreach:

• Science Olympiad Volunteer
• Majors Fair-Physics Department, University of Wisconsin Milwaukee
• Undergraduate major recruiting events-Physics Department, University of Wisconsin Madison

Publications:

X-ray and neutron reflectivity and electronic properties of PCBM-poly(bromo)styrene blends and bilayers with poly(3-hexylthiophene): ***J. Mater. Chem.*, 2012, 22 (10), 4364 – 4370**

Effects of Oxygen Annealing on Single Crystal Iron Telluride (In review- Journal of Physica C)

Manuscripts:

Effect of quenching on the Fermi surface of copper intercalated Bi_2Se_3 through Shubnikov de Haas oscillations

In-Situ Neutron Diffraction Synthesis of a Ternary Sodium Ion Cathodes